Earth-Abundant Thin-Film Devices for Photovoltaic and Electrochemical Applications

James Allan Clark

A dissertation

submitted in partial fulfillment of the

requirements for the degree of

Doctor of Philosophy

University of Washington

2019

Reading Committee:

Hugh Hillhouse, Chair

Dan Schwartz

Stu Adler

Scott Dunhman, GSR

Program Authorized to Offer Degree:

Chemical Engineering

University of Washington

Abstract

Earth-Abundant Thin-Film Devices for Photovoltaic and Electrochemical Applications

James Allan Clark

Chair of the Supervisory Committee:
Hugh Hillhouse
Chemical Engineering

Humanity faces a host of unprecedented challenges in the 21st century which will require inexpensive, scalable technological solutions. This thesis focuses on the technological development of devices which address two of these 21st-century challenges: global climate change and increasing pharmaceutical contamination of water supplies. Solution-processed Cu2ZnSnSe4 (CZTS) photovoltaic (PV) devices are a promising technology for next-generation PV devices because of their earth-abundant constituents and ability to be scaled up with roll-to-roll processing. This work identifies critical processing parameters during CZTS solution deposition to prevent the formation of amorphous carbon nitride impurity phases which ruin device performance. Discovery

of new complexation chemistries in CZTS solutions allowed for the stabilization of a wide range of metal chloride species via Lewis acid-base interactions. This facilitated a novel silver and germanium co-alloying strategy in CZTS which led to devices with record high performance metrics. Electrochemical oxidation is a promising technology to remediate pharmaceuticals in wastewaters, but current technologies lead to the inadvertent generation of ClO3-, ClO4-, and other toxic byproducts (TBPs) which are more hazardous than many pharmaceuticals. This work is the first to identify that the high nitrogen content in human urine (which contain the majority of excreted pharmaceuticals) suppress ClO3- and ClO4- formation by 3 orders of magnitude. A novel, inexpensive device scheme was developed to treat pharmaceutical-contaminated urine at the source of generation. This device consists of a series of divided electrochemical cells which control pH via H2 and O2 evolution, and sequence oxidation/reduction such that pharmaceuticals are oxidized while ClO3-, ClO4-, and other TBPs are reduced.

TABLE OF CONTENTS

LIST OF FIGURES

LIST OF TABLES

ACKNOWLEDGEMENTS

First, I want to thank my family for the ways in which they contributed to the man I am today. I want to thank my mom for being remaining my best friend for all my life. Your constant support and advice is one of my greatest treasures, and I could not have made it here without you. I want to thank my dad for bribing me to get straight A's throughout high school. I am so grateful for your constant positivity, passion for having fun, and love of food. I want to thank my grandmother for reading to me and practicing math with me as a child. She sparked a love of learning that is still with me today. To everyone else in my huge family, I am incredibly grateful for you. I feel so fortunate to have been born in a family that gives love so freely and abundantly.

I could not have made it through this process of a PhD without the love and support of my Seattle family. Ashley, you have been such a wonderful partner in this journey though grad. school. Thank you for bringing me coffee in MolES countless times, for talking with me when I'm feeling stressed, for doing yoga with me to unwind, and for always picking up my pants. Sheeraz, thank you for being such a constant force of positivity and stability in my life. The weekly 4+ hours of board games, late night video game sessions, and countless long conversations brought me so much joy. To all my other friends in Seattle: Joe Demaria, Willy Voje, Brian Grewe, Matt Crane, Barry Badeau, Matt Murbach, Andrew Collord, Rachael Noce, Ray Zhang, Heather Dahlin, Josh Mcdougal, Ed Michor, and so many more, I am so grateful my journey here in Seattle led me to meet you. Thank you for being such wonderful friends.

Throughout my time as a PhD candidate I have been very fortunate to have excellent mentors and advisors. Prof. Hillhouse, thank you for your leadership throughout this process. You taught me to face scientific problems with a deep understanding of the fundamentals, while staying rooted in what is practical. You constantly pushed me to be better and contributed so much to my growth as a scientist. To my committee members over the years, Prof. Schwartz, Prof. Dunham, Prof. Fu, Prof. Yu, and Prof. Adler, thank for your feedback and guidance. To all my labmates over the years, Andrew Collord, John Katahara, Hao Xin, Alex Uhl, Felix Eickemeyer, Sarah Vorpahl, Trevor Martin, Ian Braly, Warren Pinkard, Wes Williamson, Ryan Stoddard, Kyle Harrigan,

Yuhang Yang, Anna Murray, Julie Lee, Kathy Chen, and Nathanael Ramos, thank you for the thoughtful conversations about research, your help in the lab, and for the many lunches together.

DEDICATION

To my family, my partners, and my friends, thank you for the love.

Prologue

This section outlines the structure of this document and highlights the publications which result from this work. In **Chapter 1**, I give a high level overview of the motivation for the research presented in this work. In **Chapter 2**, I give a brief overview of photovoltaics and a background for solution processes chalcogenide materials. In **Chapter 3**, I present results published in *Chemistry of Materials*[1] regarding impurity transport in solution processed chalcogenide films. I also present previously unpublished data related to Li-doping and sulfurization effects on impurity transport in these systems. In **Chapter 4**, I present work published in *The Journal of the American Chemistry Society*[2] related to complexation chemistry in DMF chalcogenide molecular inks. This enabled the fabrication of record PCE $CuInSe_2$ devices in separate work.[3] I also present previously unpublished data related to Ag and Ge co-alloying in CZTS along with a novel CdTe molecular ink. In **Chapter 5**, I give a brief overview of fundamentals in electrochemistry and a background electrochemical treatment of wastewaters. In **Chapter 6**, I present results for a manuscript that is planned to be submitted to *Environmental Science and Technology*[4], which presents a novel electrochemical scheme to oxidize pharmaceuticals in human urine while minimizing toxic byproduct formation. Finally, in **Chapter 7**, I share concluding comments and outline future research for both solution-processed chalcogenide semiconductors and an inexpensive device to remediate pharmaceuticals in urine.

Chapter 1- Earth-Abundance and the Economics of Scale

1.1 Technological Solutions to 21st Century Problems

In the 21st century, humanity will have to overcome challenges the likes of which it has never encountered before. Many of these challenges are the product of technological innovations of the 20th century. Greenhouse gases emitted from the burning of fossil fuels are warming the planet, which is leading to massive changes and redistribution of biodiversity in ecosystems across the globe.[5] The widespread use of antibiotics is contaminating water supplies and leading to an increasing prevalence in antibiotic-resistant microorganisms.[6] Addressing these challenges, along with the many others that we face, will require a combination of technological, ideological, and political solutions. This work addresses some of humanity's 21st century challenges through a combination of fundamental and applied research.

Fundamental research aims to discover and understand the phenomena of the universe, while applied research aims to solve specific problems. The research presented in this dissertation has led to fundamental discoveries, but was always rooted in an attempt to address specific problems through the development of technological devices . For example, this work led to the discovery novel copper chloride complexes in dimethylformamide, but this effort was rooted inmaking an efficient, cheap solar cells. Central to the goal of making devices to solve humanity's problems is the reality that these devices must be engineered to be practical and inexpensive. This is required if they are to be manufactured at a the scale required to address massive problems such as greenhouse gas emissions or antibiotic-resistant microorganisms. In considering device designs, the strategies that we used to address this scalability constraint were: (1) avoid the use of extremely toxic chemicals, (2) use fabrication techniques that can be easily

scaled-up, (3) design devices with long service lifetimes, and (4) choose materials with earth-abundant elements.

1.2 Solution-Processed Chalcogenide Photovoltaics and the Evolving Economics of Silicon Photovoltaics

One of the biggest challenges facing humanity in 2019 is the rapid deployment of clean energy solutions to mitigate the effects of climate change. Despite the reality of climate change, a combination of ideological and political factors continue to support substantial doubt about anthropogenic climate change and its potential negative impacts on humans and animal populations.[7,8] Therefore, in order for clean energy to be widely adopted by the free-market regardless of beliefs, it is imperative to develop clean energy technologies that are cheaper than fossil fuel technologies. Due to the abundance of the solar resource, photovoltaics (PV) have massive potential as a clean-energy technological solution to address the growing energy needs of the 21st century. About 600−1000 TW strikes the earth's terrestrial surfaces at practical sites suitable for solar energy harvesting.[9] Despite this fact, as of 2016, the world's total installed PV capacity was 320 GW_p,[10] which represents only ~1% of the world's total electricity generation.[11]

A comparison of PV absorber layers in **Table 1.1** shows that crystalline silicon (c-Si) and polycrystalline silicon (pc-Si) dominated the PV market and made up ~95% of the added capacity in 2016. The other 5% is represented by CdTe, $Cu(In,Ga)Se_2$ (CIGS), and a-Si, all of which are thin-film solar cells. Silicon absorber layers require 100 times the thickness compared to thin-film absorbers. This is due to the much higher absorption coefficient for these thin-film technologies (a result of their direct band gap versus silicon's indirect band gap). CdTe modules can compete in price with Si modules, but the low elemental abundance of Te in the earth's crust

has disincentivized additional investment in this technology. CIGS modules made from current physical vapor deposition technologies are somewhat competitive with Si-modules, but continued reduction in Si module price has limited market share. Devices based on the III-V absorbers, GaAs, and InP have achieved very high power conversion efficiencies (PCEs) of 28.8% and 24.2%;[12] however, they have virtually no market share in utility scale PV, because the increased efficiencies do not sufficiently offset the high cost of manufacturing (performed via epitaxial growth). Amorphous silicon (a-Si) cells have achieved much lower PCE's than the crystalline counterparts, yet, because of the relatively low manufacturing cost, accounted for 500 MW_p of added capacity in 2016. While high PCE's are important, the examples of GaAs and a-Si also illustrate the importance of low manufacturing costs for a PV technology to compete with silicon.

Absorber Layer	Crystalline Silicon	Polycryst. Silicon	CdTe	$Cu(In,Ga)Se_2$	Amorphous Silicon	$Cu_2ZnSn(S,Se)_4$
2016 Added Capacity[10] [GW_p] (% of total)	[57.5] (69.6%)	[20.2] (24.4%)	[3.1] (3.7%)	[1.3] (1.6%)	[0.5] (0.6%)	-
Band gap [eV]	1.12	1.12	1.5	1.14*	1.70	1.13*
Theoretical Maximum PCE	33.5%	33.5%	32.8%	33.5%	29.0%	33.6%
Record PCE[12]	26.7%	22.3%	22.1%	22.6%	10.2%	12.6%
Solution-Processed Absorber Record PCE	-	-	12.3%[13]	17.3%[15]	-	12.6%[14]

Table 1.1 A comparison of PV absorber technologies. Theoretical maximum power conversion efficiency (PCE) is based on a detailed balance calculation based on the band gap of the absorber layer (see Section 2.1). Band gap can range from 1-1.5 eV for both CIGS and CZTS depending on the Ga/(In+Ga) and the S/(S+Se) respectively. These band gaps represent the record cells in each category. References for the added capacity,[10] Record PCE,[12] CdTe,[13] $CuInSe_2$,[15] and CZTS.[14]

To increase the adoption of PV, costs must be decreased for one or more of the above technologies. One important cost to decrease is the levelized cost of electricity (LCOE)

generated from the PV devices. LCOE takes into account the total price to install a PV system, how much power it generates (i.e., its PCE), and how long it will last. Unsurprisingly, the biggest single contributor to the total price to install a PV system is the cost of the module itself; however, soft costs (e.g., inverters, labor to install, etc.) also contributed to over 60% of the total installed price for PV installation in 2016.[11] A second, less-addressed cost that is important to decrease is the capital expenditure required to build a PV manufacturing facility. A bottom-up cost model by Powell et al. identified the high capital expenditure (CapEX) of PV manufacturing to be one of the largest barriers to the proliferation of PV technologies.[16] Incremental reductions to the capex of Si-based PV manufacturing are possible, but only to a small degree. Therefore, the development of PV technologies with exceptionally low CapEX and cost is necessary. Overall, to accelerate the growth of PV, there is a need for technological breakthroughs which lead to a PV technology that has both low LCOE and low required CapEX investment.

Solution-processed, thin-film chalcogenide photovoltaics are a promising technology to achieve the low cost goals for a next-generation PV technology. The CapEX investment required for a manufacturing facility producing 1 GW_p/year for Si modules with current technologies, thin-film modules via physical vapor deposition (PVD), and solution-processed PV devices has been estimated to be $1,000,000,000, $800,000,000, and $60,000,000, respectively.[16] The >1 order-of-magnitude lower capex for solution processing gives it the potential to be the disruptive technology that can compete with Si-manufacturing. Solution-processed PV manufacturing has not been widely adopted because the low capex is offset by lower PCEs for solution-processed films (which increases LCOE). Therefore, the key challenge for solution-processed PV is to understand and control the physical and chemical processes which lead to high PCE PV devices.

Chapter 2, **Chapter 3**, and **Chapter 4** of this work cover an introduction to and research on solution-processing for $CuInSe_2$ (CIS), $Cu(In,Ga)Se_2$ (CIGS), and $Cu_2ZnSn(S,Se)_4$ (CZTS) absorber layers for PV devices. These materials have yielded some of the highest PCEs from any solution-processed devices from any material as shown in **Table 1**. CIGS and CZTS are quite stable under ambient conditions and do not contain any toxic elements. CIGS PV devices have been developed for the past 40+ years (first device reported in 1975)[17] and have shown high PCEs from absorbers deposited by physical vapor deposition processes, as shown in **Table 1.** However, there are concerns about the potential price volatility of indium due to its moderate abundance in the earth's crust. CZTS is an extremely attractive technology because of the earth abundance of its elements and because it is readily solution-processable. CZTS devices were first reported in 1997,[18] and saw a steady rise in device improvement until 2014.[14] Unfortunately, record device PCEs have stagnated and not improved, predominantly due to the challenges with low open circuit voltage.

Over the past 5 and ½ years, improvements in solution-processed chalcogenide photovoltaics have been outpaced by massive changes in Si PV manufacturing and hybrid perovskites. The maps in **Figure 1.1a** represent price comparisons in relation to grid parity (defined as the point where the cost of PV-generated electricity equals the cost of electricity purchased from the grid) on a state by-state basis.[19] This analysis takes into account electricity price, solar irradiance in each state, and a number of other factors (e.g., 30 year lifespan, 1% degradation/year, inverter replacements every 10 years, etc.). At a total installed price of 3$/W, utility-scale PV is only economical in Hawaii, while at 1$/W, 43 states have surpassed grid

parity. Over the past seven years, the price of PV has plummeted to the point where it is now cheaper than other forms of electricity in almost every state.[5]

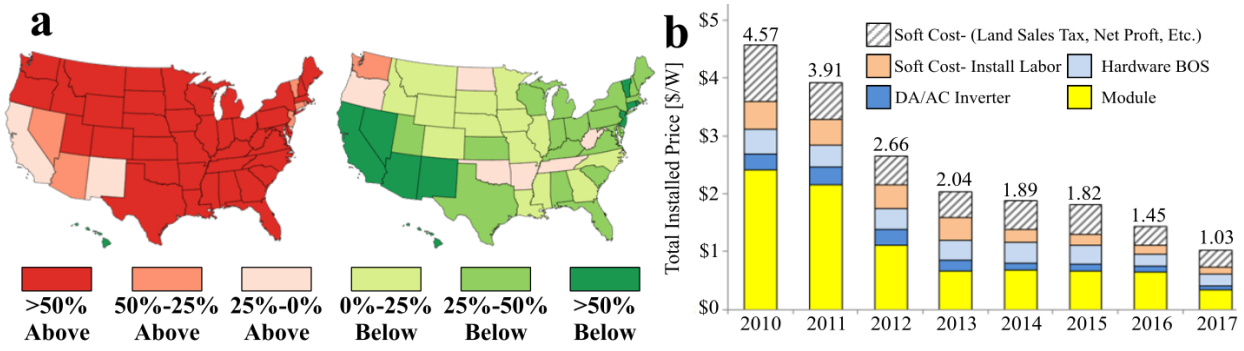

Figure 1.1 (a) Heat maps comparing the price of electricity from utility scale photovoltaics to current energy technologies in each state for a total installed price of 3$/Watt (left) and 1$/Watt (right).[19] This does not include any federal incentive and accounts for differences in electricity price and solar irradiance in each state. (b) A bar chart showing how total installed module price for utility scale PV has drastically changed over the past eight years.[5]

The drastic reduction in total installed price of PV has lead to growth at a rate of ~30%/year from 2010-2016.[10] **Figure 1.1b** highlights that every contributing cost has been reduced to achieve these record low installation prices, and that the biggest factor in the price reduction can be attributed to falling module prices. The first silicon-based solar cell was developed by Bell Laboratories in 1954,[20] and since then, an enormous amount of R&D has gone into manufacturing polysilicon, ingots, and wafers for PV and a variety of other semiconducting applications. The momentum of this technological development has contributed to the plummeting prices for Si PV technologies in the past 5 years and has raised the bar that emerging PV must meet to compete with Si PV. Over this same timespan, solution-processed hybrid perovskite PV devices have had a meteoric rise in PCE with current values >22%.[12] The combination of these effects have drastically decreased the available funding for solution-processed chalcogenide research. There remains some possibility of a breakthrough in

solution-processed chalcogenide photovoltaics, as I will outline the the **Conclusions and Future Work**. However, the reality of the evolving funding situation for chalcogenide photovoltaics prompted a transition of the majority of my research efforts into a different direction for the final year of my PhD.

1.3 The Proliferation of Pharmaceuticals in the Water Supply and the Potential of Advanced Oxidation Processes

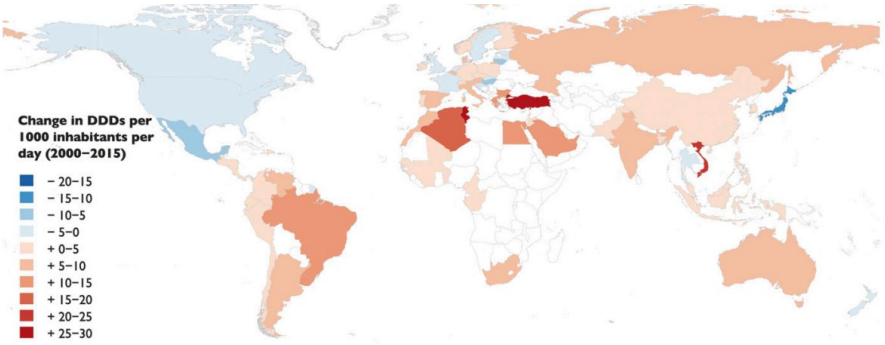

Figure 1.2: Changes in defined daily doses of human consumed pharmaceuticals from 2000 to 2015 representing an average global increase of 65%. [21]

From 2011 to 2016, the global pharmaceutical industry grew from 956 $bn to 1105 $bn, and is expected to continue to swell to 1450 $bn by 2021. The FDA has approved over 1100 unique pharmaceuticals,[22] and the pharmaceutical industry has over 7000 pharmaceuticals currently in development worldwide.[23] This increase in revenue and number of compounds correspond to an increasing use of pharmaceutical compounds worldwide. Global antibiotic usage increased by 65% from 2000 to 2015, particularly in low-mid GDP countries as shown in **Figure 1.2**.[21] Similar increases in pharmaceutical usage have been reported for many other classes of compounds. Global use of ADHD medication tripled from 1993 to 2003,[24] and opioid analgesic use more than doubled worldwide from 2001 to 2013.[25]

The worldwide increase in pharmaceutical usage has undoubtedly contributed to positive health outcomes for many individuals; however, there is a growing concern that many of these compounds contaminate water supplies, which leads to a number of downstream negative consequences. Multiple studies have identified that pharmaceutical compounds are not sufficiently degraded by current wastewater treatment facilities (WWTFs), which use a combination of biological treatment, electrocoagulation, coagulation, and membrane filtration processes.[26,27] Urban WWTFs have been one of the biggest sources of antibiotics released into the environment and have been connected to higher rates of antibiotic resistant bacteria.[6] Other work has shown that many of these compounds inhibit the survival and reproduction of algae and fish, which are the basis for aquatic ecosystems.[28] Furthermore, many pharmaceuticals end up being recycled into drinking water supplies, such that a low-dose cocktails of pharmaceuticals are consumed by people on a daily basis. One study, which analyzed tap water from 19 U.S. water facilities serving 28 million people, found measurable concentrations of 11 pharmaceuticals at the ng/L level, including sulfamethoxazole (an antibiotic) at 12 ng/L.[29] It's unclear if the compounds found in this study led to adverse health outcomes, but given the large and growing number of pharmaceuticals which are consumed, the risk of this possibility is only growing.

A growing body of research has identified so-called advanced oxidation processes (AOPs) as a technological solution to address this problem. AOPs have the ability to degrade most organic species via the in-situ generation of oxidizing species (e.g., $OH\cdot$, H_2O_2, $O2\cdot$, O_3 HOCl, etc.), which can be generated through photochemical or electrochemical means.[30–32] These processes have several advantages, such as they: (1) do not require the addition of chemicals,

only of light and/or electricity, (2) are able to degrade a wide range of organic contaminants, (3) do not produce any separate waste streams, (4) can be operated at ambient temperatures and pressures, and (5) can be scaled up to treat large volumes at WWTFs or scaled down to treat small volumes at the sources of generation. Multiple studies have examined pharmaceutical degradation using AOPs for over a decade,[33–36] but recent work has highlighted that toxic byproducts (TBPs) (e.g., chlorate, perchlorate, haloacetic acids, aliphatic halides species, haloacetonitriles, and haloacetamides) formed during AOPs compromise the quality of the treated effluent.[37]

Chapter 5 and **Chapter 6** of this work provide an introduction to and research on the development of a novel electrochemical AOP scheme to treat pharmaceuticals at the source of generation: in human urine. A brief overview of the the relevant technical background and details for device fabrication are presented in **Chapter 5**. **Chapter 6** explores a novel electrochemical scheme to degrade pharmaceuticals which minimizes toxic byproducts, and presents a novel method to eliminate toxic byproducts that are generated.

Chapter 2: Solution-Processed CIGS and CZTS, Theory and Experimental Techniques

2.1 Overview of Relevant PV Device Physics

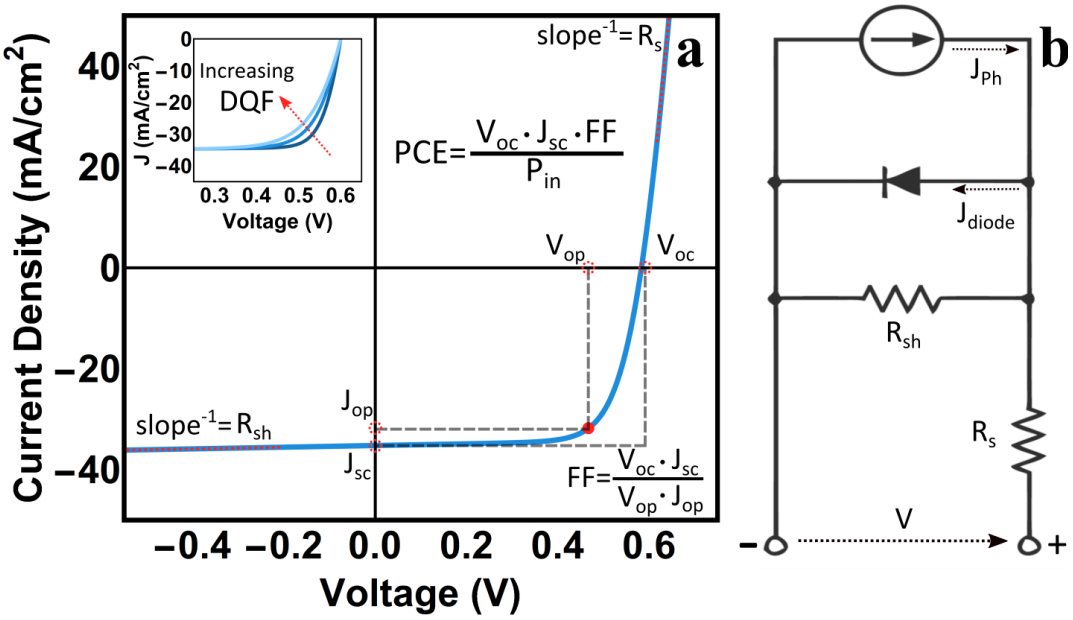

Figure 2.1 (a) Current-voltage characteristic (JV) curve from simulated device parameters of: power conversion efficiency (PCE) 14.8%, open circuit voltage (V_{oc}) 583 mV, short circuit current (J_{sc}) 35.2 mA/cm^2, fill factor (FF) 72.3%, diode quality factor (DQF) 1.5, series resistance (R_s) 4.6 Ω, and shunt resistance (R_{sh}) 5300 Ω. The red point on the curve represents the operating point, where power is maximized. Inset: Curves with DQFs of 1.0, 1.5 and 2.0 lead to progressively lower FF. (b) The simplest equivalent circuit diagram for a solar cell which where J_{ph} is the photocurrent and J_{diode} is the voltage dependent current across the diode.

This section aims to give a brief introduction to the physics of solar cells while focusing on device architectures and characterization techniques specific to solution-processed CZTS and CIGS. The overview of PV physics in this chapter is predominantly based on the work from Scheer and Schock[38] and Nelson.[39]

The power conversion efficiency (PCE) of a solar cell is composed of four parameters: (1) open circuit voltage (V_{oc}), (2) short circuit current (J_{sc}), (3) fill factor (FF), and (4) incident power (P_{in}). These can be measured by shining light on a device, applying a range of bias

voltages, and measuring the current response as shown by the current-voltage characteristic (JV) curve in **Figure 2.1a**. Incident power is the total integrated energy of all photons hitting the device. For testing, this is standardized to 1000 W/m^2 for simulated sunlight, which is spectrally matched to the AM1.5 spectrum. The operating point of the solar cell is given by the position on the curve where the current-voltage product (i.e., power) is maximized. FF is defined by equation shown in the bottom right of **Figure 2.1a** and has three contributing factors: (1) shunt resistance (R_{sh}), (2) series resistance (R_s), and (3) diode quality factor (DQF), which respectively correspond to (1) the slope of the JV curve at negative bias, (2) the slope of the JV curve at positive bias (>V_{oc}), and (3) the degree of curvature of the curve near the operating point. As shown in **Figure 2.1b** Rs and and Rsh can be understood via an equivalent circuit diagram. High R_{sh} corresponds to less leakage current which opposes the flow of photocurrent. Low R_s corresponds to a highly conductive path across the whole device. A DQF of 1 corresponds to an ideal diode, and higher values lead to a decrease in FF as shown by the inset of **Figure 2.1a**. The reasons for non-ideal diodes are related to carrier recombination in the space charge region or at the junction interface as explained in detail below.

The device parameters measured by JV directly connect to the generation, recombination, and collection of photoexcited electrons and holes (collectively carriers) in a variety of ways. In general, the population of these carriers in the valence band (VB) and conduction band (CB) of the absorber layer (or any semiconductor) can be described by Fermi-Dirac statistics. The population of electrons in the CB (n) can be described by:

$$n = \int_{Ec}^{\infty} g_c(E) \; \frac{1}{e^{(E-Ef)/k_B T}+1} \qquad \textit{Equation 2.1}$$

where, g_c is the density of allowed electron states in the CB, f is average probability that an electron state will be occupied, E is the energy of that state, k_B is the Boltzmann constant, T is temperature, and E_f is the Fermi level. In the dark, the carriers in both bands can be described by a single Fermi level (Ef) according to Equation 2.1 and an analogous expression for holes in the VB. When photons with sufficient energy are shined on a semiconductor ($E_{photon}>E_g$), electrons from the VB will be excited to the CB, increasing the population of holes in the VB and electrons in the CB above their equilibrium value. These photoexcited carriers rapidly come to equilibrium within each band at timescales much faster than they recombine: establishing a quasi-equilibrium in each band. In this excited state, the carrier population in each band can be described by two quasi-Fermi levels (Ef_n for electrons and Ef_p for holes). The difference in these quasi-Fermi levels, or the quasi-Fermi level splitting (QFLS), represents the difference in chemical potential between the photoexcited carriers and establishes the maximum amount of useful work that can be extracted from each electron-hole pair. Therefore, the upper limit of V_{oc} of a PV device is defined by QFLS/q (where q is the charge of the electron). To perform useful work outside of a device, gradients in the quasi-Fermi levels must be established to drive carriers outside of the device so that they can do useful work. For most device architectures, this is accomplished a via a PN junction to induce band-bending (i.e., drift current) and carrier selective layers on each side of the absorber layer (which establish diffusion currents). The J_{sc} of a PV device is defined by the rate that electron-hole pairs are driven out of the device and transported to the external circuit. Shockley and Queisser first described a detailed balance radiative limit for single junction PV devices assuming: (1) each photon $E_{photon}>E_g$ is absorbed and leads to an electron-hole pair, (2) photoexcited carriers only combine via unavoidable radiative

recombination (i.e. DQF= 1), (3) photoexcited carriers are transported to the external circuit without loss (i.e. R_s=0 R_{sh}=∞), and (4) the upper limits of V_{oc} and J_{sc} described above.[40] This analysis is useful to determine the upper limit for PCE and other device parameters (abbreviated PCE_{SQ}, $V_{oc,SQ}$, $J_{SC,SQ}$, etc.) for a given absorber bandgap.

2.2 Deviations from the Radiative Limit for CZTS and CIGS Devices

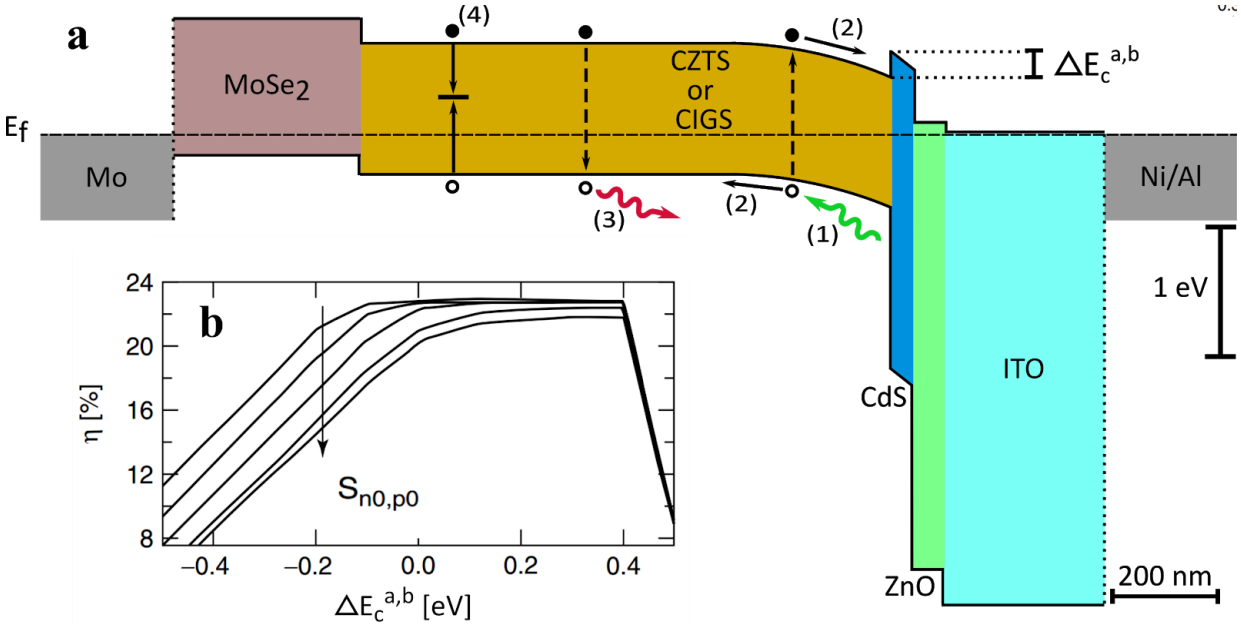

Figure 2.2 (a) Scaled band diagram of the CZTS/CIGS device at equilibrium. Band offsets are based on published data.[38,41–43] (1) A photon with sufficient energy will excite an electron from the conduction band to the valence band. (2) Photogenerated carriers are driven apart by the gradient in the Fermi level caused by band bending and alignment. (3) Carriers combine radiatively emitting a photon. (4) Carriers combine non-radiatively at localized defect states within the band gap. (b) Models reproduced from Scheer and Schock, highlighting the impact of interface recombination velocity and absorber/buffer conduction band offset ($\Delta E_c^{a,b}$) on device parameters.

In real devices, there are many non-idealities which reduce device performance below the radiative limit. Reflection of photons off of the front surface, absorption of photons by upper layers (e.g., CdS for our CZTS and CIGS devices), and incomplete absorption for $E_{photon}>E_{g,abs}$ (i.e., a non-step-function absorptivity) reduce the number of photoexcited carriers compared to

the radiative limit. In all but the best devices, quasi-equilibrium photocarrier populations are defined by non-radiative recombination pathways which are orders of magnitude faster than radiative recombination. Shockley and Read[44] and Hall[45] first derived relations which connect the non-radiative (SRH) recombination pathways via localized states which exist in the bandgap (process (4) in **Figure 2.2a**). These states are due to defects from a perfect crystal such as point defects (i.e., Cu on a Zn site, abbreviated Cu_{Zn}), grain boundaries, and interfaces. The energetic location of a mid-gap state determines how effective it is as a SRH recombination center, and mid-gap states generally lead to the highest non-recombination rates. The rate of SRH recombination depends on the position of the quasi-Fermi levels. This can lead to so-called Fermi level pinning, where the splitting of quasi-Fermi levels proceed until a population of defects becomes efficient SRH recombination centers, which inhibits further quasi-Fermi level splitting.

There are a number of techniques which have been developed to reduce non-radiative recombination CIGS and CZTS. Absorbers are deposited off-stoichiometry (Cu-poor for CIGS and Cu-poor and Zn-rich for CZTS) to minimize the the population of defects which are efficient SRH recombination centers. Sodium doping has been shown to passivate grain boundaries in both CIGS and CZTS.[46,47] Tuning the conduction band offset at the absorber buffer interface ($\Delta E^{a,b}$) reduces cross-recombination processes where electrons from the CdS recombine with the holes in the absorber as illustrated by **Figure 2.2b**. . The band diagram of **Figure 2.2a** depicts a positive $\Delta E^{a,b}$ ~0.2-0.3 eV, which is the case for CIS and CIGS absorber.[38,41,42] For CZTS, multiple conflicting values of $\Delta E^{a,b}$ have been reported, which may be related to processing techniques and/or surface chemistry. A number of reports measured $\Delta E^{a,b}$ of ~0.5 eV for CZTSe

(band gap of ~1 eV).[48,49] The large CBO is expected to act as a barrier to electrons in the conduction band and reduce device performance as illustrated by **Figure 2.2b.** The majority of highest PCE CZTS devices have band gaps near 1.15 eV (due to alloying with other elements), which is commensurate with this explanation. The biggest barrier to high PCE CZTS devices is a low V_{oc} compared to the radiative limit. This so-called voltage defecate likely has a number of contributing factors including: (1) potential fluctuations and bandgap fluctuation due to Cu/Zn disorder, (2) Sn-related defects which lead to Fermi level pinning, and (3) secondary phases.[50–54]

2.3 An Overview of Solution-Processing Techniques for CIGS and CZTS

A number of solution processes for chalcogenide semiconductors have been developed to deposit CIGS and CZTS absorber layers for PV devices including, nanocrystal (NC) inks,[55] electrodeposition,[56] colloidal suspensions,[57] and molecular ink processes.[15,58–67] Sintered layers of NC inks were the first of these routes to be developed in 2008.[55,68] Despite promising initial results, device PCEs from this route have been limited by fine-grained, carbon rich layers containing graphitic carbon from the pyrolization stabilizing ligands, which have proven very difficult to avoid.[69,70] These results represent a challenge common to any solution process when depositing an electronic material: solvents, binders, ligands, complexing agents, etc. must cleanly leave upon film deposition. Since these early results, a number of molecular ink processes have been developed and have led to consistently higher device PCEs. The solvent systems for these molecular ink processes can be divided into four major categories: (1) hydrazine,[15,58] (2) polar protic (H_2O, CH_3OH, methoxyethanol),[59,60] (3) amine-thiol,[61] and (4) polar aprotic (DMSO[62–65] and DMF[66,67,71]). Hydrazine-based solution routes hold the record for CZTS and CIGS devices as

shown in **Table 1.1**. The key advantage of hydrazine is that it can directly solvate metal chalcogenides and leave cleanly upon annealing; however, the toxic and explosive nature of hydrazine likely makes it prohibitively expensive for scale-up. Our group first developed DMSO-based and DMF-based molecular inks[62] (using thiourea (TU) as both complexing ligand and sulfur source) for chalcogenide semiconductor film formation since the solvent and sulfur source combination: (1) lacks a reactive oxygen site and thus avoids the formation of metal-oxygen-metal bonds (which can be hard to fully exchange with sulfur or selenium), (2) has high dipole moments and can solubilize many inexpensive metal salt precursors for the main elements and dopants,[64,72] (3) contains multiple different character Lewis base sites, which can help coordinate different size and hardness metal cations in solution, and (4) is much safer and more environmentally friendly than hydrazine.

The goals of the research presented in **Chapters 3 and 4** is to expand our understanding of the physical and chemical processes involved in the solution-processing of CIGS and CZTS from DMSO/DMF molecular inks, with the end-goal of improving device PCE. For CIGS, the moonshot goal is to achieve PCEs which approach vacuum-quality CIGS or hydrazine-based CIGS with a DMF- or DMSO-based solution-route. For CZTS, the moonshot goal is to improve device PCEs past the long-standing hydrazine-based PCE record. If either of these goals are achieved, it would be an important step forward toward ultra-cheap PV which can rapidly proliferate.

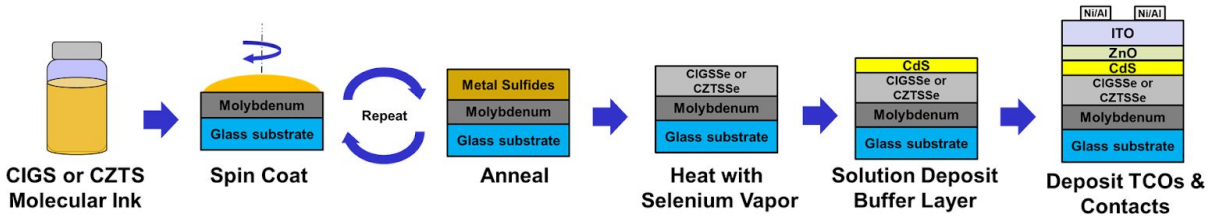

Figure 2.3- Schematic of major steps included in device-making from molecular ink solutions.

The 'molecular inks' described in this work consist of solutions of metal salts and chalcogen sources (typically thiourea), dissolved in aprotic solvents (DMF/DMSO). Thin films of metal sulfides are deposited onto molybdenum coated soda-lime glass substrates via spin coating of the molecular ink followed by annealing on a hot plate. This is repeated 3-15 times to build up the desired thickness, typically 1-2 µm. Following metal sulfide deposition, films are typically selenized: heated to ~540 °C with elemental selenium in a vented graphite box inside a tube furnace. This processing step displaces much of the sulfur in the film, replacing it with selenium. It also significantly increases grain size and improves the optoelectronic quality of the film. After selenization, the substrates are transferred into a heated solution of $CdSO_4$/NH_4OH/thiourea for chemical bath deposition of 40 nm CdS. The n-type CdS layer, typically referred to as the buffer layer, protects from sputter damage from the subsequent window layers. Highly resistive intrinsic-ZnO and In-doped SnO_2 (ITO) are then sequentially sputtered via RF sputtering. The role of the intrinsic ZnO is to act as a highly resistive layer ands a screen for shunting, while ITO is a heavily-doped n-type layer which induces band bending in the absorber layer. Nickel and aluminum contacts are deposited via physical vapor deposition through a shadow mask.

2.4 Characterization of Inks, Thin-Films, and Devices

Technique	Abbreviation	Description
Thermogravimetric analysis	TGA	The mass of a sample is measured as temperature changes, which gives information about evolving volatile species related to phase transitions and/or thermal decomposition reactions.
Raman spectroscopy	Raman	Monochromatic light is shined on a sample and scattered light is detected. A small amount of light is inelastic scattered due to allowed phonon transitions. This reveals chemical bonding environment of a sample.
Scanning electron microscopy	SEM	A collimated beam of electrons is rastered across a sample leading to secondary electrons which are collected and sent to a photomultiplier. This allows for the imaging of morphological features as small as 10 nm.
Energy dispersive spectroscopy	EDX	High-energy electrons excite core electrons in a sample. The subsequent x-rays are used to determine elemental composition
Powder X-ray Diffraction	XRD	A polycrystalline sample is illuminated with X-rays, and diffracted X-rays are collected for a range of angles of incidence/collection. X-rays constructively interfere according to this angle and the spacing between crystalline planes of the sample. This reveals information about the crystal structure of the sample.
Photoluminescence	PL	Light with sufficient energy to excite electrons from the valence band to the conduction band is shined on a sample. Light is emitted from the sample via radiative recombination of carriers. The intensity and spectral components of the emitted light give information about the optoelectronic properties of the sample.
Absolute intensity photoluminescence	AIPL	PL spectra are calibrated with black body spectra, which allow for the PL intensity to be converted to absolute units [photons/(s·m2·eV)]. Applying models to these data can yield a variety of information about the sample including PL quantum yield (PLQY) and quasi fermi level splitting (QFLS).
Current Voltage Analysis	JV	Electrical contact is made to a complete solar cell, a range of bias voltages are applied to the solar cell and the current is measured. This is used to extract the power conversion efficiency and other device parameters as shown in **Figure 2.1**a
External quantum efficiency	EQE	Monochromatic light is shined on a PV device and the current is measured. This is performed for a range of wavelengths and compared to a reference diode with known responsivity. This reveals what percentage of electron hole pairs are collected as a function of photon wavelength.
Mixing calorimetry	Calorimetry	Heat flux from a sealed vessel is measured as two individually solvated species are mixed. This reveals the enthalpy of interaction of these two species.

Table 2.1 A summary of analytical techniques presented in **Chapters 2-4**

The CZTS and CIGS molecular inks are characterized in a number of ways. A detailed discussion of all these techniques is omitted for the sake of brevity; however, **Table 2.1** gives a brief overview of the techniques to characterize solutions and thin-films discussed in **Chapter 3** and **Chapter 4** of this work. In addition to the above techniques, glow discharge optical emission

spectroscopy (GDOES) has proved an exceptionally useful tool to quickly measure depth dependent elemental profiles for precursor and selenized thin-films. To quantify the impurities in these layers, I developed a novel calibration technique which tracks the depth-dependent impurities as discussed in **Chapter 3**.

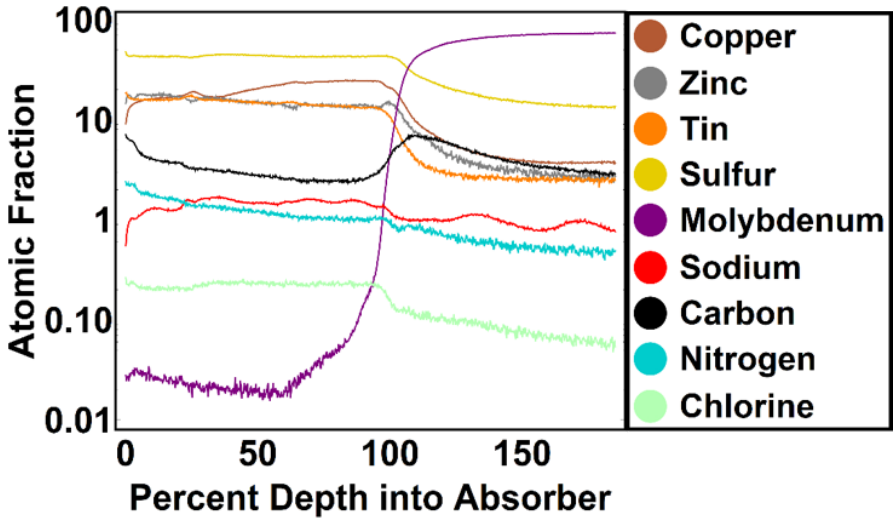

Figure 2.4 Calibrated GDOES depth-profile of a CZTS precursor film reveals the atomic composition of intrinsic constituents and impurities as a function of depth

To examine a sample with GDOES, it is placed onto the glow discharge source in front of the cathode, such that the sample itself acts as the cathode during sputtering. An annular anode is fixed above the surface of sample, and the interior of the anode is purged with argon gas. At the start of sputtering, a high RF voltage is applied between that anode and the sample, which is sufficient to generate an argon plasma above the surface of the sample. Atoms from the surface of the sample are sputtered away by the Ar plasma and diffuse away from the surface. High energy electrons in the plasma collide with sample atoms promoting their valence electrons to excited energy states. As these electrons relax back to the ground state, they emit light. Each element emits a unique spectrum of light according to the probabilistic distribution of allowed

energetic transitions (typically referred to as emission lines). This light is focused through a lens, passed to a diffraction grating where it is separated into spectral components, and then collected in a number of detectors which correspond to particular emission lines for elements of interest. Uncalibrated GDOES depth profiles have arbitrary units (volts) as a function of sputtering time for each element detected. The measured voltage for a given elemental emission line is related to a number of factors including: (1) the atomic concentration of the element in the sample, (2) the sputter rate of the sample, (3) the number of photons emitted per sputtered atom, (4) the re-absorption of these photons in the plasma, and (5) the optical collection efficiency. The plasma conditions (pressure, voltage, current and impedance) can drastically affect factors 2-4.

To account for the differences in sputter condition, I developed a calibration scheme which uses certified reference materials (CRMs) and EDX and ICP MS measurements from each sample. Three CRMs were used to establish initial calibration factors by sputtering for one hour and measuring the volume of each of these sputter craters profilometry. The measured sputter volume, the total integrated signal from GDOES, and known weight percents were then used according to Equation 2.2 to determine calibration factors for the elements of interest in each sample.

$$\frac{\frac{\rho V\ Wt\%_i}{MWT_i}}{Total\ Signal\ Ele_i}\left(units\colon \frac{mols}{V * s}\right) \qquad \textit{Equation 2.2}$$

As discussed above, emission yield varies based on the composition of the plasma (a matrix effect); therefore, calculating elemental ratios using the CRM cal. factors alone does not match what is measured from EDX and ICP-MS of CZTS films. Therefore, a correction to the CRM

calibration factors was performed such that the ratio of the integrated signals in the absorber matched the ratio measured from ICP-MS or EDX as shown in Equation 2.3.

$$Cu_{Cal.Factor,j} = Zn_{Basis\ Factor} \frac{Cu_{ICPMS,j}}{Zn_{ICPMS,j}} \frac{Zn_{\int\ GDOES,j}}{Cu_{\int\ GDOES,j}}$$

Equation 2.3

Once the calibration factors were established, they were used to calculate the molar sputter rates for each element as a function of depth. The depth dependent elemental ratios were calculated by taking the ratio of these depth-dependent molar sputter rates. The depth-dependent concentrations of impurities were calculated by dividing the depth-dependent molar sputter rate of a given impurity by the total depth-dependent molar sputter rate.

Chapter 3: Evolution of Morphology and Composition during Annealing and Selenization in Solution-Processed Chalcogenide Thin-Films

3.1 Introduction

The CZTS DMSO molecular inks consisting of Cu, Zn, and Sn salts and thiourea to deposit CZTSSe absorber layers were first described by Ki and Hillhouse.[62] Xin et al. later expanded on this work to reveal the importance of redox reactions in this ink,[63] and in a subsequent report, showed that lithium-doping of the DMSO molecular ink significantly improves device PCE (up to 11.8%).[64] More recently, the EMPA reported a device PCE of 12.3% using this Li-doped DMSO molecular ink, which represents the world record for hydrazine-free solution-processed CZTS.[73] The CZTS/DMSO molecular ink process has been adopted by a large number of groups,[73–83] but many of these reports have a wide range of reported absorber morphologies. Moreover, devices in most of these studies suffer from low device PCEs (<8%), predominantly due to low fill factor. Multiple studies have shown that the multilayer morphology can be affected by a range of processing conditions including: (1) modifications to the selenization time and temperature profile,[74] (2) evaporation of NaF on the film before selenization,[76,80] (3) and multiple-selenizations of the same film.[79] Despite the prevalence of these multilayer morphologies, their chemical origin has been largely unexplored.

A major difference between the dense absorbers reported by Xin et al.[64] and the many other studies reported in the literature for the DMSO molecular ink process is the thermal anneal profile and environment before selenization. In these studies, the molecular ink is typically annealed at a range of temperatures between 250°C and 350°C in air,[73–77] nitrogen,[78,79] or not reported.[80–83] By contrast, Xin et al. reported using an hot plate set point of 540 °C in a nitrogen

environment. This work reveals that different annealing profiles during ink deposition critically affect a number of precursor properties including: (1) the metal sulfide composition and crystallinity, (2) the depth-dependent concentration profiles of impurities, and (3) the degree of polymerization of C (carbon) and N (nitrogen) containing thiourea decomposition products. Further, we show how these properties affect selenized film morphology, impurity distributions, and PV device performance characteristics.

3.2 Analysis of Molecular ink and Metal Sulfide Precursor Films

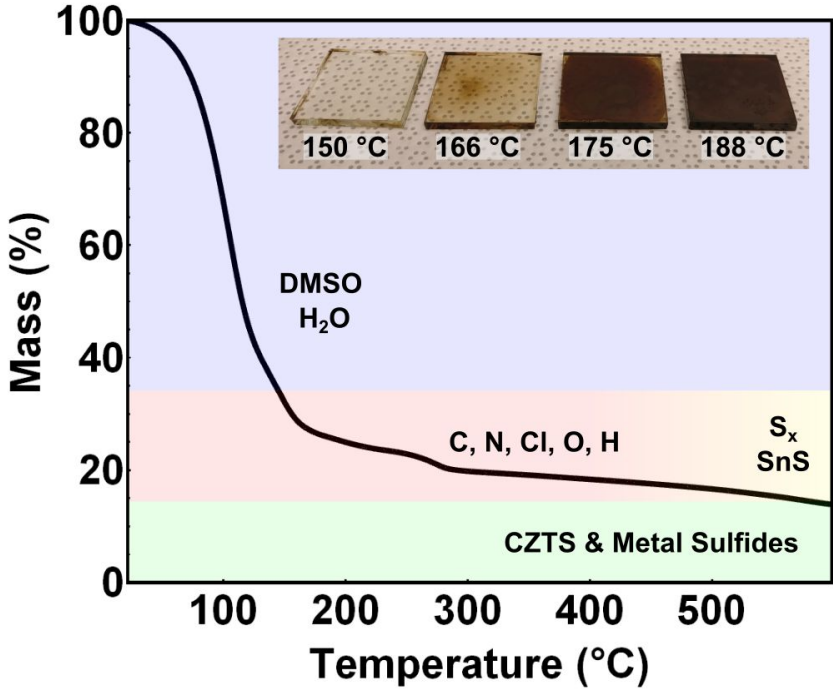

Figure 3.1 TGA of the DMSO molecular ink heated in N_2 atmosphere with a ramp rate of 1 °C/min. Plot shading indicates ink constituents: blue- evolved solvents, red- evolved impurities, yellow- evolved species due to CZTS decomposition, and green- retained metal sulfides. Plot shading corresponds to a mass balance shown in Table 3.1 below. Inset: spin-coated precursor films on glass annealed at different temperatures showing the onset of color change indicating metal sulfide formation.

Constituents	*Mass %*	*(Molecules or Atoms)/ Formula Unit CZTS*
Cu_2ZnSnS_4	14.5%	1.0
Solvents		
DMSO	63.6%	23.9
H_2O	2.3%	3.7
Solvents Total	*65.9%*	*27.5*
Impurities		
Carbon	4.5%	11.0
Nitrogen	4.6%	9.7
Chloride	5.2%	4.3
Oxygen	3.4%	6.2
Hydrogen	1.0%	28.6
Excess Sulfur	0.9%	0.8
Impurities Total	*19.6%*	*60.6*

Table 3.1: Mass and mole balance for the constituents of the CZTS DMSO molecular ink. The colored shading matches the plot shading for evolved constituents in Figure 3.1 above.

Thermogravimetric analysis (TGA) is a useful technique to study the temperature regimes of decomposition of the molecular ink. Similar to the expected complexes in this ink, Madárasz et al. examined the decomposition of Cu, Zn, and Sn hydrated chloride/thiourea complexes in air.[84] They found three regimes of decomposition: (1) dehydration of the complexes from room temperature to 180 °C, (2) complex decomposition and metal sulfide formation between 200 and 270 °C, and (3) metal oxide formation at temperatures as low as 275 °C. Films deposited from the DMSO molecular ink have been annealed in air at temperatures >275 °C in multiple studies,[74,75,77,82] which risks the oxidation of the metals to some extent and otherwise affects decomposition pathways. TGA of the CZTS/DMSO molecular ink under constant N_2 flow from 25-600 °C was performed to track the stages of degradation in an inert environment as shown in **Figure 3.1**. A summary of a mass balance of these precursors' constituents is presented in **Table 3.1**. From 25-150 °C, 66% of the mass had been lost, which corresponds to the mass percent of DMSO and H_2O in the ink as shown in the blue shaded region of **Table 3.1**. 150 °C is also

below the onset of the formation of light-absorbing metal sulfide species as shown in the inset of **Table 3.1**. This suggests that the DMSO and water-of-hydration in the precursors cleanly volatilize from the film without decomposing. From 150°C to 500 °C, the primary source of mass loss can be attributed to the decomposition and volatilization of the thiourea, chloride, and acetate species, which is indicated by the pink shading. Note that from 260°C to 280°C, there was a notable increase in the rate of mass loss, indicating that this is a critical temperature for impurity removal. At the higher temperatures (>500 °C) the decomposition of CZTS into binary metal sulfides is expected as described Scragg et al.[85] This decomposition is accompanied by the volatilization of S_x and SnS, which is indicated by the yellow shading in **Figure 3.1**. Near 580 °C, the mass percent was approximately equal to 14.5%, which corresponds the mass percent of CZTS as shown in **Table 3.1**. However, given that some portion of the mass loss can be attributed to S_x and SnS vaporization, this suggests that some impurity elements remained in the film even at these highest temperatures.

The TGA ramp of 1 °C/min up to 600 °C leads to a much higher thermal exposure than the brief anneals between spincoated layers. During TGA, the material spends 300 min above 300 °C, 200 min at about 400 °C, and 100 min above 500 °C. By contrast, films are only annealed at a maximum of 3 min/ layer (i.e. 21 min total exposure) during spin-coating in this study. Thus, the TGA data are a useful upper limit for impurity removal in a spin-coated thin film, since the impurities have a larger potential time window to volatilize. In the following sections, a number of annealing profiles with varying time and temperature between spin-coating layers were explored to determine the effects of these impurities on precursor films, CZTSSe absorbers, and PV device performance.

3.3 Chemical Composition Morphology and Crystallinity of Precursor Films

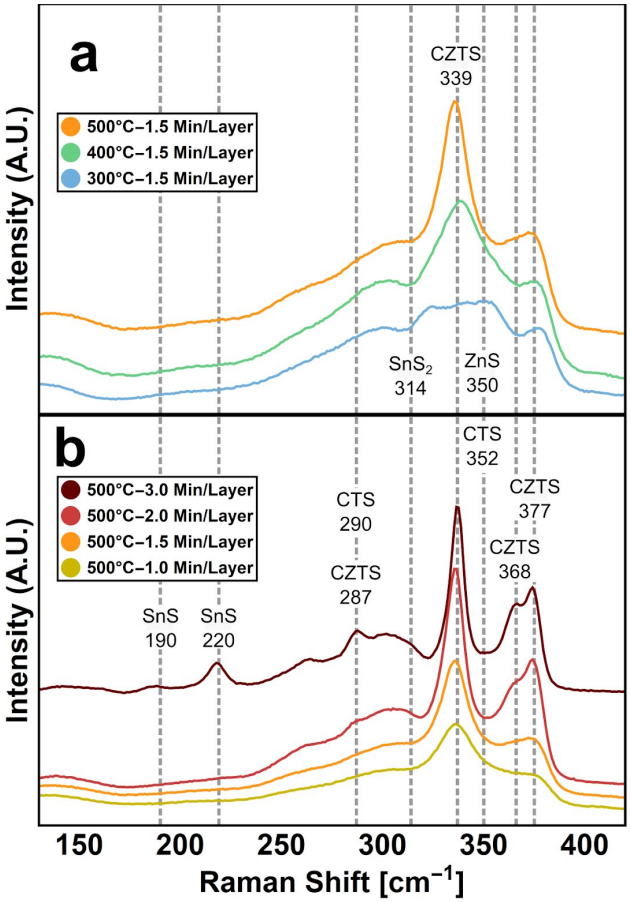

Figure 3.2 Near-resonant Raman spectra of precursor films annealed for different temperatures and times. Gridlines are indicative of major peaks attributed to the indicated metal sulfides. Films are composed of increasing amounts of CZTS with increasing anneal time and temperature.

Near-resonant Raman spectra of CZTS films with various annealing conditions show a clear difference in the metal sulfide phase distribution as shown in **Figure 3.2**. A number of metal sulfides exhibit Raman bands from 250-400 cm^{-1} including: ZnS (350 cm^{-1}), monoclinic Cu_2SnS_3 (CTS) (290 and 352 cm^{-1}), SnS_2 (314 cm^{-1}), and CZTS (289, 339, 368, and 377 cm^{-1}).[86–88] Given that the Raman bands for these species have many peaks and shoulders which overlap, is it difficult to deconvolute the spectra in **Figure 3.2** to determine the exact quantity of each of these

phases. However, there are clear trends in the relative peak intensities with changing annealing time and temperature. As shown in **Figure 3.2a**, the ratio between the primary CZTS peaks at 339 cm^{-1} and the primary peaks for ZnS and CTS near 350 cm^{-1} substantially increase with increasing annealing temperature. Thus, films annealed at higher temperatures are composed of more CZTS and less secondary phases. This trend continues for increasing annealing times at 500 °C as shown in **Figure 3.2b**. For longer durations, all CZTS peaks become sharper and more prominent in comparison to the broad background from 250-400 cm^{-1}. Exclusively for the longest annealing condition (500 °C-3 min/layer), peaks appear at 190 cm^{-1} and 220 cm^{-1} which can be attributed to SnS.[86,87]

The amount of CZTS formed in the precursor film is closely related to the crystallinity of the film as indicated by XRD in **Figure 3.3a,b**. For annealing temperatures at or below 400 °C, little to no crystallization of the metal sulfide precursor film is visible. However, at 500 °C, the film is readily crystallized, and crystallization increases with increasing annealing time. It is noted that because of the overlapping diffraction patterns, the crystalline phases of Cu_2ZnSnS_4, ZnS, and monoclinic $CuSnS_2$ cannot be distinguished by XRD. Despite the differences in phase distribution and crystallinity, SEM results of all precursor films annealed at different conditions look identical, except for the 500 °C for 3 min/layer condition. For all except this condition, precursor films have a porous, flat morphology with features <50 nm. Precursor films annealed at 500 °C for 3 min/layer exhibit a heterogeneous morphology with 2 μm agglomerations appearing every ~10 μm across the surface of the film as shown in **Figure 3.4a,b**.

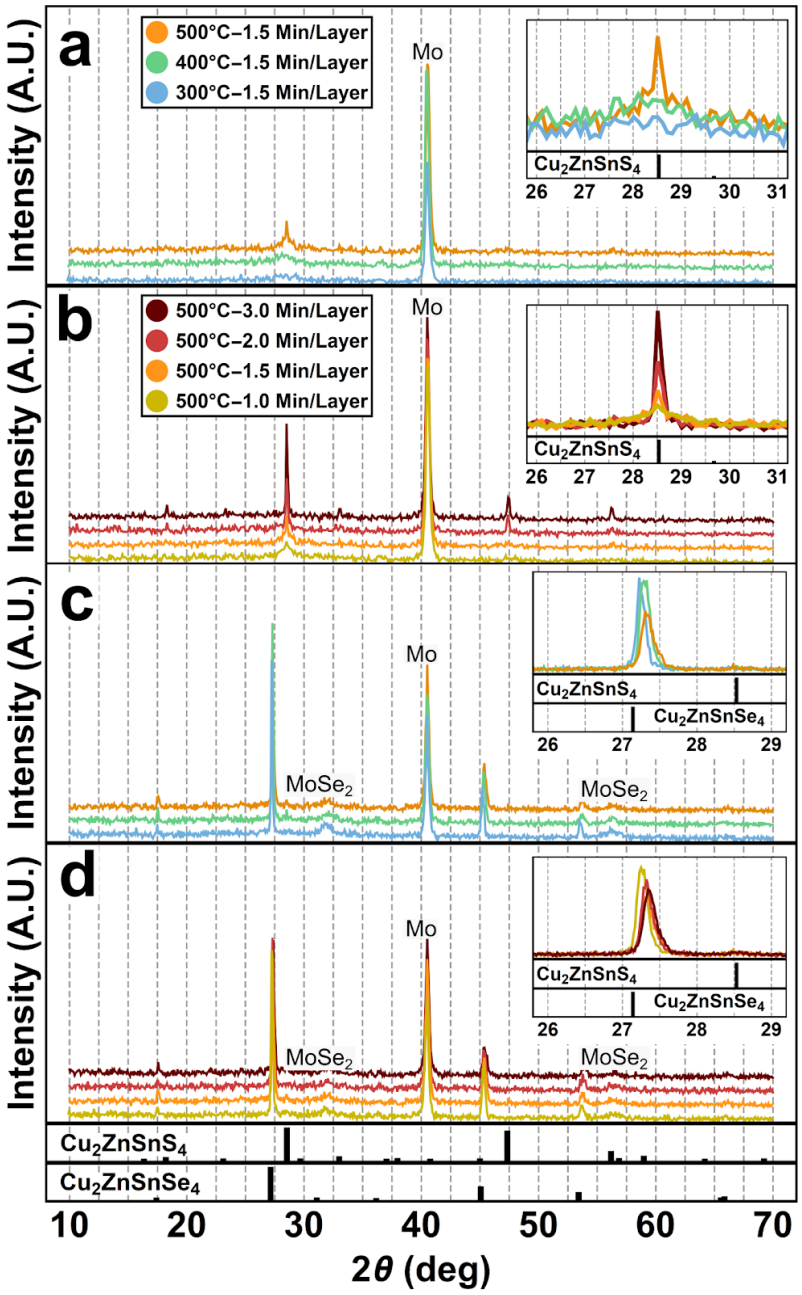

Figure 3.3 XRD patterns for precursor films (a, b) and CZTSSe films after selenization (c, d) annealed at different conditions after spin-coating. Films are increasingly more crystalline with increasing annealing temperature (a) and increasing annealing time at 500 °C (b). After selenization, a peak shift toward higher 2θ angle with increasing annealing temperature at 1.5 min/layer (c) and with increasing annealing time at 500 °C (d) is apparent which indicates increasing S/(S + Se).

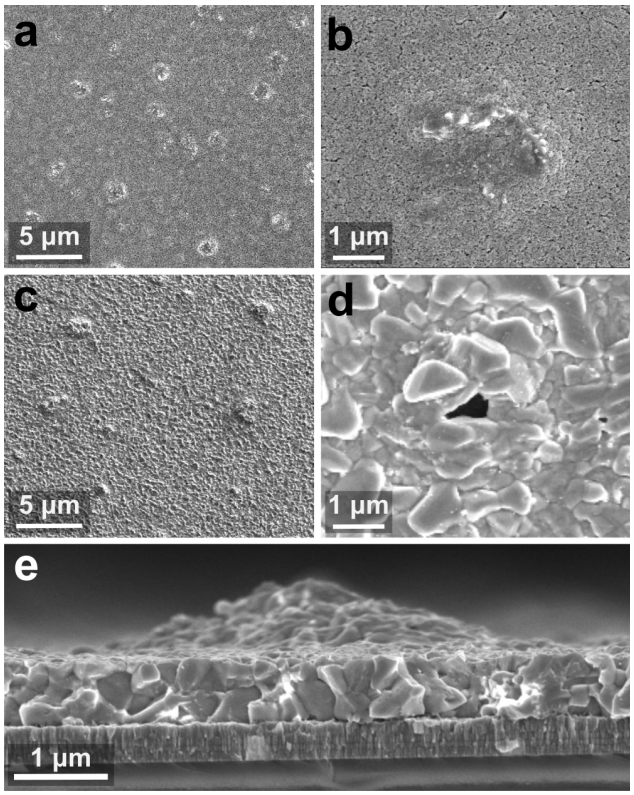

Figure 3.4 . SEM top views of precursor (a, b) and selenized (c−e) films annealed at 500 °C for 3 min/layer after spin-coating. (a, b) Precursor films have 2 µm agglomerations approximately every 10 µm. EDX and Raman results indicate that these agglomerations are SnS precipitation from the bulk. (c−e) Selenized films show raised voids across the surface with approximately same size and spacing as agglomerations on precursor films, suggesting that SnS vaporizes during selenization.

These agglomerations are significantly enriched in Sn as measured by EDX. Given that the Raman spectra suggest the appearance of SnS phase, it follows that these agglomerations correspond to precipitation of SnS from the bulk. This is consistent with a proposed decomposition pathway in which CZTS decomposes to Cu2S(s), ZnS(s), SnS(s), and Sx(v) at elevated temperatures.[85]

3.4 Chemical Composition Morphology and Crystallinity of Selenized Films

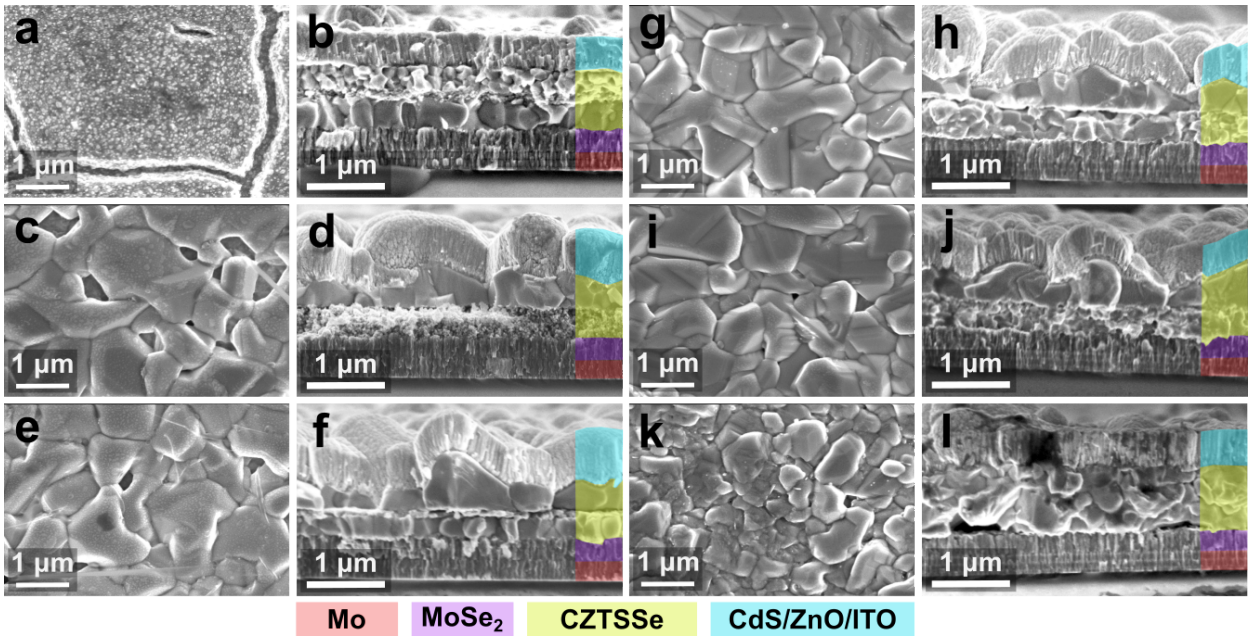

Figure 3.5 SEM of selenized films (columns 1 & 3: a, c, e, g, i, k) and cross sections of completed devices (columns 2 & 4: b, d, f, h, j, l) with each layer labeled. Annealing conditions after spin-coating: 300°C 1.5 min/layer (a, b), 400°C 1.5 min/layer (c, d), 500°C 1.0 min/layer (e, f), 500°C 1.5 min/layer (g, h), 500°C 2.0 min/layer (i, j), and 500°C 3.0 min/layer (k, l)

The crystallinity, phase purity, and the extrinsic element distribution due to different annealing conditions directly impact the physical properties of the selenized films in a variety of ways. **Figure 3.3c,d**. shows that all precursor films form crystalline $Cu_2ZnSn(S_xSe_{1-x})_4$ after selenization. The shift of the peaks toward higher 2θ with higher annealing times and higher annealing temperatures indicates an increase in the S/(S + Se) ratio. This trend was confirmed by EDX measurements. The increasing sulfur content in the selenized films seems to directly correlate with the degree of crystallization in the film before selenization. Despite being more

crystalline before selenization, films annealed at 500 °C appear slightly less crystalline with increasing annealing time as indicated by the peak height in **Figure 3.3c,d**.

Although there are similarities in crystallinity, the selenized films exhibit a wide variety of morphologies depending on the anneal profile after spin-coating, as shown in **Figure 3.5**. The surface of the film annealed at 1.5 min/layer at 300 °C has a cracked, small-grained top layer and a dense bottom layer (see **Figure 3.5a,b**). This morphology has not been reported for the DMSO molecular ink process; however, a similar morphology has been reported for CZTSSe absorbers where selenium was thermally evaporated onto molybdenum before deposition of solution-processed CZTS.[69] As discussed in that work, this morphology is likely indicative of a bottom-up grain growth mechanism where impurities are expelled toward the surface of the film during selenization. The film annealed at 400 °C (**Figure 3.5c,d**) has a morphology commonly presented in the literature for the DMSO molecular ink process, with a large grained upper layer and a fine-grained bottom layer.[63,74,75,82] The bottom layer exhibits a morphology with grains <50 nm. A second film annealed at 3.0 min/layer at 400 °C exhibited a similar morphology suggesting that this regime of grain growth is indicative of the temperature rather than the annealing time.

Compared to the film annealed at 400 °C, the films annealed at 500 °C for 1−2 min/layer exhibit a similar double layer structure, but with a denser top layer and improved grain growth in the bottom layer as shown in **Figure 3.5e−j**. The film annealed for 1 min/layer (**Figure 3.5f**) has a trilayer structure with a fine-grained middle layer and a bottom layer with ~300 nm round grains. For the 1.5 min/layer condition, this finegrained layer is not observed, and only the 300 nm round grains remain on the bottom layer. For the 2.0 min/layer condition, the grains of the

bottom layer appear smaller and much less faceted. Finally for the 3.0 min/layer condition, the multilayer morphology is gone, but the entire film exhibits a morphology with smaller grains and less crystal faceting. As shown in **Figure 3.4c−e** the surface of the film has raised voids with the same size and spacing as the SnS precipitation in the precursor film. Thus, the raised voids are attributed to the evaporation of the SnS rich regions during selenization.

3.5 Connecting GDOES Depth Profiles with Morphology of Selenized Films

As indicated by the growing weight loss of the molecular ink with temperature in **Figure 3.1** an increasing amount of C-, N-, Cl-, H-, and O-containing species volatilize from precursor films with increasing temperature. To understand the complicated reactions and transport of these species before and after selenization, calibrated GDOES elemental depth profiles were measured on precursor and selenized films for different annealing conditions as shown in **Figure 3.6**

The elemental ratio depth profiles of precursor films annealed at 300, 400, and 500 °C for 1.5 min/layer are shown in **Figure 3.6a**. For all anneal temperatures, the bulk Cu/(Zn + Sn) is constant, and all depth profiles generally show a trend of increasing Cu/ (Zn + Sn) toward the back contact. For the 500 °C condition, the Cu/(Zn + Sn) sharply decreases at the moly/precursor interface. This could be related to a reaction with CZTS and molybdenum to produce MoS and Cu_2S, ZnS, and SnS,[52] and the higher diffusivity of Cu into the molybdenum compared to these other metals. As expected with increasing anneal temperature, the bulk Zn/Sn ratio increases because of the formation of volatile SnS species and the corresponding Sn loss.[85]

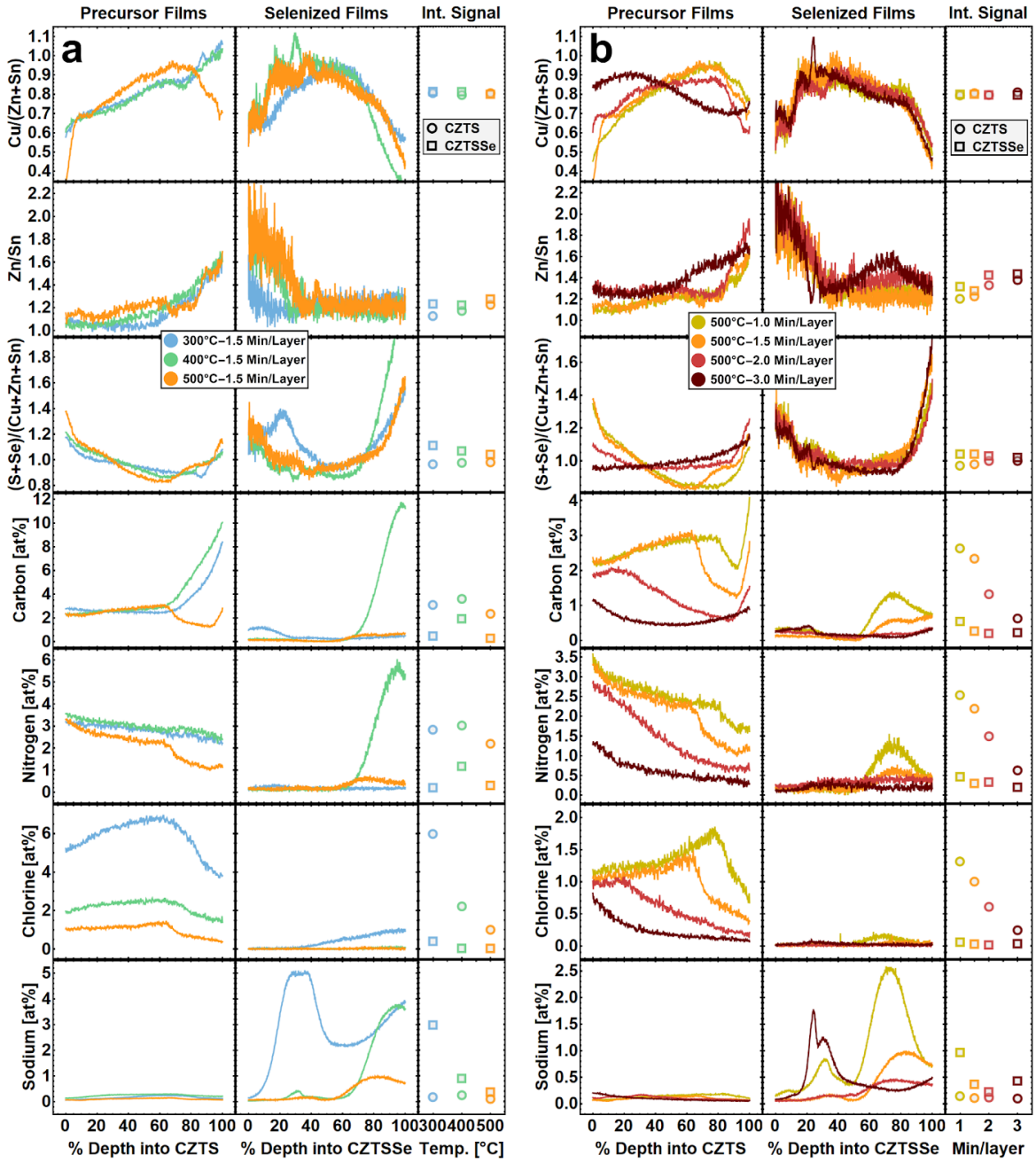

Figure 3.6 Calibrated GDOES elemental ratios and impurity depth profiles for precursor and selenized films annealed for selected annealing times and temperatures after spin-coating. Column 1 indicates precursor films, column 2 indicates selnized films, and column 3 indicates the integrated signal of the GDOES based off of ICP-MS, EDX, and GDOES calibration standards. Circles represent the precursor films before selenization, and the squares represent the selenized CZTSSe films. Full calibration details can be found in the Section 2.4.

The Zn/Sn depths profiles all show increasing Zn/Sn toward the back contact. The elemental ratio depth profiles of precursor films annealed at 500 °C for various times in **Figure 3.6b** support the above explanations of the data. Increasing anneal time at 500 °C leads to increasing Cu depletion at the back contact interface and increasing Sn loss throughout the bulk of the film.

Generally, the transport of extrinsic elements out of the precursor film during annealing is governed by the rate of multiple physiochemical processes including the following: (1) decomposition/pyrolysis of precursors, (2) diffusion of volatile products to the film's surface, and (3) desorption of species from the surface of the film. Further, the decomposition products that form and the relative rates of these processes will be significantly different for different annealing profiles. Determining which of these processes is the rate-limiting step is complicated by the effect of annealing sequential layers after spin-coating (i.e., the bottom layers receive more thermal treatment than the top layers). Despite these complications, the GDOES depth profiles of the extrinsic elements in the precursor films (see the first column of **Figure 3.6a,b**) reveal a number of interesting aspects about how the anneal profile affects the transport of extrinsic elements. C and N have similar trends for all annealing conditions, suggesting that they may be chemically related and/or covalently bound together. As shown in Figure 6a, the 300 and 400 °C conditions exhibit nearly identical C and N profiles with nearly 10 atom % carbon at the back contact interface. By contrast, the 500 °C condition has less C and N at the bottom of the film. This could suggest that the 500 °C anneal temperature is required to activate a decomposition reaction involving C and N that is not active (or much slower) at 400 °C and lower. Possible volatile products for this decomposition reaction could include HCN, $(CN)_2$, or CNCl. Increasing annealing time at 500 °C removes more C and N from the film as shown in **Figure 3.6b**. Unlike

C and N, Cl is increasingly removed from the films for all annealing conditions. This suggests that a reaction which evolves volatile chloride compounds is active at all studied annealing temperatures. Possible volatile decomposition products could include Cl_2 or HCl.

After selenization, all CZTSSe films generally show a copper-poor and zinc-rich surface. This stoichiometry is favorable for the front surface of the absorber as it supports the occurrence of (V_{Cu} + Zn_{Cu}) defect clusters, as CZTS richness in this defect cluster is predicted to lower both conduction and valence band edges.[89] The fine-grained upper layer for films annealed at 300 °C are rich in Na, Se, and some C, but have no N. By contrast, the fine-grained bottom layer for films annealed at 400 °C are rich in all of these elements. Similar to the 400 °C films, the fine-grained layer for films annealed at 500 °C contain C, N, Na, and Se, but show significantly less of these elements with increasing annealing time. A key factor for understanding how impurities affect grain growth is the interaction with sodium polyselenide (Na_2Se_x, x = 2, 3, 4, or 6). Liquid Na_2Se_x can exist at temperatures as low as 255 °C, and has been proposed as a liquid fluxing agent that can increase in grain size, as seen for Na-doped films.[47,76] Evidence also suggests that vapor-phase transport of Na_2Se_x via Se reactions with the SLG is the dominant source of Na in CZTSSe films during selenization.[90] The driving force for Na_2Se_x precipitation onto the film's surface and flux through the film is capillary condensation and capillary flow due to the nanoporosity of the film. This nanoporosity changes over the course of the selenization as grains grow. Given that impurities have been shown to impede grain growth,[69] the amount and location of Na_2Se_x in the film are closely related to the depth-dependent impurity profile in the film. This would explain why Na and Se have high concentrations in regions with small grains and decreasing concentration in areas of films with progressively larger grains. This explanation

is also commensurate with the high amount of Na and Se found in the films annealed at 300 °C, where the grain growth at the surface was inhibited at the surface for the entire duration of the selenization. In addition to the above discussion, Na_2Se_x may also react with some impurities (such as chloride) and/or act as a fluxing agent which facilitates the removal of impurities from the film. As in the precursor films, the depth-dependent trends for C and N in the selenized films show substantial correlation. Given the similar amount of C and N in precursor films annealed at 300 and 400 °C, the films annealed at 400 °C have an order of magnitude higher C and N than the films annealed at 300 °C after selenization. At 500 °C, the C and N also appear in the bottom layers of the selenized films but with decreasing amounts that correlate with their removal before selenization.

3.6 Structure of Carbon and Nitrogen Impurities in Fine-Grained Layers

In order to study the commonly reported fine-grained layer of the 400 °C annealing condition (**Figure 3.5d**), a mechanical liftoff of the CZTSSe absorber at the CZTSSe/Mo interface was performed. A schematic of the liftoff process along with top‑down SEM images of the fine-grained layer is shown in **Figure 3.7a-b**. Direct measurement of the fine-grained layer with photoluminescence (**Figure 3.7c**) and Raman spectroscopy (**Figure 3.7d**) reveals three features characteristic of an amorphous hydrogenated carbon nitride (a-C:H:N) network: (1) overlapping peaks ranging from 1100 to 1700 cm^{-1} corresponding to the D and G Raman scattering peaks in a graphitic structure,[91] (2) a small peak centered at ~2200 cm−1 attributed to the CN stretching band,[92] and (3) the broad photoluminescence peak from 1.6 to 2.3 eV when exciting with 532 nm.[91]

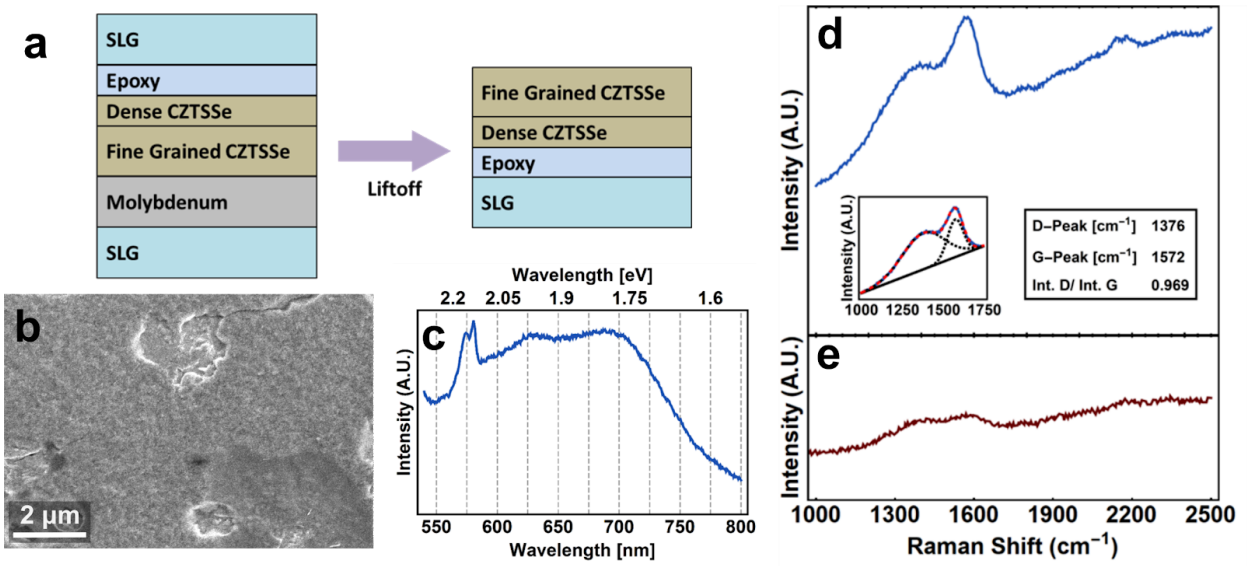

Figure 3.7 (a) Schematic of the mechanically-exfoliation procedure to cleave samples at the CZTS/molybdenum interface. (b) Top down SEM images of the fine-grained CZTSSe layer of a film annealed at 400 °C for 1.5 min/layer. (c) Photoluminescence and (d) Raman spectroscopy of the mechanically exfoliated fine-grained layer from a 400 °C for 1.5 min/layer. (e) Raman spectroscopy of the top- surface of a CZTSSe absorber annealed at 500 °C for 3.0 min/layer. Both samples exhibit Raman characteristics of an amorphous hydrogenated carbon nitride network.

The bandgap of carbon nitride can have a wide range from 0.5 to 2.7 eV depending on the composition and degree of ordering, but compositions of ~30% N/(C + N) (which matches the composition from GDOES) to values which have been shown to have a PL peak centered at 2.1 eV.[92–94] These data indicate that the C- and N-rich material that was discovered with GDOES is an a-C:H:N network. The source of this a-C:H:N network can be attributed to the polymerization of thiourea. Upon heating to 250 °C in an oxygen free environment, thiourea is known to decompose to CS_2, NH_3, and the heterocyclic triazine compound, melamine ($C_3H_6N_6$),[95] and heating further to 400 °C has been shown to polymerize melamine into C- and N-containing heterocyclic polymer networks.[96] Raman measurements of the precursor films (shown in Figure S8 of the appendix), show peaks at 670 and 970 cm^{-1}, which are characteristic of melamine and

oligomers of melamine such as s-triazine.[97,98] While the precursor films annealed at 300 and 400 °C have similar amounts of C and N, it is expected that these films have different degrees of polymerization of heterocyclic triazine networks. Given the differences in C and N after selenization for these conditions, it follows that melamine with a higher degree of polymerization less readily decomposes during selenization. Annealing at 500 °C likely leads to higher molecular-weight oligomers of melamine. However, this formation mechanism is also countered by a decomposition pathway that occurs at this temperature during annealing, as shown by the GDOES data. The films that were annealed at 400 °C likely have the most C and N because this is within the temperature window where the polymerization of melamine is maximized, and the decomposition that is seen at 500 °C is less pronounced. The C and N are below the detectable limit of GDOES in the CZTSSe film annealed at 500 °C for 3 min/layer; however, Raman spectroscopy of this film shows weak characteristics of a-C:H:N as seen in **Figure 3.7e**. This suggests that the a-C:H:N network has been incorporated into the CZTSSe film, which might also explain the less-faceted morphology seen in **Figure 3.5k, l**.

3.7 Device Performance

As seen in **Table 3.2**, the different anneal profiles lead to significantly different device performance characteristics. Devices made from films annealed at 300 °C for 1.5 min/layer exhibit the lowest PCE due to low V_{oc} and FF which is likely due to the high SRH recombination in the space-charge region due to the fine-grained upper layer. Devices made from films annealed at 400 °C have low PCE and FF, matching reported examples of samples with a fine-grained layer.[80–82] The porous fine-grained layer toward the back contact reduces the fill factor by drastically increasing the series resistance and diode quality factor (DQF).

Temp [°C]	Time [min /layer]	PCE [%]	V_{oc} [V]	J_{sc} [mA/cm^2]	FF [%]	R_s [Ω]	R_{sh} [Ω]	DQF
300	1.5	5.49 ± 1.38	0.385 ± 0.034	30.2 ± 3.7	46.7 ± 5.4	11.2 ± 11.5	1500 ± 1270	3.24 ± 0.58
400	1.5	5.74 ± 2.18	0.422 ± 0.016	30.8 ± 3.7	43.2 ± 11.6	41.2 ± 34.5	2620 ± 1980	N/A
500	1.0	7.73 ± 0.86	0.438 ± 0.006	33.7 ± 1.2	52.3 ± 4.5	6.9 ± 6.0	2990 ± 980	3.14 ± 0.94
500	1.5	8.04 ± 1.08	0.430 ± 0.010	32.7 ± 2.8	57.1 ± 4.6	5.0 ± 1.0	1650 ± 1300	2.05 ± 0.23
500	2.0	7.56 ± 0.63	0.426 ± 0.011	29.8 ± 1.4	59.7 ± 4.7	5.4 ± 0.7	2710 ± 2060	1.90 ± 0.16
500	3.0	7.39 ± 1.38	0.419 ± 0.018	32.7 ± 2.4	53.5 ± 5.4	6.3 ± 4.9	1790 ± 1460	2.64 ± 0.96

Table 3.2 Summary of CZTSSe photovoltaic device characteristics for various anneal conditions. The device parameters presented for each sample are average values and standard deviations from 20 solar cells with a MgF_2 anti-reflective coating and an active area averaging 0.105 cm^2. The diode quality factor (DQF) for the 400 °C conditions is listed as N/A due to the fact that some devices in this condition exhibited a double-diode-type barrier that prevented an unambiguous diode quality factor from being determined.

The DQF for the 400 °C conditions is listed as N/A due to the fact that some devices in this condition exhibited a double-diode-type barrier that prevented an unambiguous diode quality factor from being determined. For the 500 °C at 1, 1.5 and 2 mins/layer conditions, there is a clear trend of increasing FF and decreasing V_{oc} with increasing anneal time. The FF increase could be due to a decrease in an C and N rich layer (**Figure 3.6**), while the V_{oc} decrease could be due to an increase in a-C:H:N incorporation into the bulk of the absorber (**Figure 3.7e)**. For the 500 °C at 3 min/layer condition, the FF is worse due to the large voids related to SnS vaporization. The tradeoff between all of these effects leads to the highest average device performance for the 500 °C 1.5 min/layer condition, with a champion devices of 10.7%. In addition to the six conditions shown in **Table 3.2**, devices were made for films annealed at 300 °C at 3 min/layer and 400 °C at 3 min/layer after spin-coating. Notably, the annealing condition of 300 °C at 3 min/layer had average device PCE close to all of the 500 °C anneal conditions and a single device with 10.5% PCE, which shows that multiple optima might exist for high PCE devices.

3.8 Lithium Doping's Effect on Sodium Transport

In Xin et al.'s first report on Li-doped CZTSSe, both the Li-free and the Li-doped samples exhibited dense monolayer morphologies using an anneal profile of 500 °C at 2 min/layer.[64] Our previous reports with nearly identical conditions all contained multilayer morphologies,[62,63] similar to what is presented in **Figure 3.5** (which has no dopants added to the ink). Here, we use GDOES to show how Li-doping affects elemental distribution in the film and the Na concentration as a function of depth. A dopant-free ink and a 2.5% LiCl/metals ink were prepared and spin-coated to form a precursor film. The depth profiles for nearly all elements were identical, with the exception of Na and Li as shown in **Figure 3.8**. As expected, the Li-doped film exhibited a high amount of lithium in the precursor film while the dopant free film had none. Surprisingly, the lithium was also measured in high concentrations in the molybdenum and a small amount was measured in the soda-lime glass (**Figure 3.8b**). The depth profiles also show that the Li-doped film contains approximately double the amount of Na (**Figure 3.8a**) This suggests that Li displaces Na in the SLG and this Na then diffuses into the bulk of the precursor film. This explanation is commensurate with the free energy of formation of Li_2O (-562.1 kJ/mol) and Na_2O (-377.1 kJ/mol).

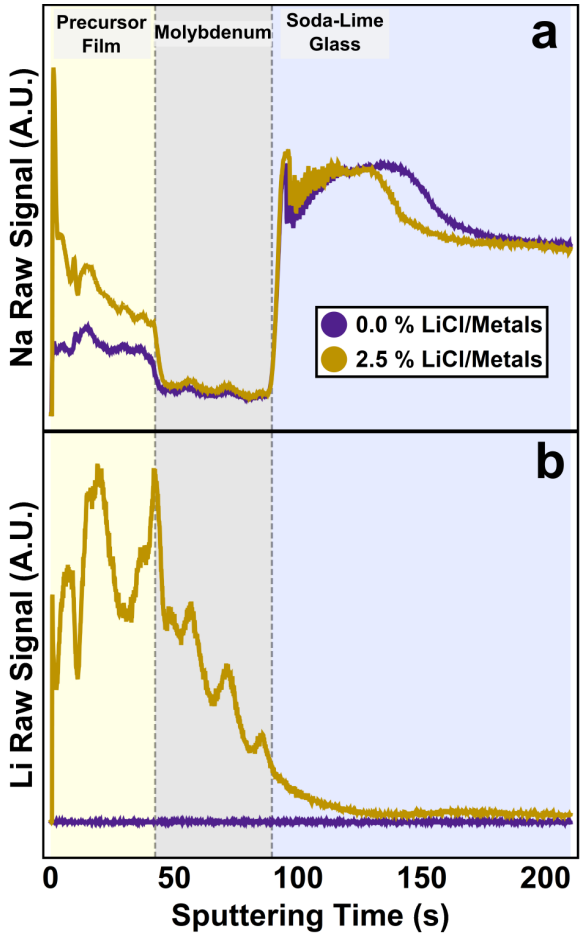

Figure 3.8 (a,b) GDOES depth profiles of precursor films with and without LiCl doping. Yellow shading represents the metal sulfide precursor film, grey shading represents the Mo, and the blue shading represents the SLG. (a) Films doped with lithium show significant sodium enrichment of precursor films. (b) Lithium from precursor film diffuses into the SLG and displaces sodium. (c) Photograph of a CZTSSe absorber that was selenized in a graphite box previously used for Lithium-doping experiments. (d,e) SEM cross sections of (d) region 1 and (e) region 2. Note that region 2 has a significantly denser morphology. (f) GDOES depth profiles of each of these regions reveal that region 2 has significantly more sodium on the surface and decreased carbon and nitrogen throughout the depth of the absorber.

As discussed above, sodium polyselenides (Na_2Se_x) have been proposed as liquid fluxing agents which increase grain growth during selenization.[47,76] Further, there is recent evidence that these gas-phase alkali polysenides are readily transported via the gas-phase, and doping is often accidental.[99] Further, this expelled sodium is expected to contaminate the graphite box during selenization.

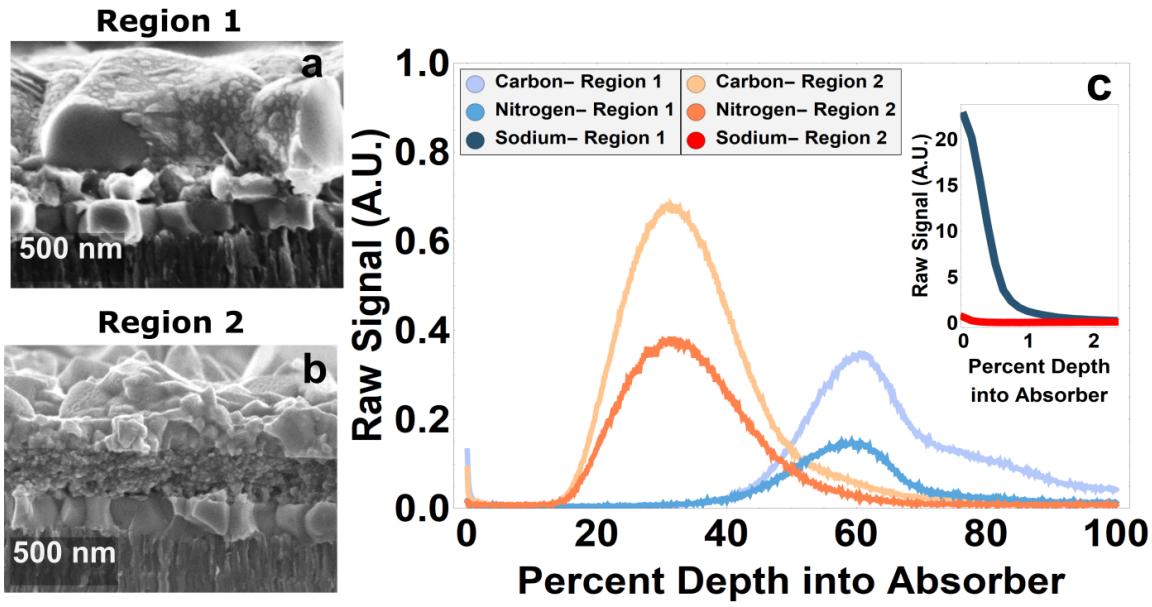

Figure 3.9 Characterization of a CZTSSe film without Li-doping that was selenized in a graphite box previously used for Li-doping experiments. (a,b) SEM cross sections of two regions of the film, where Region 1 was closer to the edge of the box. Note that region 2 has a significantly denser morphology. (c) GDOES depth profiles of each of these regions reveal that region 2 has significantly more sodium on the surface and decreased carbon and nitrogen throughout the depth of the absorber.

Figure 3.9 characterized a film of a sample that was selenized in a graphite box previously used for lithium doping experiments. Comparison of the cross sections in **Figure 3.9da,b** show that region 1 has much finer grains than the dense morphology in region 2, while GDOES of each of these regions reveal that region 2 has 20x more sodium on the surface of the film and significantly less carbon and nitrogen in the absorber as shown in **Figure 3.9c**. These results suggest that (1) volatile sodium containing species (i.e., Na_2Se_x) deposit on the walls of the graphite box during selenization, and (2) these species facilitate the transport of C and N out of CZTSSe films fabricated from the CZTS/DMSO molecular ink. Despite the wide number of studies which discuss how alkali elements can affect the optoelectronic properties of chalcogenides, this is the first data that connects alkali species to the transport of impurities out

of solution-processed films. These results also explain the dense 'Li free' samples in Xin et al.'s report on Li-doped CZTSSe, since a single graphite box was used for all selenizations.[17]

3.9 The Potential of Sulfurization to Remove Impurities

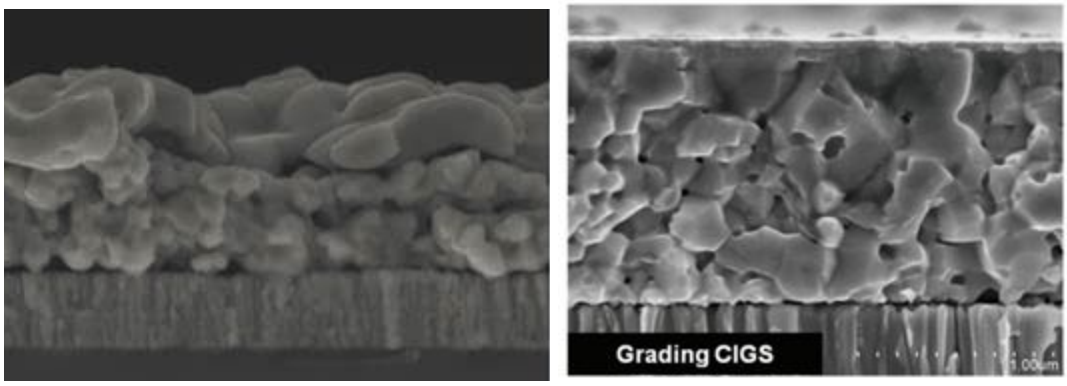

Figure 3.10 SEM cross sections of CIGS absorbers from the DMSO-TU process (left) (from the same dataset that lead to 14.7% devices),[65] and from hydrazine (right) (from the same dataset as the world record PCE for solution processed PCE: 17.3).[15] The multi-layer morphology for the DMSO-TU suggests that C and N have become trapped in the film.

The experiments examining the annealing profile of CZTS from the DMSO-TU molecular ink showed that there may be two optima for annealing in order to avoid the trapping of C- and N-containing TU decomposition products. High temperature annealing (~500 °C) was shown to remove C and N, but the Raman data in **Figure 3.7e** show that polymerized amorphous carbon nitride (a-C:H:N) becomes incorporated into absorbers even for the hottest/longest thermal profile examined. The other annealing profile which led to high efficiency devices was a low anneal temperature (~300 °C), which avoids the polymerization of a-C:H:N and allows C and N to volatilize during selenization. The record CIS device (13.0%) and CIGS device (14.7%) made from the DMSO-TU process have all used a low temperature annealing profile.[65] This leads to dense films in the case of CIS as presented in in Uhl et al.,[65] but leads to a multilayer morphology in the case of CIGS as shown in **Figure 3.10a**. By contrast, the hydrazine-based

record for solution-processed CIGS exhibits a dense morphology and leads to a much higher device PCE (17.3%). Preliminary experiments showed that CIGS, deposited from either the DMSO-TU or DMF-TU inks, consistently exhibited fine-grained layers for many different annealing profiles. This is not true for CIS deposited from same inks. This suggests that gallium inhibits transport of carbon and nitrogen impurities out of the film. Therefore, it was desirable to use an alternative method to remove C and N from the absorber before selenization.

Wu et al. found that CZTS absorbers from a molecular ink process based on methoxy-ethanol and thiourea (MEOH-TU) showed substantial improvement in multilayer morphologies and device performance by employing a sulfurization before selenizing CZTSSe films.[100] This led to a device efficiency of 10.1% and recently, Wu et al. reported a follow up paper with an 11.1 PCE device.[101] The MEOH-TU was first presented in 2015 and has been widely adopted; however, apart from these studies, efficiencies have been limited to <9%.[59] The morphological and device PCE improvements presented by Wu et al. lack any discussion of impurity transport; however, I hypothesized that these improvements were due to C and N transport out of the film during sulfurization. Therefore, an experiment was performed with DMF-CIGS molecular ink to determine (1) if sulfurization affects impurity transport out of the absorber, and (2) if this leads to improved morphologies.

CIGS-DMF molecular inks were used to deposit metal sulfide precursor films, which were treated to various sulfurization and selenization profiles. No optimization for the time and temperature of the sulfurization was performed (sulfurizations were performed for 20 mins at 540 °C, identical to the selenization conditions). Nevertheless, sulfurized films showed drastic differences in impurity content and morphology as shown in **Figure 3.11**.

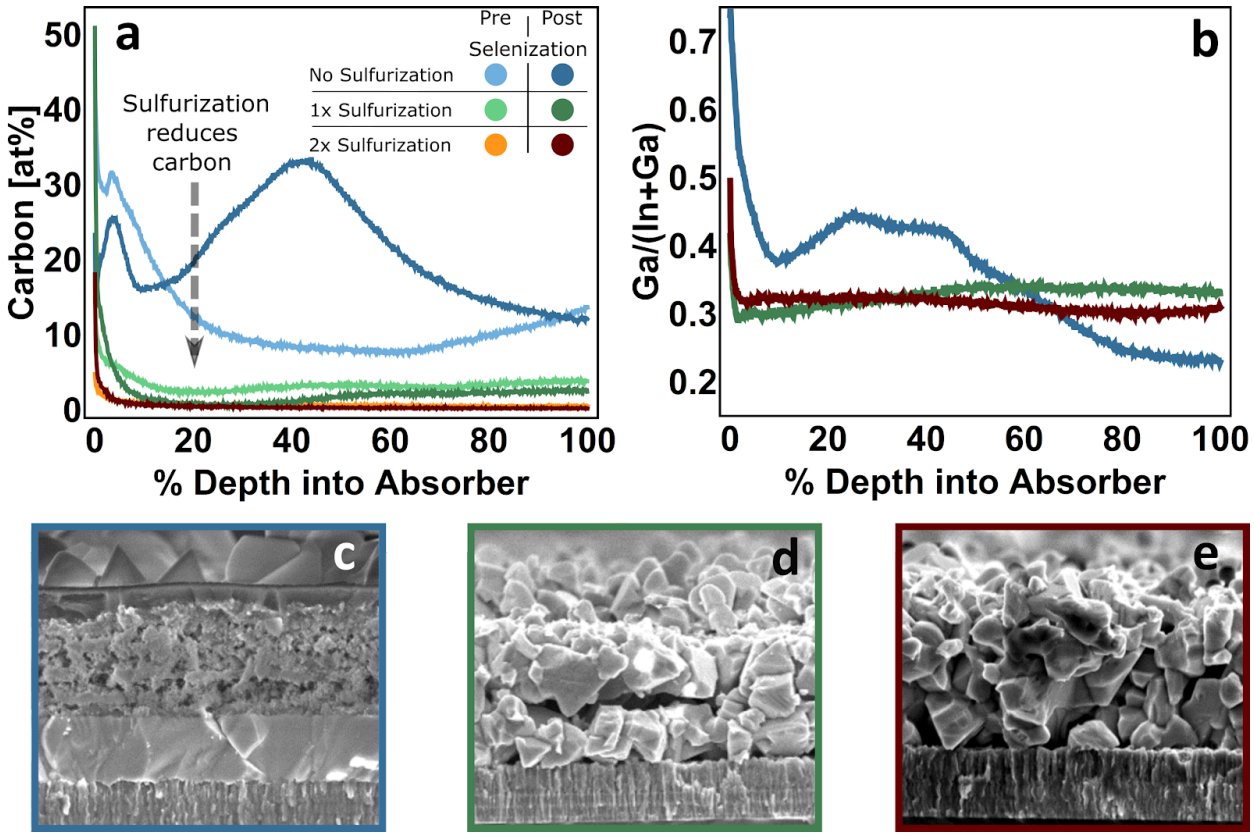

Figure 3.11 GDOES depth profiles for (a) carbon and (b) Ga/(Ga+In) of CIGS sulfide and selenized films which were sulfurized to various degrees before selenzation. SEM cross sections of selenized CIGS films (c) without sulfurization, (d) with one sulfurization, and (e) with 2 sulfurizations show that improvements in morphology correlate with the removal of impurities.

Films exhibited substantially decreased carbon content after one sulfurization, and carbon content was below the signal to noise for GDOES after two selenizations. The GDOES elemental depth profiles of the baseline selenized film reveal that the fine-grained layers are enrichiched in gallium and carbon. This correlation is likely related to why CIGS films have much worse morphology than their CIS counterparts. The co-localization of Ga, C, and N suggest that gallium containing species may react and bind C and N containing thiourea decomposition products during selenization. The removal of the impurities with sulfurization leads to progressively better morphologies as shown by **Figure 3.11c-e**. The 2x sulfurized CIGSe film

shown in **Figure 3.11e** has the lowest impurity levels of an CIGS film measured with GDOES and has similar morphology to the hydrazine-based device presented in **Figure 3.10b**.

3.10 Conclusion

In this chapter, we have shown how the annealing profile of the DMSO molecular ink critically effects the material properties and depth-dependent impurity profiles of both precursor and selenized films. For precursor films, annealing profiles with increasing thermal exposure lead to (1) metal sulfide with more crystallinity and fewer binary phases (with the exception of SnS for the highest thermal exposure), (2) increasing transport of Cl out of the film, (3) increasing transport of C & N out of the film only if annealing temperature >400 °C are used, and (4) a higher degree of polymerization of non-volatilized C and N. This leads to selenized films which evolve C and N at 300 °C during selenization while films annealed at 400 °C trap C and N in a fine-grained layer, which was shown to consist of a hydrogenated amorphous carbon nitride (a-C:H:N) network. Selenized films from 500 °C conditions had significantly reduced C and N in the bottom layers which led to an improvement in device performance over the 300 °C and 400 °C conditions. The reason for the device improvement from Li-doping experiments was shown to be due to the expulsion of Na from the SLG into the precursor film during annealing. High Na content in the film likly creates Na_2Se_x during selenization, which was shown to substantially reduce the C and N impurities in films after selenization. Finally, the potential of sulfurization as a method to remove impurities from these molecular inks was demonstrated.

Chapter 4: Complexation Chemistry in N,N-Dimethylformamide-Based Molecular Inks for Chalcogenide Semiconductors and Photovoltaic Devices

4.1 Introduction

While there are numerous benefits of the DMSO-based molecular ink chemistry for chalcogenide semiconductor thin films, some important metal species have low solubility or low stability in DMSO, including Cu(I), Ag(I), In(III), Ge(II), and Ge(IV) species.[65,66] Cu(I) species can be effectively solubilized to form stable inks with DMSO by using thiourea as a ligand.[62,63] However, the same DMSO-TU-based stabilization does not significantly increase solubility of Ag(I) and In(III) compounds, and it forms a gel with Ge(II) and Ge(IV) compounds.[66] Ag(I) and Ge(IV) are of interest because alloys of the species with CZTS have been increasingly studied in an attempt to reduce cation site disorder in the kesterite lattice.[102–107] To overcome these issues with stability and solubility, we investigated numerous other solvents and ligands and found that N,N-Dimethylformamide (DMF) stabilized these species and allowed for the creation of high concentration stable molecular inks.[66] In addition to the increased stability and concentration (relative to DMSO-based inks), the new DMF-based ink chemistry was used to add all the metal species necessary for CZTS and $Cu_2Zn(Sn,Ge)(S,Se)_4$ (CZTGS) in their desired oxidation state, Cu(I), Zn(II), Sn(IV), and Ge(IV), without needing to undergo redox reactions.[63] These DMF-based CZTGS inks were stable and lead to devices with PCE of 11.0% with record high open-circuit voltage for its bandgap.[66] With a V_{oc} of 583 mV and a band gap of 1.2 eV, the device achieved 63% of the Shockley–Queisser limit V_{oc}, which is the highest reported for any kesterite absorber material. A subsequent report used a 50% DMF and 50% IPA based ink wherein it reported a highly-concentrated, stable ink which was employed to deposit 1 μm thick

CIS films in four layers of spin-coated ink (compared to 13 layers from a DMSO-TU ink) and PV devices resulting in a PCE of 3.4%.[67] However, the high concentration of IPA may have led to the formation of M-O-R and M-O-M linkages. In the current report, we show that CIS thin films and PV devices with 13.4% PCE may be fabricated using only DMF as a solvent.

The combination of DMF and TU contains four different character Lewis base sites (the O and N in DMF along with the S and N in TU), which appear to be unique in their ability to stabilize a wide number of (Lewis acidic) metal chlorides (particularly high valence In(III), Ga(III), Sn(IV), and Ge(IV)) at high concentrations. However, there is little fundamental understanding of the mechanisms through which these high concentrations are achieved. In this work, we examine the complexes formed in DMF solutions of metal chlorides (Cu, Ag, Zn, In, Ga, Sn, Ge), along with chalcogen sources (thiourea, selenium tetrachloride, elemental selenium, and polyselenide chloride species).

4.2 Chloride and Thiourea Complexes in DMF Solutions

Starting Species	Solubility in DMF	Effect of Free Cl^- on Solubility	Donates Free Cl^- to Stabilize CuCl	Effect of Thiourea on Solubility
CuCl	<0.01 M	Increased to ~0.35 M	No	Increased to 0.25M
AgCl	<0.01 M	None	No	Increased to 2.0 M
$ZnCl_2$	1.5 M	Increased to 1.75M	Slightly	Increased to 2.0 M
$InCl_3$	0.3 M	Increased to 0.65 M	Yes	Increased to 0.65 M
$GaCl_3$	>3.0 M	-	Yes	-
$SnCl_4$	0.4 M	Increased to 0.6M	Yes	Increased to 0.5M
$GeCl_4$	0.04 M	Decreased	Yes	None
$SeCl_4$	1.1 M	Decreased	Yes	Decreased
Se	<0.01 M	Increased to 1.5 M†	No	None

Table 4.1 A summary of the solubilities of species in DMF with and without excess chloride and thiourea. $^{\dagger}SeCl_4$ was used as the free Cl^- source

Dimethylformamide (DMF) is a Lewis-basic aprotic solvent which is known to solvate bivalent and trivalent cations, but is generally unable to solvate monovalent cations.[108] **Table 4.1**

summarizes the solubilities of the metal chlorides examined here and highlights the drastic differences in the concentrations of achievable stable solutions. CuCl has exceptionally low solubility in DMF alone and disproportionates according to 2 $Cu^{+} \rightleftharpoons Cu^{0} + Cu^{2+}$. This disproportionation reaction is well-known, and equilibrium constants have been measured for a number of solvents, with water, DMF, DMSO, and acetonitrile being ~10^{7}, ~10^{4}, ~10^{0}, and ~10^{-21} respectively.[109] However, this report also showed that ligands which preferentially bind Cu^{2+} can increase these equilibrium constants (i.e., increase disproportionation) in DMF and other solvents. Analogously, species that stabilize the Cu^{+} oxidation state are expected to decrease the disproportionation equilibrium constant (i.e., decrease disproportionation).

Figure 4.1a shows that the addition of tetraethyl ammonium chloride (TEAC) reverses the CuCl disproportionation reaction in DMF. For ratios of TEAC/CuCl>1, all Cu^{0} dissolves and the solution turns clear. Since TEAC is known to almost completely dissociate TEA+ and Cl- in aprotic solvents,[110] this stoichiometry suggests that CuCl and Cl^{-} react to form some combination of $CuCl_2^{-}$, $Cu_2Cl_4^{2-}$, or $Cu_3Cl_6^{3-}$, which are soluble in DMF and shift the disproportionation reaction to the left. Indeed, Zhao et al. have shown that all three of these species exist in aqueous solutions of CuCl and NaCl and that the polynuclear species become more prominent for higher CuCl concentrations.[111] Higher concentration solutions of CuCl for TEAC/CuCl=1 appear yellow in color (but still stable). This is an indication of higher concentrations of polynuclear ($Cu_2Cl_4^{2-}$, or $Cu_3Cl_6^{3-}$) copper complexes.

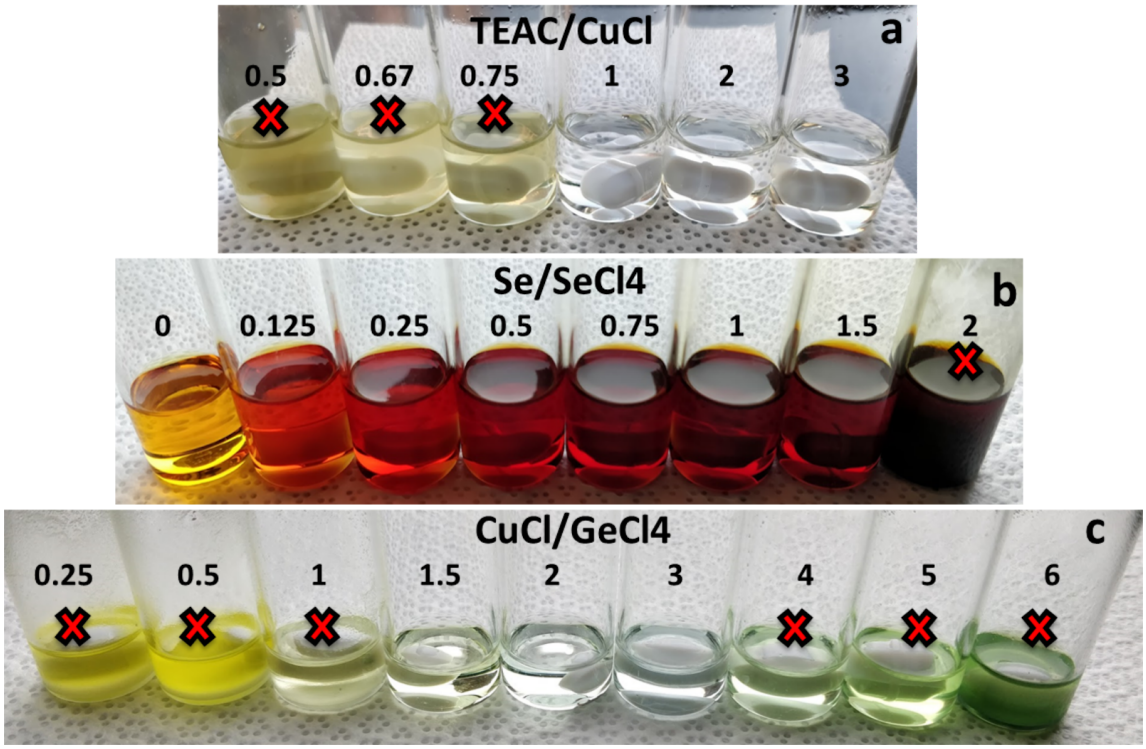

Figure 4.1 Solubility studies with various chloride species in DMF. Red X indicates all solids did not dissolve. (a) CuCl (constant 0.025 M) mixed with tetraethylammonium chloride (TEAC) in DMF. All solids (Cu^0) dissolve at 1 TEAC/CuCl and higher suggesting that $CuCl_2^-$ is stabilized in solution. (b) $SeCl_4$ (constant 0.5 M) mixed with Se metal in DMF. Se is solvated up to 1.5 Se/$SeCl_4$ via equilibrium reactions with $SeCl_2$ and Se_2Cl_2. (c) $GeCl_4$ (constant 0.25 M) mixed in with CuCl in DMF. Individually, $GeCl_4$ and CuCl have low solubility in DMF, but chloride transfer from germanium to copper drastically increases the solubility of both species.

A number of the other metal chloride species examined here can participate in redox reactions and reactions with Cl^- to form various complexes in solution. **Figure 4.1b** exemplifies the ability of $SeCl_4$ to react with elemental Se, which allows for dissolution of Se into DMF up to 1.25 M. Starting with a concentration of 0.5 M $SeCl_4$, ~0.75 M Se can be solvated into solution. Lamoureux et al. examined equilibria between $SeCl_4$ and Se in a number of aprotic solvents and inferred a number of equilibria including $SeCl_4 + Se \leftrightarrow 2SeCl_2$, $SeCl_4 + 3Se \leftrightarrow 2Se_2Cl_2$ and others which form polyselenide species up to Se_4Cl_2.[112] Given that greater than 1 Se/$SeCl_4$ is

soluble, this must mean that some polyselenide species are present. This is confirmed by the color of the solution as Se_2Cl_2, which is reddish-brown.

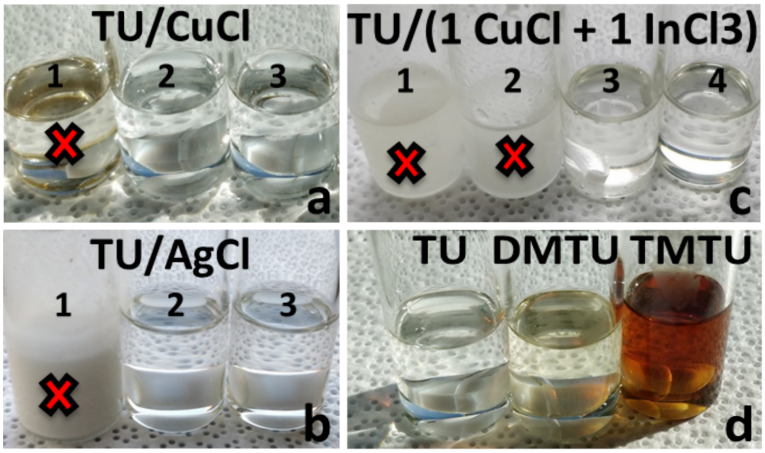

Figure 4.2 Solubility studies with various species in DMF. Red X indicates all solids did not dissolve. (a) CuCl (constant 0.025 M) mixed with thiourea (TU) in DMF. All solids (Cu^0) dissolve at 1:2 TU suggesting that CuCl is stabilized via a coordination complex with 2 TU. (b) AgCl (constant 0.5 M) mixed with thiourea (TU) in DMF. All solids dissolve at 1:2 TU suggesting that AgCl is stabilized via a coordination complex with 2 TU. (c) Solutions of CuCl, $InCl_3$, and TU in DMF where [CuCl+$InCl_3$]= 1.5 M. A thiourea/metal ratio>3 is required to stabilize CIS inks. (d) Solutions of CuCl, $ZnCl_2$, and $SnCl_4$ with thiourea (TU), dimethyl-thiourea (DMTU), and tetramethyl-thiourea (TMTU). In contrast to the the CIS inks, TU/metal=1 is stable for CZTS inks.

$GeCl_4$ has complex interactions with CuCl in DMF solutions, where both chloride-transfer and electron-transfer (redox reactions) can occur to differing degrees depending on the relative concentration of both species. DMF complexes with both $GeCl_4$[113] and $GeCl_2$[114] have been reported; however, $GeCl_4$ alone has a low solubility in DMF (~0.04 M). **Figure 4.1c** shows how chloride transfer between $GeCl_4$ and CuCl can drastically increase the low solubility of both species. Similar to Sn this may be due to a redox equilibrium reaction $2CuCl_2 + GeCl_2 \leftrightarrow 2CuCl + GeCl_4$, but for ≤2 CuCl/$GeCl_4$ does not appear green in color, suggesting a cationic Ge(IV) species is highly soluble in DMF (perhaps $GeCl_2^{2+}$). For ≥2 CuCl/$GeCl_4$ solutions appear green, suggesting that copper has been oxidized to Cu(II).

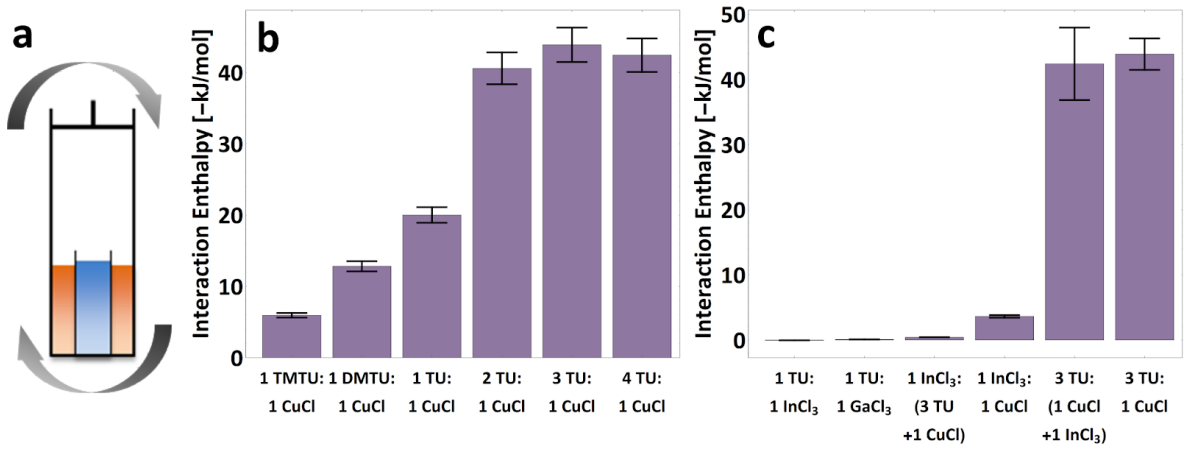

Figure 4.3 (a) Schematic of mixing calorimetry vessel before mixing. One or more species was dissolved/suspended in DMF and deposited in the annulus (shown in orange), while a second species was dissolved/suspended in DMF and deposited in the cup (shown in blue). The heat was measured as the sealed vessel was rotated and kept at constant temperature. Further details of solution calorimetry results and procedure can be found in the SI. (b) Measured enthalpy of complexation for thiourea and methylated thiourea with CuCl. The saturation in interaction enthalpy above 2 TU/CuCl suggest that 2 TU complex with TU in solution. (c) Measured enthalpy of complexation for various metal chloride and TU mixtures.

Thiourea (TU) is a Lewis base that is known to complex with a number of (Lewis acidic) metal chlorides. A number of these complexes have been isolated: $CuCl(TU)_3$,[115] $Cu_2Cl_2(TU)_4$,[116] $AgCl(TU)_2$,[117] $ZnCl_2(TU)_2$,[84] $InCl_3(TU)_3$,[118] $SnCl_2(TU)$,[84] and $SeCl_4(TU)_2$.[119] However, the metal chloride/TU complexes that exist in DMF solutions may differ from these isolated complexes, because DMF is also a Lewis base that can compete with TU in solution. **Figure 4.2a** shows that CuCl is stabilized in DMF when a stoichiometry of at least 2 TU/CuCl is present in solution. This suggests that $CuCl(TU)_2(DMF)_x$ complex forms in solution, and this is further supported by the calorimetry data shown in **Figure 4.3**. To determine the enthalpy of complex formation, individual precursors were dissolved or suspended in DMF and then mixed inside an isothermal calorimeter according to the schematic in **Figure 4.3a**. The 1 CuCl: 1 TU and 1 CuCl: 2 TU complexation enthalpies were measured to be -20.03± 1.1 kJ/mol and -42.3± 2.33 kJ/mol

respectively, while additional TU showed no increase in the exotherm as shown in **Figure 4.3b**. As with Cl^-, TU preferentally stabilizes CuCl in solution and reverses the disproportionation in DMF reaction discussed above. Similarly to CuCl, the solubility of AgCl is also drastically increased in DMF when 2 TU/AgCl is present as shown in **Figure 4.3b**. Thiourea also increases the solubility of a number of these other metal chlorides as shown in **Table 4.1**.

4.3 Raman Spectroscopy of Chloride and Thiourea Complexes in DMF

In order to clarify various coordination mechanisms between CuCl, $InCl_3$, and TU in DMF, Raman spectroscopy was measured on a number of solutions as shown in **Figure 4.4**. In this range, the major active Raman modes for DMF can be attributed to various C−N−C′ modes at 318, 356, and 405 cm^{-1}, the O=C−N bend at 660 cm^{-1}, the N−C′ stretch at 866 cm^{-1}, various C′−H deformation modes at 1093 and 1440 cm^{-1}, the C−H bend at 1408 cm^{-1}, and the O=C stretch at 1662 cm^{-1},[120] where C and C′ respectively indicate the aldehydic carbon and carbons associated with the methyl groups. The major active Raman modes for TU are the N−C−N bend at 486 cm^{-1}, the C=S stretch at 744 cm^{-1}, and the C−N stretch at 1085 cm^{-1}.[121] $InCl_3$ is known to have overlapping Raman modes at 289 and 300 cm^{-1} which are both related to stretching of InCl.[122] Cu−Cl has major Raman modes at 206 and 463 cm^{-1},[123] which are respectively related to Cl−Cu−Cl bending and Cu−Cl stretching modes.

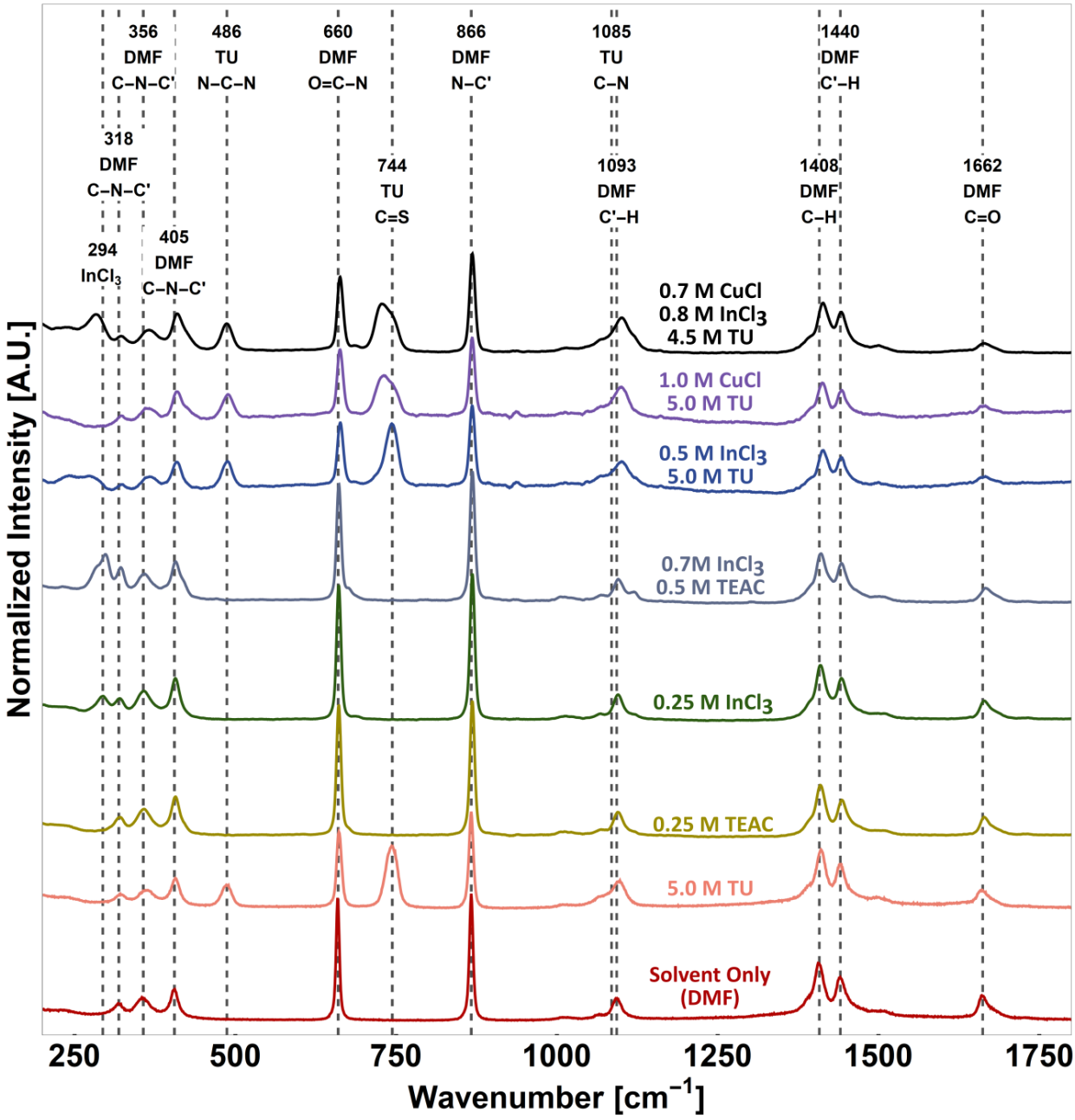

Figure 4.4 Raman spectra for various combinations of CuCl, InCl3, thiourea (TU), and tetraethylammonium chloride (TEAC) dissolved in DMF. The excitation wavelength was 785 nm. Major Raman modes for each of the species are labeled, and their description is given in the text. For the DMF labels, C refers to the aldehydic carbon, while C′ refers to the carbons associated with the methyl groups.

A detailed analysis of the Raman peak shifts for a number of DMF solutions is presented below and leads to the following conclusions: (1) CuCl and TU complex in solution via the interaction between Cu and S. (2) $InCl_3$ does not directly form a complex with TU in solution; instead, TU scavenges free chloride in solution, which in turn increases the concentration of more highly soluble cationic indium species (e.g., $InCl_2^+$). (3) Free chloride (via TEAC) increases the concentration of the more highly soluble $InCl_4^-$. (4) Solutions containing CuCl, $InCl_3$, and TU show characteristics of both $InCl_4^-$ and cationic indium species, which explains the drastic increase in $InCl_3$ solubility in complete CIS inks. (5) For solutions containing CuCl, $InCl_3$, and TU, excess TU (ratios of 6 TU:1 CuCl:1 $InCl_3$ or higher) is required to prevent the precipitation of coordinated $[Cu(TU)_2]^+$ and $[InCl_4]^-$ complexes.

Conclusion (1). CuCl/TU solutions exhibit a pronounced broadening and shift of the SC peak at 743 cm^{-1}, which is a clear indication that the CuCl and TU complex via the Lewis acid−base interaction between Cu and S. These Raman data along with the above calorimetry data suggest that Cu(I) is stabilized in DMF by the formation of $CuCl(TU)_2(DMF)_x$ or $[Cu(TU)_2(DMF)_x]^+$. Given that the Cu−Cl stretching Raman mode 463 cm^{-1} is absent in these solutions, we suspect that the cationic complex forms, which also liberates Cl^- into the solution.

Conclusion (2). In contrast to CuCl/TU solutions, the Raman spectra of $InCl_3$/TU solutions show no evidence of Lewis acid−base interaction between In and S based on the absence of a peak shift at 744 cm^{-1}. This is surprising because the addition of TU to DMF solutions of $InCl_3$ substantially increases the solubility of In as shown in Table 1. We suspect that this increase in indium solubility is related to an increase in cationic indium species due to TU complexation with free chloride in solution. In solution, TU is known to tautomerize to its thione form and

complex with chloride to form thiourea hydrochloride (TU-HCl).[124] This explanation is supported by the peak shift at 1085 cm^{-1} to higher wavenumbers for $InCl_3$/ TU solutions when compared to TU solutions, because a similar peak shift has been shown in Raman spectra of TU-HCl when compared to TU.[125] The formation of TU-HCl complexes reduces free Cl^- in solution which directly affects the equilibria of In species. As discussed above, five indium chloride complexes ($[InCl_n]_{(3-n)}$, n =0−4) exist in equilibrium in DMF, and a reduction of the concentration of Cl^- in solution leads to higher concentration of cationic species (e.g. $[InCl_2]^+$, $[InCl]^{2+}$).[126] A corresponding peak shift and broadening of the In−Cl Raman modes to lower wavenumber (~250−290 cm^{-1}) are observed for $InCl_3$/TU solutions, which are attributed to an increased concentration of cationic indium species.

Conclusion (3). As shown in **Table 4.1**, increasing the concentration of Cl^- (via TEAC) increases the solubility of indium chloride in DMF as well. As before, this change in free chloride in solution affects the equilibria between indium chloride species and increases the concentration $InCl_4^-$ in solution. A corresponding shoulder appears on the In−Cl Raman modes toward lower wavenumber for $InCl_3$/TU solutions, which is attributed to an increased concentration of $InCl_4^-$.

Conclusion (4). We have previously shown that solutions of CuCl, $InCl_3$, and TU can stabilize concentrations of $InCl_3$ up to 1.8 M,[3] which is much higher than solutions with TEAC or TU alone. Interestingly, the In−Cl stretching modes in these solutions exhibit characteristics of both $InCl_3$/TEAC and $InCl_3$/TU solutions (a peak at 285 cm^{-1}, and broad peaks at 250 and 270 cm^{-1}, respectively), suggesting that both $[InCl_4]^-$ and cationic $[InCl_n]_{(3-n)}^+$ species are stabilized in

complete CIS inks. Given that both of the charged indium species have a higher solubility than $InCl_3$ alone, this explains the much higher achievable concentration of In.

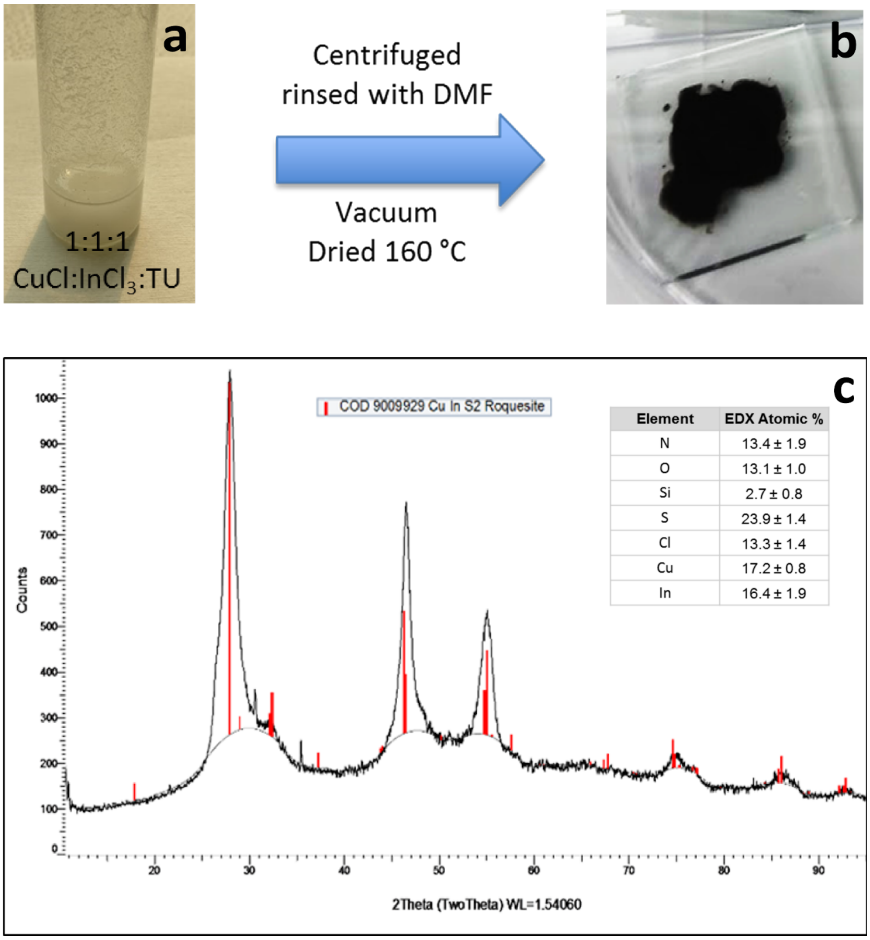

Figure 4.5 (a) A 1:1:1 mixture of CuCl: $InCl_3$: TU forms a white precipitate. (b) The mixture was centrifuged, rinsed with DMF, deposited onto a glass slide, and dried in a vacuum oven at 160 °C for 8 hours. (c) XRD shows peaks characteristic of $CuInS_2$ and EDX shows evidence of Cu, In, S, and Cl. These data suggest that the precipitate contains CuCl, $InCl_3$ and TU.

Conclusion (5). When small amounts of TU are added to solutions of CuCl and $InCl_3$ in DMF, a white precipitate forms and at least 6 TU:1 CuCl:1 $InCl_3$ is required to stabilize inks, as shown in **Figure 4.2b**. The precipitate from a 2 TU:1 CuCl:1 $InCl_3$ mixture was isolated via centrifugation, rinsed, and dried at 160 °C as shown in **Figure 4.5**b. EDX and XRD of the dried

precipitate reveals that it contains Cu, In, Cl, and TU as shown in **Figure 4.5**c. Given these data and the above discussion of stabilization mechanisms for CuCl and $InCl_3$, we suspect that, when TU is in excess less than 6 TU:1 CuCl:1 $InCl_3$ in solution, a cationic $[Cu(TU)_2]^+$ complex and anionic $[InCl_4]^-$ crystallize and precipitate. When additional TU is added, it reduces the concentration of InCl4− by coordinating with Cl− and increasing the concentration of cationic indium complexes. A detailed reaction scheme for this proposed stabilization mechanism is presented in **Scheme 4.1** below.

$$InCl_3 + CuCl \rightarrow InCl_2^+ + CuCl_2^- \ (Stable)$$

$$InCl_2^+ + CuCl_2^- + 2\,TU \rightarrow InCl_4^- + Cu(TU_2)^+ \ (Precipitation)$$

$$InCl_4^- + Cu(TU_2)^+ + 4\,TU \rightarrow InCl_2^+ + Cu(TU_2)^+ + 2\,TU^- + 2\,TU \cdot HCl \ (Stable)$$

Scheme 4.1 Proposed mechanism to explain the behavior of CuCl, $InCl_3$, and TU solutions. As shown in SI figure 1 solutions of 1:1 CuCl and $InCl_3$ are stable, unstable for ratios of 1:1:2 CuCl:$InCl_3$:TU and stable for ratios of 1:1:6 CuCl:InCl3:TU as shown in Figure 2c of the main text. The above stabilization mechanism is proposed based on these data and the Raman data.

4.4 Methylated Thiourea Complexes

			$CuInS_2$				
sulfur source	metal loss	Cu (at%)	Ga (at.%)	In (at.%)	Cu/(In+Ga)	Ga/(In+Ga)	Cu/In
TU	none	9.54	3.33	8.22	0.83	0.29	1.16
DMTU	Ga (some In)	14.57	0.11	10.9	1.32	0.01	1.34
TMTU	Ga and In	7.1	0	0.08	88.75	0.00	88.75
			$Cu_2\ ZnSnS_4$				
sulfur source	metal loss	Cu (at%)	Zn (at.%)	Sn (at.%)	Cu/(Zn+Sn)	Zn/Sn	Cu/Sn
TU	some Sn	10.78	8.05	4.09	0.89	1.97	2.64
DMTU	Sn	17.44	7.9	2.58	1.66	3.06	6.76
TMTU	Sn and Zn	16.85	0	0	N/A	N/A	N/A

Table 4.2 EDX Summary of Thin Films from CIS and CZTS inks with sulfur sourced from thiourea (TU), 1,3-dimethylthiourea (DMTU), and tetramethylthiourea

In **Chapter 3** we demonstrated that decomposition products of TU can polymerize to form amorphous carbon nitride by deprotonation of the N−H groups with N−C bond formation.

Therefore, methylated thioureas (i.e., where the amine groups are methylated) were hypothesized to avoid this polymerization and allow C- and N-containing decomposition products to leave cleanly upon annealing. We examined 1,3-dimethylthiourea (DMTU) and tetramethylthiourea (TMTU) as potential ligands in molecular inks. As with TU, CuCl/ $InCl_3$/$GaCl_3$ inks (CIGS inks) require at least three R-TU per metal for a stable ink while CuCl/ZnCl2/$SnCl_4$ inks (CZTS inks) do not have this requirement. These CuCl/R-TU complexes appear darker in color with increasing methylation of the R-TU as shown by the CZTS inks in **Figure 4.2d**. Thin films from CIS and CZTS inks with TU, DMTU, and TMTU were fabricated by spin-coating and annealing at 500 °C. As shown by EDX in **Table 4.2** films from inks exhibited progressively more metal loss with increasing methylation of the TU. CIS films from TU inks exhibited no metal loss, while films from DMTU and TMTU exhibited increasing Ga and In loss. CZTS from TU inks exhibited some Sn loss due to a known CZTS decomposition reaction,[85] but films from DMTU and TMTU ink exhibited even greater Sn loss and even Zn loss in the case of TMTU. $GaCl_3$, $InCl_3$, $ZnCl_2$, and $SnCl_4$ are volatile at 500 °C, with vapor pressures of >760,[127] ~550,[127] ~10,[128] and >760 Torr,[129] respectively. These data highlight an important role of TU in aprotic molecular inks that was previously unreported: TU is a vital complexing agent which prevents metal chloride evaporation during annealing. TU complexes with Cu, Zn, In, and Sn chlorides all exhibit structures where Lewis-acidic metal interacts with the Lewis-basic sulfur on TU.[84,115,118] Some species may not complex with TU in solution, but these complexes form upon ink drying. For example, the S in TU does not directly complex with $InCl_3$ in solution as shown by the Raman data above. However, when DMF is driven off of solutions of $InCl_3$ and TU, Raman spectra of the dried film exhibits a substantial shift in the C = S peak at 743 cm−1 as shown in

Figure 4.6. This suggests $InCl_3$ complexes with TU via In−S interaction upon ink drying, which inhibits $InCl_3$ vaporization. Since CuCl has been shown to coordinate with TU via interaction with sulfur in DMF, mixing calorimetry experiments with CuCl and the R-TU compounds were used as a model system to assess the metal−sulfur interaction strength for these species. As shown by **Figure 4.3c**, TU, DMTU, and TMTU respectively exhibit enthalpies of complex formation of −20.03 ± 1.1, −12.83 ± 0.71, and −5.95 ± 0.33 kJ/mol with CuCl.

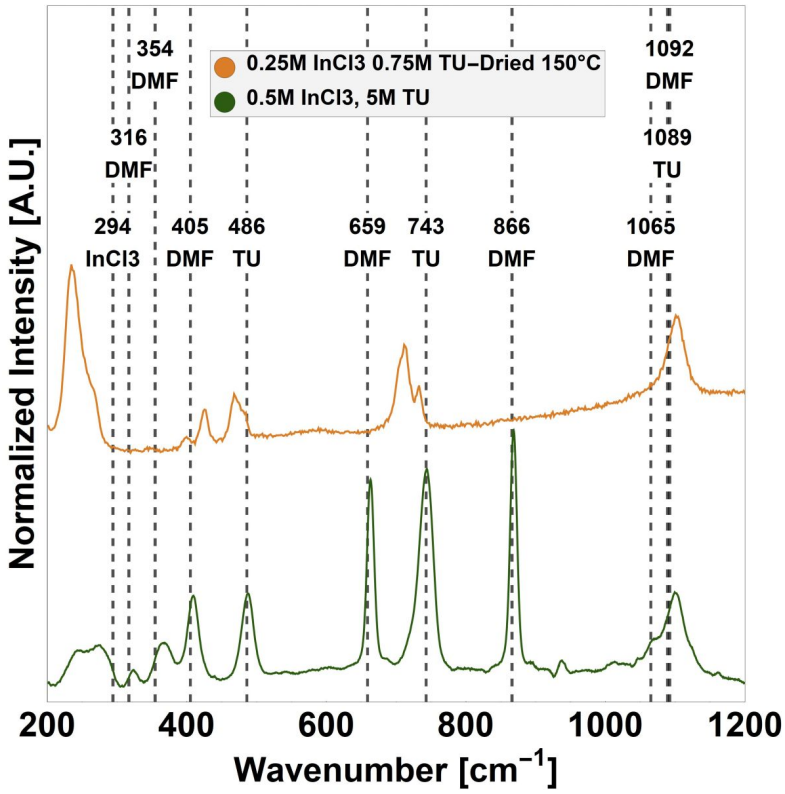

Figure 4.6: Raman spectroscopy of a solution of $InCl_3$ and TU in DMF (green trace), and of a film dried at 150 °C (orange trace). The absence of a shift in the S=C stretch at 743 cm^{-1} indicated that In does complex with the sulfur from TU in solution. Upon drying, however, Raman spectroscopy of the film reveals a clear shift in the the S=C stretch at 743 cm^{-1} indicating an In/TU complex has formed via the interaction in In and S.

The decreasing enthalpy of complex formation suggests decreasing interaction strength between the Lewis-acidic metal and the Lewis-basic sulfur, which is consistent with the trend in metal loss shown in **Table 4.2**.

4.4 Selenides from Solution Processing without Post-Selenization

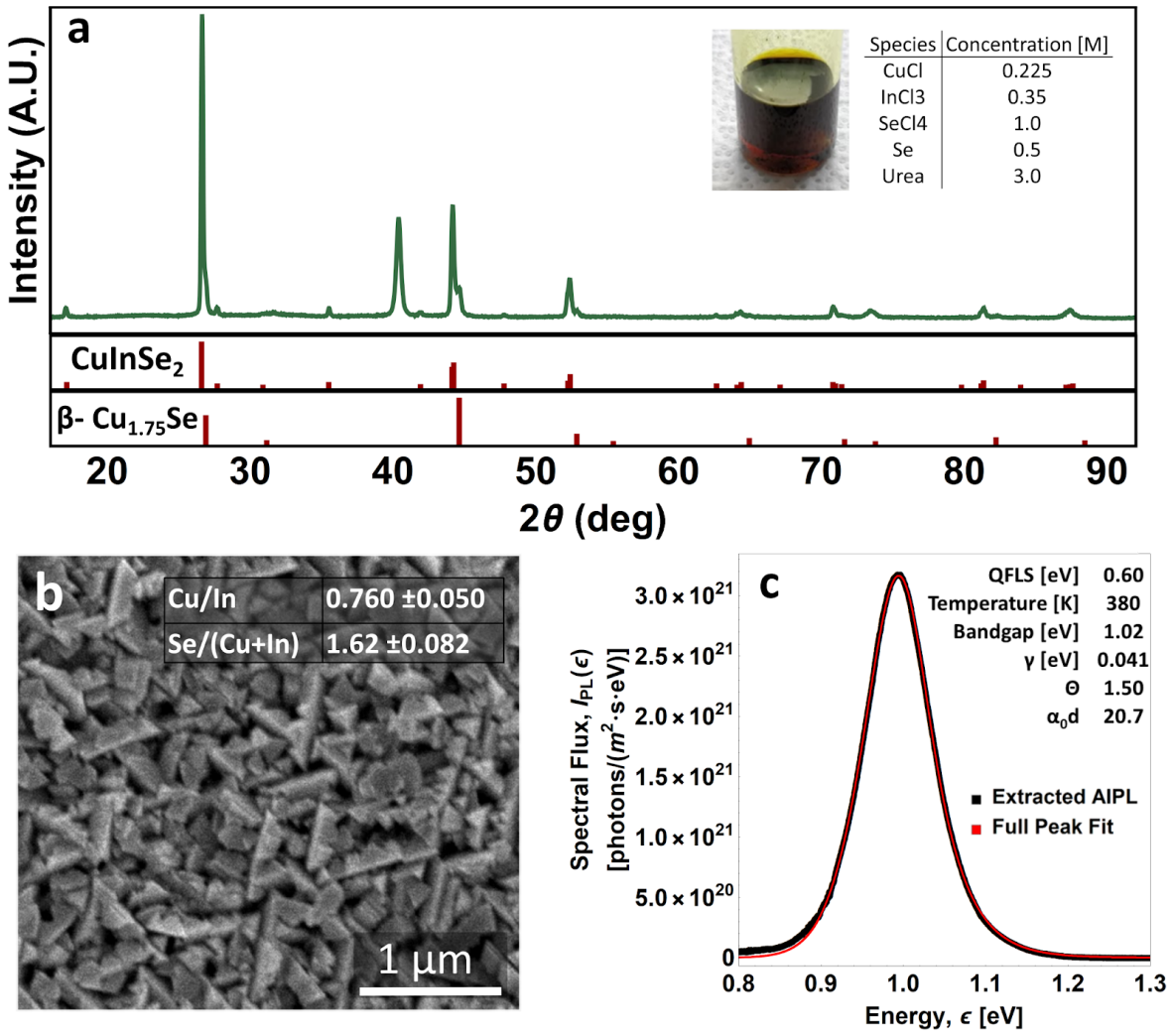

Figure 4.7 Characterization of a drop cast 100µL of an all-Cl CISe Ink (shown in the inset of a) annealed at 550°C for 20 min. (a) Powder XRD shows peaks characteristic of $CISe_2$ (PDF 00-040-1487) with some β-$Cu_{1.75}Se$ (PDF 04-014-3323) (b) SEM of the drop-cast film. The inset shows the average metal ratios measured with EDX for this film. (c) Absolute intensity confocal photoluminescence (PL) of drop-cast film (excitation intensity ~25000 suns). The PL Peak at 1.0 eV is typical of $CuInSe_2$ PL. Peak parameters were extracted with a full-peak fit method that was previously reported.[130]

The selenides of CZTS, CIS, and CIGS almost universally lead to higher PCE devices than the sulfide versions of these compounds. This has been attributed to favorable defect chemistry and better band alignment with CdS as illustrated by **Figure 2.2**. Further, the low bandgap of $CuInSe_2$ (CISe) (1.0 eV) make an excellent candidate for the bottom absorber in tandem PV cell applications.[3,65] Our discovery that free Cl^- stabilizes CuCl has allowed us to explore alternative molecular inks free from TU. We found that inks consisting of CuCl, $InCl_3$, $SeCl_4$, hereafter referred to as poly selenium chloride (PSC) CISe inks, are stable. Using $SeCl_4$ as a chalcogen source has some key advantages over TU: (1) the direct incorporation of Se into a molecular ink could eliminate the need for selenization, which is one of the biggest barriers to scale-up for chalcogenide-molecular-ink-based solar cells, and (2) $SeCl_4$ is carbon and nitrogen free (which was the cause of the fine-grained layers as discussed in Chapter 3). However, substituting $SeCl_4$ for TU also has some challenges: (1) the chalcogen is in the wrong oxidation state and must be reduced (from Se^{4+} to Se^{2-}), and (2) the absence of TU as a binding complex will allow metal chlorides to evaporate during annealing. Similar to the DMTU and TMTU inks in the previous section, there is significant $InCl_3$ and $SeCl_4$ loss when no binding agent is present in PSC CISe inks.

As a first attempt to overcome the two challenges with PSC CISe ink, urea was added to act as both a complexing and reducing agent. This ink was drop-cast onto a substrate, annealed under a Petri dish (550 °C for 20 min), and characterized with powder XRD, SEM, EDX and absolute intensity photoluminescence (AIPL). As shown in **Figure 4.7a** the XRD pattern from this film is an excellent match with $CuInSe_2$ and shows some evidence of $CuSe_{2-x}$. SEM of the film reveals heterogeneous morphology typical of drop-cast films; however, some regions

showed highly faceted morphology as shown in **Figure 4.7b**. Further, EDX revealed a roughly constant Cu/In and Se/(Cu+In) across the film. However, these values are Cu-poor and Se-poor when compared to pure CISe. EDX also revealed small amounts of Cl and N remaining in the film (4.1 ± 2.1 and 3.2 ± 2.0 atomic %, respectively). Given XRD only shows CISe and $CuSe_{2-x}$, this suggest that an indium-rich amorphous phase is present in the film. AIPL of the CISe film was measurable with a characteristic peak position at 1.00 eV as shown in **Figure 4.7c**. AIPL was somewhat heterogeneous across the substrate, and regions near corners and edges of the substrate showed the most intense PL, which may be due to increased Na flux near the edges of the substrate. The slight difference between the data and full-peak fit from 0.8 to 0.9 eV can be attributed to $CuSe_{2-x}$ plasmon resonance[131] and was found to be much more intense with other substrates with higher Cu/In ratios. These data represent the first example of photoluminescent, hydrazine-free solution processed CISe and may represent a novel ultra-low CAPEX pathway to deposit chalcogenide materials.

4.5 Photovoltaic Devices from DMF Molecular Inks

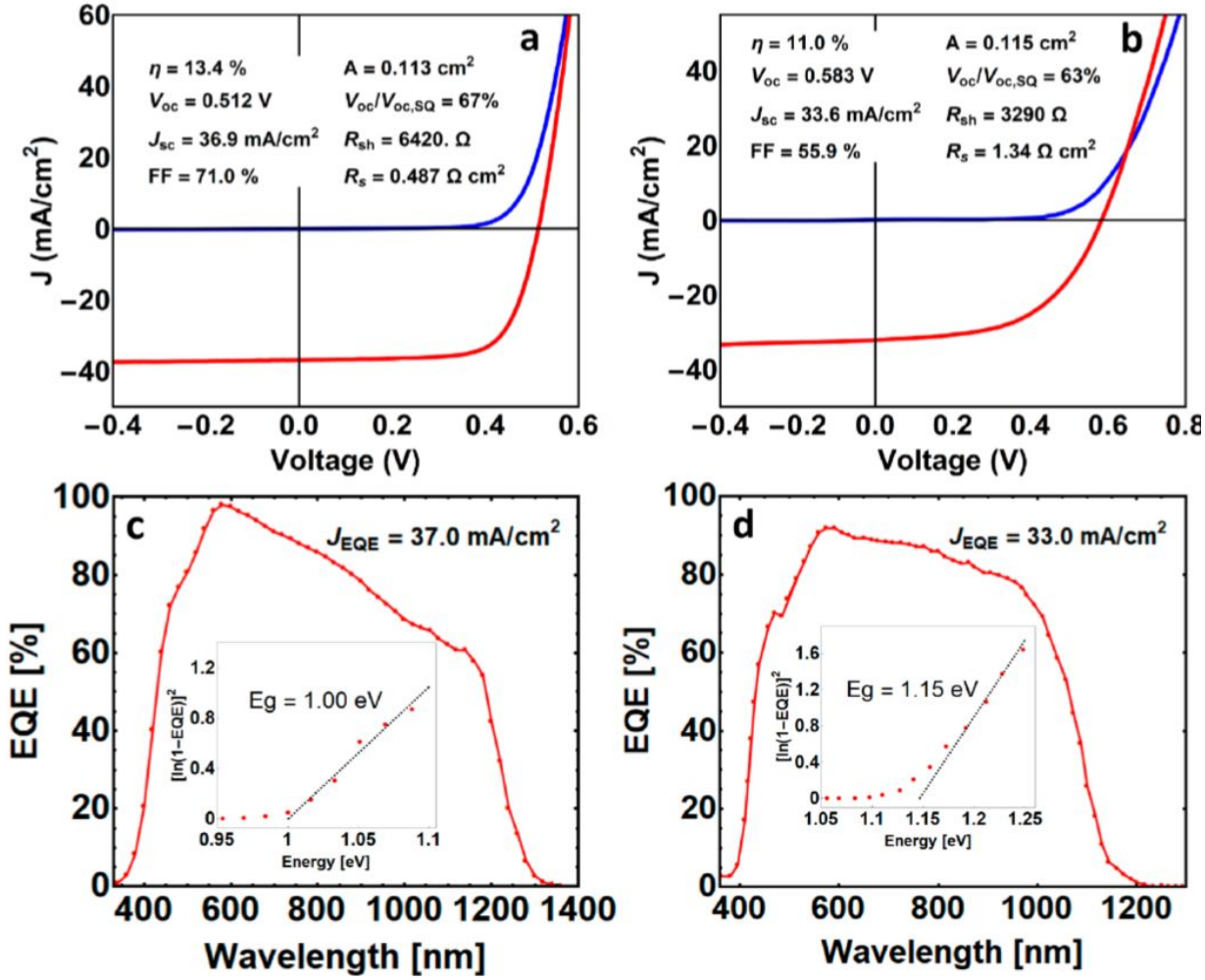

Figure 4.8 Device characterization of champion $CuIn(S,Se)_2$ (CISe) and Cu2Zn(Ge,Sn)(S,Se)4 (CZGTS) PV devices. Note that the CIS cell had a MgF_2 AR coating, while the CZGTS device did not. (a) JV of a CISe device. The active area efficiencies of 13.4% are among the highest reported PCEs for solution-processed CISSe. (b) JV of a CZTGS device. This is the highest reported $V_{oc}/V_{oc,SQ}$ for any kesterite device. (c,d) Integrated current from the EQE of the CIS (c) and CZTGS (d) devices show excellent matching to the Jsc values.

Utilizing the high solubility of CuCl and $InCl_3$ in the DMF-TU molecular ink allowed for the deposition of a ~2.2 μm CuInS2 precursor films in six spin-coating cycles (compared to 13 layers required for a 1.5 μm precursor film for the DMSO-TU CIS ink).[65] The champion devices from this absorber layer exhibited an exceptionally high PCE of 13.4% as shown in **Figure 4.8a**.

The Voc of 512 mV of this device is equivalent to 67% of the Schottky−Queisser (SQ) limit Voc based on the 1.00 eV bandgap extracted from EQE, which is among the highest value reported for any absorber with a 1.00 eV bandgap. The EQE data in **Figure 4.8c** reveal collection efficiencies <70% for carriers generated from photons with wavelengths of 1000−1200 nm. This suggests that Jsc may be improved by reducing the thickness of the absorber to improve carrier collection in this range. DMF-TU molecular inks with CuCl, $ZnCl_2$, and $GeCl_4$ were used to deposit $Cu_2Zn(Sn,Ge)(S,Se)_4$ absorbers via spraycoating, while avoiding gelling of the inks observed previously in DMSO-TU.[66] The champion device from this absorber layer had a Ge/(Ge+Sn) content of 30% and exhibited a relatively high PCE of 11.0%, as shown in **Figure 4.8b**. Note that this device has approximately the same germanium content and bandgap as the 12.3% PCE device reported by Kim et al.[102] Based on the 1.15 eV bandgap extracted from EQE, this device has a SQ limit V_{oc} (referred to as $V_{oc,SQ}$) of 915 mV. Therefore, the 583 mV V_{oc} of this device is equivalent to 63% of the $V_{oc,SQ}$ which is the highest $V_{oc}/V_{oc,SQ}$ reported for a kesterite-based device with any bandgap. A high series resistance and diode quality factor lead to a low fill factor of 55.9% for this device. This is typical for spray-coated films due to higher amounts of pinholes and higher surface roughness compared to spin coated films. If this device could be reproduced with identical performance but with fill factor improved to 70% (similar to values for other spin-coated high PCE kesterite devices),[57,102,132] this would lead to a 13.8% PCE which would represent a new world-record kesterite-based device.

4.6 Co-alloying CZTS with Silver and Germanium

As discussed in the introduction, CZTS devices have a low V_{oc} compared to their theoretical maximum (hereafter referred to as the V_{oc} deficit) . This is almost certainly due to substantial concentrations of defects, yet the most detrimental defect state(s) to device performance is the subject of much debate. The atomic radii for Cu(I), Zn(II) and Sn(IV) have similar atomic radii (respectively 74, 74, and 69 pm) in CZTS, which leads to small barriers for point substitution defects of these cations. DFT calculations predict that Cu_{Sn}, Sn_{Cu}, and Sn_{Zn} defects are near the middle of the bandgap (and are efficient SRH recombination centers).[53] This DFT analysis also predicted that a number of defect clusters (Zn_{Cu} + Cu_{Zn}) have very low formation energy, which has since been confirmed by direct observation.[133] Although this defect complex is predicted to have energy levels near the band edges, (Zn_{Cu} + Cu_{Zn}) clusters have been predicted to lead to bandgap and/or electrostatic potential fluctuations on the order of ~200 meV.[51] These fluctuations do reduce the maximum achievable V_{oc}, but calculations and experiments show that reducing the Cu/Zn disorder alone is not enough to explain the V_{oc} deficit for CZTS. [51,134,135] The culprit for the V_{oc} deficit is therefore most-likely related to a Sn-related midgap defect state in the bulk or at an interface which pins one (or both) of the quasi-Fermi levels under illumination. Many dopant and alloying species have been explored in an attempt to ameliorate the effects of these point defects, yet only a few stand out as showing improvement to device performance.[54,136] The most successful devices from these experiments utilized Li-doping, Ag-alloying and Ge-alloying and are highlighted in **Table 4.3**.

Material	Deposition Method	PCE [%]	Area [cm^2]	Eg [eV]	V_{oc} [mV]	Jsc [mA/cm^2]	FF [%]	Rs [Ω cm^2]	Rsh [Ω cm^2]
Radiative Limit		*33.5*	-	*1.13*	*886*	*43.4*	*87.1*	-	-
CZTSSe[7]	Hydrazine Ink	12.6	0.42	1.13	513	35.2	69.8	0.72	621
Li-CZTSe[73]	DMSO-TU Ink	12.3	0.25	1.11	496	35.2	65.8	-	-
Li-CZTSe[64]	DMSO-TU Ink	11.8	0.10	1.04	449	38.8	68.1	0.46	530
ACZTS[107]	Amine-thiol (MO) Ink	11.2	0.21	1.11*	464	36.2	66.5	1.56	542
CZGTS[102]	Coevaporation	12.3	0.52	1.11	527	32.2	72.7	0.36	1111
CZGTS[66]	DMF-TU Ink	11.0	0.12	1.15	**583**	33.6	55.9	1.34	378

Table 4.3 Comparison of high PCE kesterite all for a number of different compositions *This device employed an absorber bandgap gradient with ranged from 1.11 eV at each absorber interface to 1.06 eV in the center of the absorber.

The device parameters for the devices presented in **Table 4.3** are somewhat similar, yet the physical mechanisms for these high PCEs may have different origins. One commonality between all of these devices is the band gap close to 1.13 eV. This is likely related to the suppression of the interface recombination due to optimal conduction band offset at the CZTS/CdS interface ($\Delta E_c^{a,b}$) as illustrated by **Figure 2.2**. While $(Li_{1-x}Ag_x)_2ZnSnSe_4$ alloys have been synthesized via high temperature solid-state reactions,[137] the two devices presented showed little to no incorporation of Li CZTS.[64,73] For DMSO-TU inks, the effect of Li-doping is convoluted with the effect of impurity removal, improved morphology, and Na-doping (see **Chapter 3.6** and **Figure 3.5).**

Alloying Ag with CZTS has been shown to decrease PL peak full-width half max (FWHM) and PL red-shift from the band gap while increasing Ag incorporation, suggesting decreased

band-tailing.[106] This is due to the much larger atomic radius of silver (114 vs. 74 pm for Cu), which increases the formation energy of Zn_I defects (where I =Ag or Cu). Yuan et al. reported DFT calculations of AZTS which agree with these experimental results and assert that the reduction of I_{Zn} defects should reduce Fermi level pinning at the CdS interface and increase V_{oc}.[138] Low temperature V_{oc} measurements of $Cu_2ZnSnSe_4$ and $(Cu_{0.9}Ag_{0.1})_2ZnSnSe_4$ devices show that the PCE and V_{oc} is reduced for CZTS, while the PCE and V_{oc} increases monotonically for CAZTS (up to 600 meV and 16%at 125 K).[106] This lack of 'carrier freeze out' suggests that the energetics for carriers are substantially different for 10% Ag/(Ag+Cu) doped samples. There are multiple reports of CAZTS devices which have PCEs >10%,[105–107] and campion cells typically have 10%-30% Ag/(Ag+Cu) .

Alloys of $Cu_2Zn(Ge_y,Sn_{1-y})Se_4$ with y> 40% exhibit red-shifted PL peaks, which may be related to defect/band transitions,[66] and the highest PCE Ge-alloyed devices have been reported for y=20%-30%.[66,102,103] In contrast with Ag, alloying with Ge with CZTS does not substantially change PL FWHM, which suggests that it does not affect the Cu/Zn disorder attributed to band-tailing.[136,139] The main benefit from Ge-alloying is related to the improvement in Voc. The CZGTS devices presented in **Table 4.3** have the highest $V_{oc}/V_{oc,SQ}$ for any kesterite device ever reported (with values 61%[102] and 63%[66], respectively). This could be related to the suppression of the detrimental Sn-related point defects discussed above. Ge has a smaller atomic radius than (53 vs. 69 pm for Sn), which should suppress Zn_{IV} and Cu_{IV} defects (where IV =Sn or Ge), which are predicted to be efficient SRH recombination centers.[53]

The combination of Li-doping, Ag-alloying and Ge-alloying into a single absorber layer may have additive improvements device performance and lead to a new record PCE for

CZTS-based solar cells. DFT calculations of CZTSe, AZTSe, and CZGSe indicate that (1) the kesterite (space group $I\bar{4}$) is the most stable phase for all species, (2) the VBM consists of the Cu 3d or Ag 4d /Se 4p antibonding orbitals, and (3) the CBM consists of Sn 5s or Ge 4s /Se4p antibonding orbitals.[140,141] This suggests that the position of the VB and CB can be independently tuned by varying the Ag/(Ag+Cu) and Ge/(Ge+Sn) ratios, respectively. Since the band gaps for $(Cu_{1-x}Ag_x)_2ZnSnSe_4$ alloys have a bowing parameter in the range of interest (with measured values of 0.98, 0.95, 1.06, and 1.34 eV for x= 0.0, 0.2, 0.4),[142] while band gaps of $Cu_2ZnGe_zSn_{1-z}Se_4$ vary linearly from 1.0 to 1.5 eV,[66] this allows for a number of compositions to be explored while targeting the band gap optimal for ΔE_c^a (1.13 eV). Given that the world record device for $V_{oc}/V_{oc,SQ}$ was fabricated via spray coating a DMF-TU-based ink,[66] and that DMF-TU-based inks were shown to stabilize the chlorides Ag, Cu, Zn, Ge, and Sn as shown in **Table 4.1**, this should be achievable with the solution chemistry that we have developed. If a device can be fabricated with the same V_{oc} achieved in Ge-alloyed films along with the high FF and J_{sc} from Li-doped films, this would easily set a new world record for CZTS devices. Using values of 583 mV, 35.2 mA/cm2, and 72.3% for the V_{oc}, Jsc, and FF respectively, the simulated JV curve shown in **Figure 2.1** corresponds to a PCE of 14.8%, which would be a drastic improvement from the current record of 12.6%.

Initial a pilot study examining four compositions examining a combination of of Li-doping, Ag-alloying and Ge-alloying in kesterite devices have been quite promising. **Table 4.4** highlights four compositions which were chosen to target the 1.13 eV bandgap discussed above. Target metal ratios for the cations were I/metals=43.0%, II/metals=29.2% and IV/metals= 27.8%, which is based on champion devices for CZTS. As shown by the the data summarized in **Table 4.4** and

the best device JV curve presented in **Figure 4.9**, these devices have some of the highest $V_{oc}/V_{oc.SQ}$ values for any kesterite device ever made. Given that no optimization was performed on the metal ratios of these devices, there is massive potential for this co-alloying strategy to lead to a new world record PCE for kesterite devices.

Sample Composition	PCE (%)	V_{oc} (mV)	$V_{oc}/V_{oc.SQ}$(%)
$Cu_2Zn(Sn_{0.7},Ge_{0.3})Se_4$	10.65	514	59.3
$(Cu_{0.9},Ag_{0.1})_2Zn(Sn_{0.7},Ge_{0.3})Se_4$	9.97	549	63.0
$(Cu_{0.8},Ag_{0.2})_2Zn(Sn_{0.65},Ge_{0.35})Se_4$	11.71	581	62.7
$(Cu_{0.7},Ag_{0.3})_2Zn(Sn_{0.8},Ge_{0.2})Se_4$	9.88	574	61.9

Table 4.4 A summary of the compositions examined for a pilot study examining Ag and Ge co-alloying in CZTS. The champion device PCEs and V_{oc}s are listed for each composition.

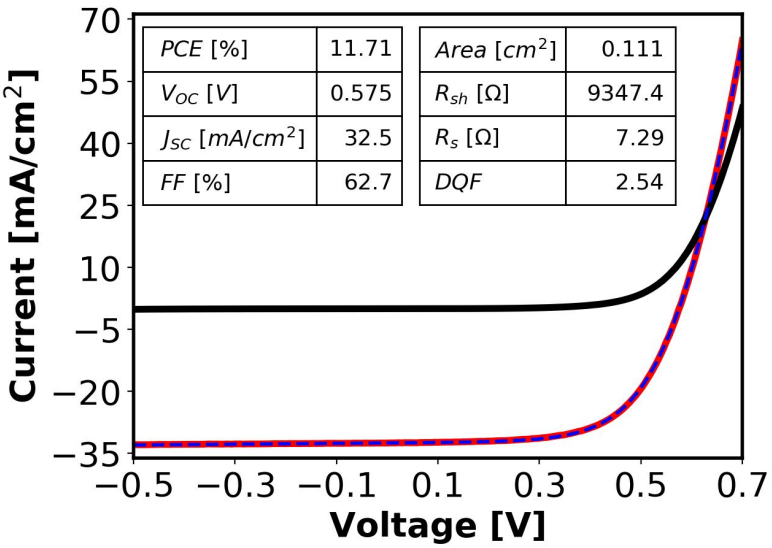

Figure 4.9 JV device characterization of the champion of a $(Cu,Ag)_2Zn(Ge,Sn)(S,Se)_4$ (CAZGTS) PV device from a small pilot study examining Ag and Ge co-alloying. This device had a composition of 20% Ag/(Ag+Cu), 35% Ge/(Ge+Sn) and Li doping of 2.5%/metals. This absorber had a bandgap of 1.17 eV (measured by PL) which corresponds to a $V_{oc}/V_{oc,SQ}$ of 62.1%.

4.7. Conclusion

This work represents a fundamental step forward in our understanding of DMF-based chalcogenide inks. In particular, these results expand on previous papers that utilized DMF-based inks for CIS[67,71] and CZGTS[66] which reported high-concentration, stable inks but did not explain the solvation mechanisms for each species. While CuCl and $InCl_3$ respectively have very low and moderate solubility in DMF alone, we showed that the solubility of both of these species can be drastically increased with Cl^- and TU. Calorimetry and solubility experiments suggest Cu(I) is stabilized via $CuCl(TU)_2$ and $Cu_nCl_{1+n}^{n-}$ (n=1,2,3), while In(III) solubility is hypothesized to increase via a similar phenomena, where Cl^- and TU affect the equilibrium between $InCl_n^{(3-n)+}$ complexes (n=0,1,2,3,4) which have been reported in DMF.[126] We also showed that the low solubility of $GeCl_4$ and CuCl is drastically increased for both species due to chloride transfer from $GeCl_4$ to CuCl .

These results, in combination with our discovery of stable $Cu_nCl_{1+n}^{n-}$ complexes, allowed us to develop a sulfur-free CISe molecular ink. Drop casting and annealing of this ink lead to photoluminescent, crystalline $CuInSe_2$ without selenization. This novel ink has excellent potential as an ultra-low-cost method to deposit a wide range selenide PV absorbers (CuInSe, CIGSe, CZTSe, and CZTGSe). Finally, the novel complex chemistry which was developed with the DMF-TU processes enable the fabrication of CAZGTS solar cells, which have some of the highest $V_{oc}/V_{oc,SQ}$ values ever reported.

Chapter 5: Electrochemical Treatment of Wastewater, Theory and Experimental Techniques

5.1 An Overview of Relevant Electrochemical Phenomena

Electrochemistry is a cheap and powerful tool to drive chemical reactions using electrical energy. In an electrolytic cell, two electrodes are immersed in a conductive solution and an external voltage is applied. On one electrode (the anode), oxidation reactions occur where electrons flow into the electrode (e.g., $2H_2O \rightarrow O_2(g) + 4H^+ + 4\ e^-$), and on the other electrode (the cathode), reduction reactions occur where electrons flow out of the anode (e.g., $2H_2O + 2\ e^- \rightarrow H_2(g) + 2OH^-$). There must always be a complete circuit between the anode and the cathode for a reaction to occur, so a conductive solution (with relatively high ionic strength) is necessary. It is also possible to isolate each electrode in separate conductive solutions and connect them with a tube filled with an electrolyte with ion-permeable caps at each end (referred to as a salt bridge). The advantage of these so-called "divided cells" is that the products of oxidation and reduction reactions can be spatially separated. This can have a number of practical advantages as shown in **Chapter 6**.

Thermodynamics, kinetics, and mass transport are the three classes of physical phenomena that are vital to understanding the behavior of electrochemical systems. The thermodynamics of a reaction set the equilibrium concentrations of oxidants and reductants for a given electrochemical reaction. This is governed by the Nernst equation, which accounts for the standard electrode potential of the reaction and the activities of the species undergoing oxidation and reduction. The kinetics of a reaction describe the rate of change in concentration of species undergoing oxidation and reduction due to activation energy barriers between the reactants and products.

This is governed by the Butler–Volmer equation, which takes into account the activation energy barrier and the activation overpotential (potential applied in excess of the equilibrium potential). Finally, since electrochemical reactions happen at the surface of electrodes, it is vital to account for mass transport of reactants toward and products away from the electrode. In the boundary layer near the electrode, mass transport is dominated by diffusion (governed by Fick's law). If there is forced convection in the solution (i.e., stirring), transport of species into and out of this boundary layer is dominated by convection (governed by the Navier-Stokes equation for incompressible flow).

5.2 Fabrication of Modular Electrochemical Cell and Electrodes

The goal of this work is to engineer a device which can be used to electrochemically oxidize pharmaceuticals, minimize the generation of toxic byproducts, and provide in-place remediation for toxic byproducts generated. This achievement of this goal requires a flexible electrochemical setup which allows for many electrodes to be quickly tested.

I designed a simple cell as shown in **Figure 5.1**, which fits a planar electrode between a base plate and the body of the cell. This is sealed with a gasket, and the stack is tightened in place by nuts and bolts. A custom cap is fitted at the top, which has a cutout for the counter and reference electrodes. In order to mimic a real device, the dimensions of the cell were chosen for a relatively high surface area to volume ratio (SA/V). The exposed area of the working electrode is 8.56 cm^2, and the cell body has a volume of ~40 cm^3 ($SA/V=0.214cm^{-1}$). The body of the device is made from teflon, and a chemical-resistant (Kalrez) rubber o-ring was used to form the seal with the planar electrode. 304 stainless steel tubes were used as the counter electrodes for

oxidation experiments, and Ti-tubes coated in IrO_2 were used as the counter electrodes in all reduction experiments.

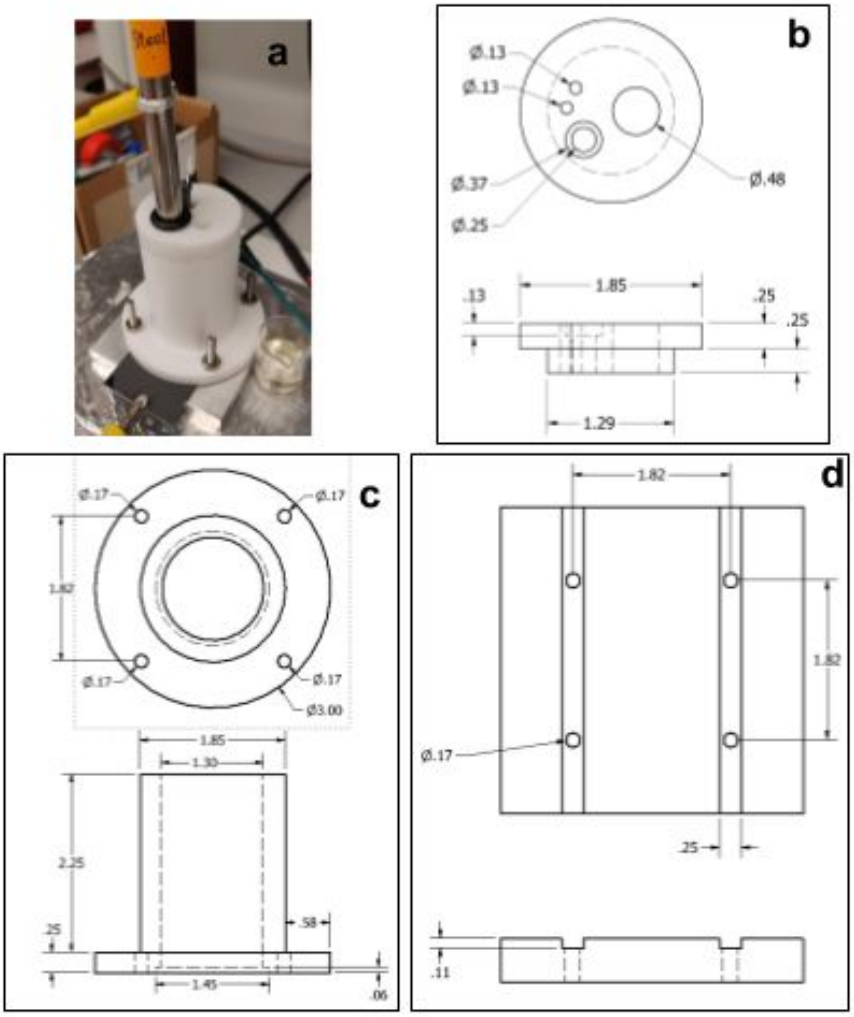

Figure 5.1 We developed a custom electrochemical cell which is able to adapt to a variety of planar electrodes, cylindrical electrodes, and custom-fritted glassware for divided cell experiments. (a) A picture of the cell in use. (b) The cap of the cell has a hole for the cylindrical counter electrode, the reference electrode and holes for gas sparging. (c) The body of the cell can accommodate ~40 mL of liquid and has an effective working electrode surface area of 8.56 cm^2. (d) The holes in the body of the cell align with the holes in the base of the cell so that they can be held together with nuts and bolts, sandwiching the planar electrode between them (sealed with a gasket).

5.3 Characterization of Electrodes and Solutions

There are a variety of electrochemical techniques and solution characterization techniques that were used to treat and characterize solutions in **Chapter 6**. A detailed discussion of all these techniques is omitted for brevity; however, **Table 5.1** gives a brief overview of the techniques. All electrochemical techniques were performed using a three electrode potentiostat with an Ag/AgCl reference electrode, where the planar electrode was the working electrode and the cylindrical electrode was the counter electrode, as depicted in **Figure 5.1**.

Technique	Abbreviation	Description
Potentiostatic Treatments	PS	A specified potential is maintained on the working electrode vs. the reference electrode. This maintains a constant driving force for reactions but the reaction rate (i.e., the current) is not controlled.
Galvanostatic Treatments	GS	The applied potential on the working electrode and the counter electrode are constantly adjusted to maintain a specified voltage. This maintains a constant reaction rate, but the applied driving force (i.e., voltage) changes to maintain it.
Cyclic Voltammetry	CV	A range of potentials is applied to the working electrode and the current is measured. This gives information about oxidation and reduction events that occur at specific voltages.
Ion Chromatography	IC	A sample is injected into a pressurized column with a mobile phase. Ions in the sample have different affinities to the column and eleute out at different times. The conductivity of the mobile phase is measured over time and peaks in the conductivity correspond to specific ions.
High-Performance Liquid Chromatography	HPLC	A sample is injected into a pressurized column with a mobile phase. Non-polar organics in the sample have different affinities to the column and eleute out at different times. The mobile phase is vaporized and the compounds of interest are measured via UV absorption and mass spectroscopy.

Table 5.1 A brief summary of analytical techniques presented in **Chapter 6**

Chapter 6: A Novel Electrochemical Scheme to Eliminate Pharmaceuticals and Toxic Byproducts in Human Urine

6.1 Introduction

Most pharmaceutical compounds are not sufficiently deactivated at wastewater treatment facilities (WWTFs) (utilizing biological treatment, electrocoagulation, coagulation and membrane filtration processes) and eventually end up being discharged into the environment. These pharmaceuticals threaten aquatic ecosystems,[143] contribute to bacterial drug resistance,[144] and eventually return to human drinking water supplies.[145] Advanced oxidation processes (AOPs) are an attractive technology to address this growing problem because of their ability to degrade most organic species via the in-situ generation of oxidizing species (i.e., $OH\cdot$, H_2O_2, $O_2\cdot$, O_3 HOCl, etc.), which can be generated through photochemical or electrochemical means.[30–32] The dominant route for pharmaceutical excretion is in urine;[146,147] therefore, decentralized AOPs, which treat this concentrated source of pharmaceuticals before it is diluted with other wastewater streams, would allow for much higher efficiency toward pharmaceutical degradation. Multiple studies have examined pharmaceutical degradation using AOPs for over a decade,[33–36] but recent works have highlighted that toxic byproducts (TBPs) (e.g. chlorate, perchlorate, haloacetic acids, aliphatic halides species, haloacetonitriles, and haloacetamides) formed during AOPs compromise the quality of the treated effluent.[37] These TBPs are mostly chlorinated species; however, brominated and iodinated species may be present at much lower concentrations but with higher toxicity.[148] Of the toxic byproducts, ClO_4^- is perhaps the biggest problem due to its exceptionally high stability and low toxicity threshold. Thus, there is a need to develop novel

AOPs that have high efficiency toward pharmaceutical reduction to prevent or mitigate ClO_4^- formation.

Multiple studies have examined the electrochemical oxidation of simulated fresh urine,[149,150] stored urine,[148,151–153] or simulated stored urine.[154] Though the details used in these studies vary significantly, there are examples where the concentrations of generated ClO_4^- for roughly equivalent oxidation treatments are vastly different. For a normalized charge passed of 30 Ahrs/L, two studies report 100% oxidation of chloride to ClO_4^-,[148,152], while another reports ClO_4^- below the detection limit.[155] One big difference between these studies is the composition of the matrix. Urine has a high concentration of nitrogen of ~10 g/L, which is bound in the form of urea.[156] However, natural abundant bacterial urease hydrolyzes urea to form ammonium, bicarbonate, and OH-. This reaction happens rapidly, with one study finding that urea is nearly completely hydrolyzed within 5 hours of storage in a pipe.[157] The dissolved ammonium is in equilibrium with dissolved ammonia, which is volatile and will evaporate over time if exposed to open air. This work aims to clarify the effects that the concentration of these dissolved constituents have on the formation of ClO_4^-.

In this work, we present two important advances in field of advanced oxidation processes for wastewater treatment. (1) We present data which reveal the beneficial effects of high ammonia content to prevent the generation of perchlorate and chlorate. This suggests a motivation to immediately treat contaminated urine at the source of generation. (2) We present a novel electrochemical scheme based on divided cells using inexpensive glass frits. This allows for the acidification of the oxidize matrix, which can be used for a subsequent reduction treatment to reduce TBPs.

6.2 The Advantages of Decentralized Treatment of Urine

Matrix	Volume [$Lp^{-1}d^{-1}$]	Matrix COD [mg/L]	Pharm COD [mg/L]	Pharm COD/Matrix COD	Required Charge Passed [A·hrs]	Daily Electricity Cost
Pure Pharmaceuticals	1.3	0	1,600.00	100%	5.81	$0.0697
Pharmaceuticals in Urine	1.3	10000	1,600.00	14%	42.10	$0.5052
Domestic Wastewater	148	702.7	14.05	2.0%	296.16	$3.5539

Table 6.1 Estimates for the the required charge and cost to electrochemically oxidize pharmaceuticals in domestic wastewater streams per person per day. These calculation assumed an electricity rate of 0.15 $/kWhr, a pharmaceutical concentration of 10 mM (which is estimated to require 100 mM of oxygen for COD calculations), an applied voltage of 6 V, a faradaic efficiency toward reactive oxidant generation of 15%, and assumes 50% of oxidants react to reduce COD. Matrix composition taken from Larsen.[158]

Point-source treatment of fresh urine has multiple advantages: (1) chemical oxygen demand (COD), (2) conductivity, (3) nitrogen content. Average human urine production is 1.3 $Lp^{-1}d^{-1}$, while average domestic wastewater discharge is 148 $Lp^{-1}d^{-1}$.[158] The dilution of urine with these other waste streams not only decreases the absolute concentration of pharmaceuticals, but it also decreases their relative concentration compared to the total concentration of organics in the solution. This is due to mixing with other organics such as cooking oils, detergents, etc. This domestic wastewater may be further diluted by other waste streams containing other organics before reaching a WWTF (e.g., industrial wastewater, urban runoff, etc.). One way to quantify this is to compare the COD from pharmaceuticals vs. the COD of the matrix on a per person per day as shown in **Table 6.1**. In a scenario where pharmaceuticals are the only source of COD in the matrix, it would take only $0.07 to oxidize all pharmaceuticals. This cost is moderately increased to $0.50 when all the COD of the urine matrix is included and is substantially

increased to $3.55 when COD from all domestic wastewater is included. The COD_{pharm}/COD_{total} decreases from 14% to 2% once the urine stream is mixed with other domestic wastewater streams. This calculations presented in **Table 6.1** represent a lower bound on the daily cost for electrochemical treatment of these systems, particularly for the larger treatment volumes. Diluted fresh urine has substantially larger volume and lower conductivity, which drastically increases the cost required to electrochemically remediate pharmaceuticals due to larger electrode requirements, longer treatment times, and high solution resistivity.

Another major benefit of treating pharmaceutical containing urine at its source is the high urea content in urine, which inhibits the formation of chlorate and perchlorate. To examine how dissolved nitrogen concentration affects the formation of perchlorate, a series of oxidations were performed on a BDD electrode as shown in **Figure 6.1**. Fresh urine has an average concentration of 250 mM Urea and 100 mM Cl-,[156] which corresponds to 500 mM NH_4^+ after urea hydrolysis. Studies which examined treatment of stored urine have measured substantially less NH_4^+ with values of 34 mM[148] and 109 mM,[152] which suggest there was substantial ammonia evaporation in these studies. As shown in **Figure 6.1**, the ClO_3^- and ClO_4^- generated during oxidation is inhibited by more than three orders of magnitude when for a matrix of 100 mM Cl^- and 250 mM urea compared to 100 mM Cl- alone. A matrix containing corresponding concentrations of hydrolyzed urine (100 mM Cl^-, 500 mM NH_4^+, and 250mM HCO_3^-) also shows the same suppression in ClO_4^- generation, but the generated ClO_3^- is one order of magnitude higher. For decreasing concentrations of NH_4^+ in the matrix, substantially more ClO_3^- and ClO_4^- is generated during oxidation. One explanation of this behavior is that ammonia species scavenge active chloride species, which inhibits their further oxidation. Urea has been measured to react with

active chlorine species at a rate of 0.63 M-1s-1,[154] and at high concentrations, this is suspected to be faster than the oxidation pathways which lead to ClO_3^- and ClO_4^-.

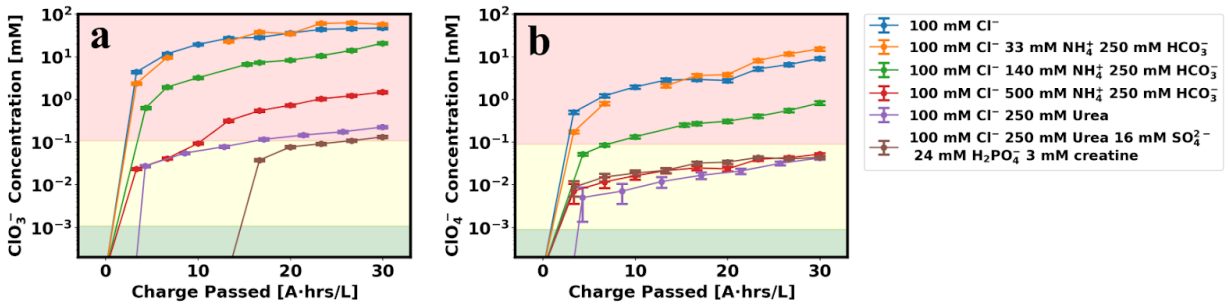

Figure 6.1 Concentrations of generated (a) ClO_3^- and (b) ClO_4^- for various matrices oxidized on a BDD anode. Green shading indicates a concentration below the drinking water recommendations of 90 ppb for ClO_4^-[159] and 200 ppb for ClO_3^-.[160] Yellow shading indicates a concentration below 100x drinking water recommendations (corresponding to typical dilution from other domestic waste water). Red shading indicates a concentration above 100x drinking water recommendations. Galvanostatic treatments were performed for 90 mins at a current density of 94 mA/cm^2 for a final charge passed of 30 A·hrs/L. Matrices with high nitrogen content corresponding to the concentration of fresh urine (250 mM urea or 500 mM NH_4^+) show a three order of magnitude suppression in the generated ClO_3^- and ClO_4^- compared to a nitrogen free matrix.

6.3 The Oxidation of Pharmaceutical in a Simple Urine Matrix

Figure 6.2 shows CVs of oxidative sweeps of three different solutions on boron-doped diamond (BDD) and thermally decomposed iridium oxidize (IrO_2). The CVs of BDD in **Figure 6.2a** show a difference of 200 mV in the onset of current between the ClO_4^- and other solutions. This is due to the lower overpotential required for chlorine evolution vs. oxygen evolution on BDD. In the Cl^- solution, there is a rapid increase in the current in the anodic sweep near 1.9 V, which corresponds to the oxidation of active chlorine species.[161] This is absent in the Cl^- and urea solutions, suggesting that the active chlorine species have been scavenged by the urea. This is commensurate with the suppression of ClO_3^- and ClO_4^- generation shown in **Figure 6.1**.

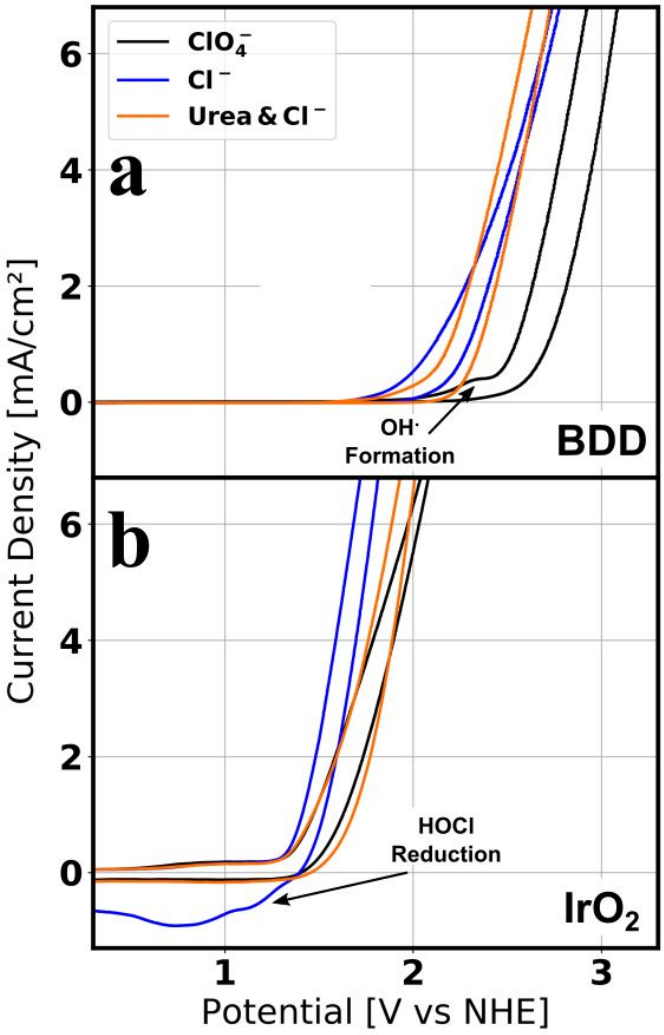

Figure 6.2 Cyclic voltammograms (CVs) of in 0.1 M $NaClO_4$, 0.1 M NaCl, and 0.1M NaCl + 0.25 M Urea on (a) BDD and (b) IrO_2 anodes. The CV of 0.1 M NaCl oxidized on BDD exhibits an oxidation peak whichis attributed to the oxidation of HOCl. This peak is absent in 0.1 M NaCl + 0.25 M Urea CV, which suggests that urea scavenges HOCl. A similar phenomena is observed in the IrO_2 CVs where the HOCl reduction peak is apparent in the 0.1 M NaCl matrix and absent from the 0.1 M NaCl + 0.25 M Urea matrix.

In contrast to BDD, the CVs of IrO_2 in **Figure 6.2b** show little difference in the onset of current evolution and magnitude of current when Cl^- is present. The surface of IrO_2 anodes are known to oxidize according to $IrO_2 + H_2O \rightleftharpoons Ir(OH)_3 + H^+ + e^-$.[162] Therefore, the oxidation pathways involving these surface oxides toward Cl_2 and O_2 must have similar kinetics. In the Cl- only

solutions on IrO_2, the peak seen in the cathodic sweep from 1.2 to 0 V likely corresponds to the reduction of oxidized chlorine species, such as HOCl or surface-bound $Cl^{\cdot}$. The absence of this peak when urea is present in the matrix again demonstrated that urea scavenges HOCl and/or surface-bound $Cl^{\cdot}$.

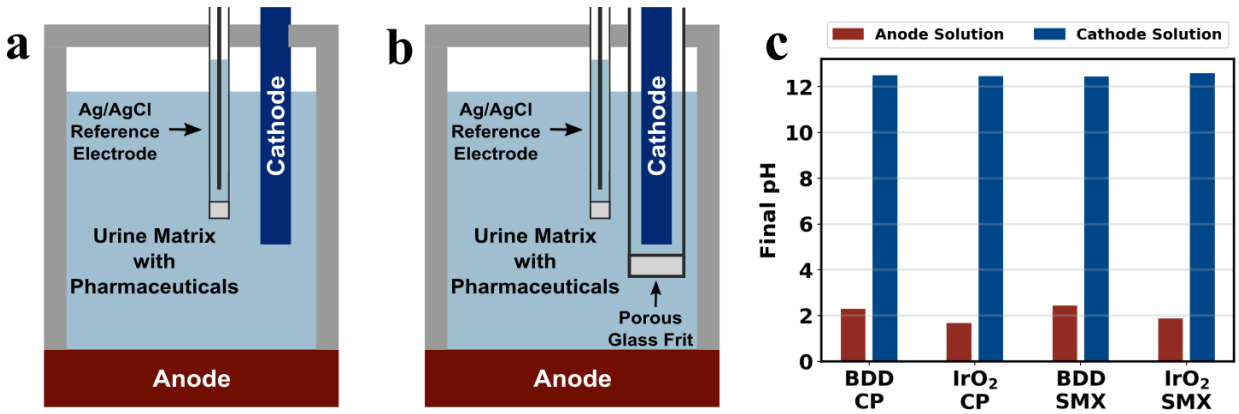

Figure 6.3 Cyclic voltammograms (CVs) of in 0.1 M $NaClO_4$, 0.1 M NaCl, and 0.1M NaCl + 0.25 M Urea on (a) BDD and (b) IrO_2 anodes. The CV of 0.1 M NaCl oxidized on BDD exhibits an oxidation peak with is attributed to the oxidation of HOCl. This peak is absent in 0.1 M NaCl + 0.25 M Urea CV, which suggests that urea scavenges HOCl. A similar phenomena is observed in the IrO_2 CVs where the HOCl reduction peak is apparent in the 0.1 M NaCl matrix and absent from the 0.1 M NaCl + 0.25 M Urea matrix.

In order to examine the potential of point-source treatment of pharmaceuticals in fresh-urine matrices, a series of experiments were performed with BDD and IrO_2 anodes. Oxidation experiments were performed on both of these electrodes with one of two pharmaceuticals, sulfamethoxazole (SMX) and cyclophosphamide (CP), each in a non-divided and divided cell configuration. CP and SMX were chosen as test compounds because of their major differences in reactivity toward active chlorine species. SMX has a relatively high bimolecular rate constant with HOCl of 10^3 $M^{-1}s^{-1}$,[163] while we measured CP to have an exceptionally low bimolecular rate constant of ~10^{-6} $M^{-1}s^{-1}$. A schematic of the non-divided and divided cell configurations for

oxidation are shown in **Figure 6.3a** and **Figure 6.3b**, respectively. For the divided cell setup, a glass frit (with porosity 4-8 um) proved to be a simple, cheap way to prevent mixing of solutions in the anode and cathode compartments. Furthermore, this led to large pH difference between the two compartments as shown in **Figure 6.3c**. The pH gradient is established because the oxygen evolution reaction at the anode generates H+ while the hydrogen evolution reaction at the cathode generates OH-. Positive ions flow from anode to cathode, and negative ions flow from cathode to anode through the glass frit, which counteracts this gradient. However, given that Na+ and Cl- are both at 0.1 M, H+ and OH- are expected to accumulate in the anode and cathode chambers until their concentration is on the order of Na+ and Cl-. On average, the pH in the anode chamber stabilized to 1.8 and 2.3 for IrO_2 and BDD, respectively. Furthermore, this gradient is quickly established. Passing 10 mA/cm2 for 5 mins (~0.2 A.hrs/L) was sufficient to establish a gradient of ~10 pH units for both BDD and IrO_2. This simple, inexpensive technique to adjust the pH of the matrix has many potential advantages. (1) Acidification of urine to pH 2 has been shown to prevent hydrolysis of urea for over 200 days.[164] This could prove useful to prevent urea hydrolysis and ammonia loss for device designs where large volumes of concentrated urine are collected before treatment. (2) Many pharmaceuticals have different susceptibility to oxidation depending on the solution pH, typically due to the protonation/deprotonation of amine groups. Controlled mixing of the basic cathode compartment solution with the anode compartment solution could be used to set the pH to a value that maximizes degradation of a particularly recalcitrant pharmaceutical. (3) Low pH environments are generally more favorable toward reduction. Therefore, the efficacy of subsequent reduction

treatments on the anode compartment solution to degrade TBPs is expected to be drastically enhanced.

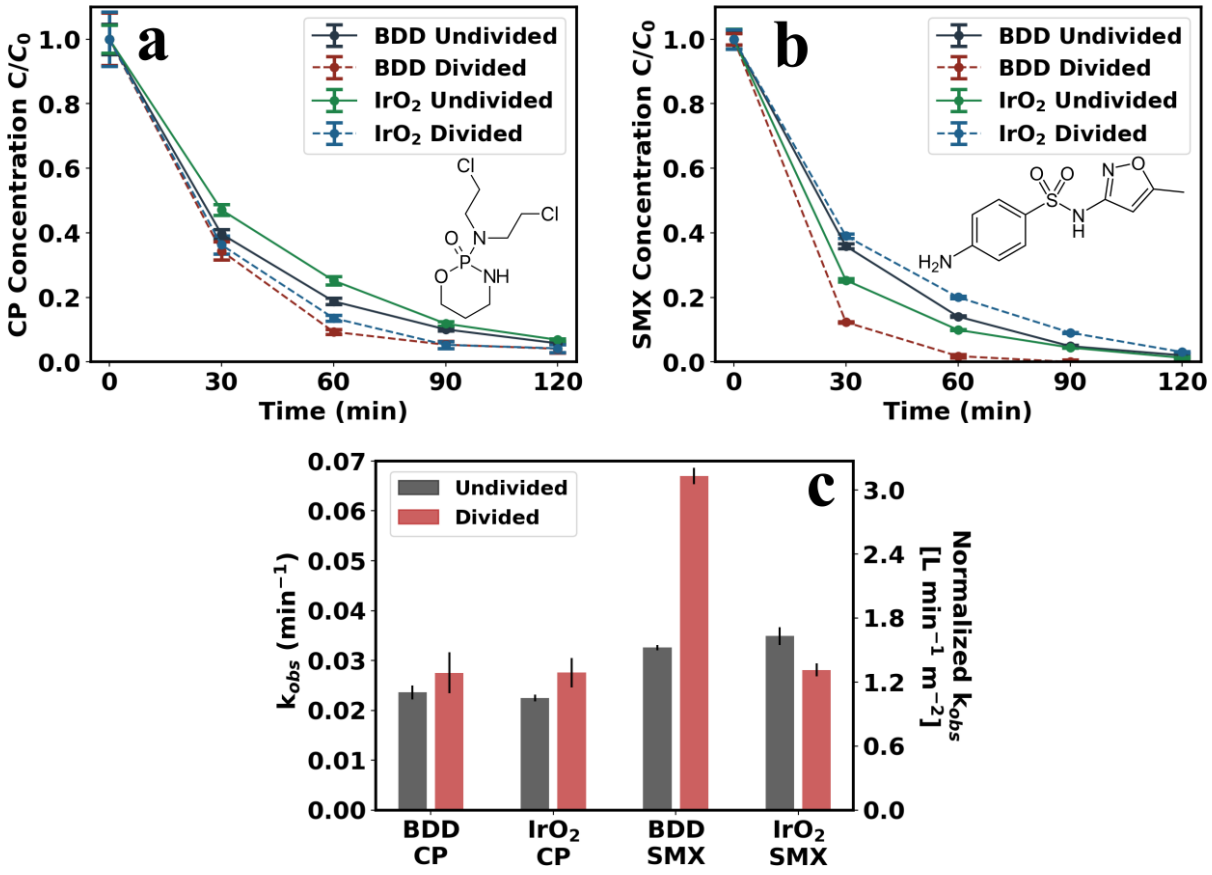

Figure 6.4 Results from oxidation experiments of a simple urine matrix spiked with a pharmaceutical at 10 mA/cm^2 on BDD and IrO_2 anodes in the undivided and divided setups. 120 mins of oxidation corresponds to 4.28 A·hrs/L. (a) Concentration of cyclophosphamide (CP) over the course of the oxidation with a starting CP concentration of 500 ppm. Inset: The chemical structure of CP. (b) Concentration of sulfamethoxazole (SMX) over the course of the oxidation with a starting SMX concentration of 100 ppm. Inset: The chemical structure of SMX. (c) Observed first-order rate constants for pharmaceutical degradation.

The rate of pharmaceutical degradation and the rate of toxic byproduct generation were compared between every combination of pharmaceutical, anode, and cell configuration as shown in **Figure 6.4** and **Figure 6.5** respectively. **Figure 6.4** shows that CP and SMX can be degraded to below 90% of their starting value after two hours of oxidation at 10 mA/cm^2 (4.28 A hrs/L) for

both cell setups on each electrode. The observed pseudo-first-order rate constant for degradation was similar for both electrodes, with the exception of SMX on BDD which had an exceptionally higher degradation rate constant. This higher rate constant could be partially due to the higher dissolved oxidant concentration (**Figure 6.5j**), but a such a drastic improvement was not seen on IrO_2 despite a similar increase in dissolved oxidants. We hypothesize that large increase in the SMX degradation in the BDD divided cell was due to higher concentrations of $Cl^{\cdot}$. A pH-dependent equilibrium of $ClOH^{\cdot-}$ with $Cl^{\cdot}$ and $HO^{\cdot}$ has been shown to favor $Cl^{\cdot}$ at low pH and $HO^{\cdot}$ at high pH. Given the exceptionally high rate of reactivity of SMX toward chlorinated byproducts via active chlorine species, we suspect that $Cl^{\cdot}$ reacts faster with SMX than the $OH^{\cdot}$. Both perchlorate (**Figure 6.5a,b**) and chlorate (**Figure 6.5c,d**) were near or below the detection limit for the ion chromatography techniques used in these experiments. No perchlorate was measured in matrices oxidized by the IrO_2 anode, which is similar to what has been reported previously.[148,155] Perchlorate was formed in the matrices oxidized on the BDD anode, but much lower concentrations than what has been reported previously.[148,152] This is due to the urea in solution as discussed about in Section 3.1. Nitrate (**Figure 6.5e,f**) and nitrite (**Figure 6.5g,h**) generation was found to be higher on the IrO_2 electrode than the BDD electrode. These nitrogen compounds could come from the oxidation of urea and/or the oxidation of CP/SMX. However, in the IrO_2 divided cell experiments, nitrate generation was substantially reduced and nitrite was below the detection limit. A reaction pathway with nitrite and $OH^{\cdot}$ has been shown to lead to nitrosamines, which are acute TBPs.[165] Therefore, the suppression of both the NO_2 and the NO_3 in using the IrO_2 divided cell configuration is an indication that these pathways are not active. Quantification of the dissolved oxidants (**Figure 6.5i,j**), showed that they were 2-10x more

concentrated in the divided cell setup. This is likely related to the fact that in an undivided setup, dissolved oxidants such as H_2O_2 and HOCl are expected to be reduced at the cathode.

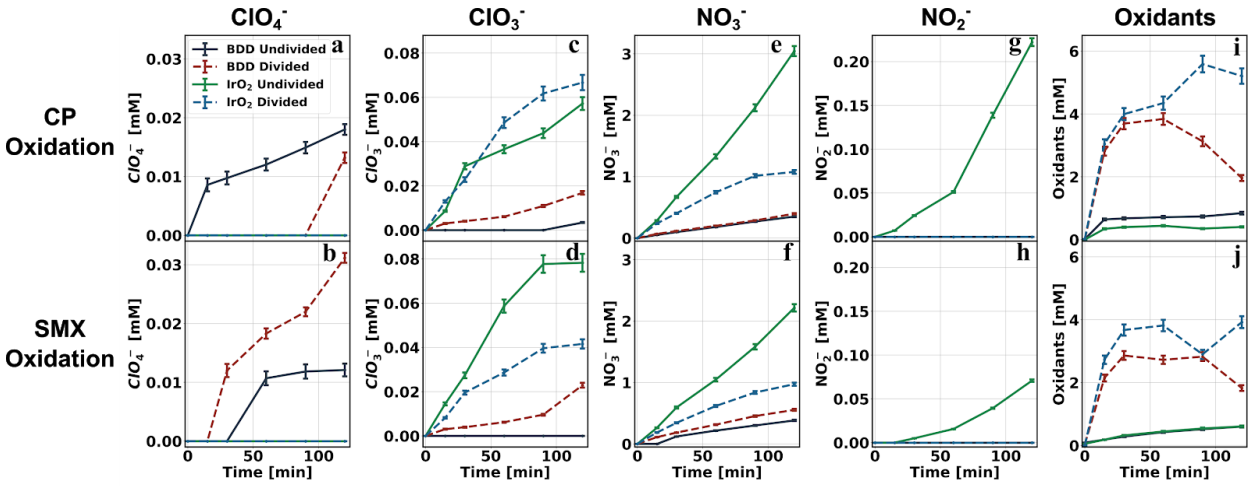

Figure 6.5 Concentration of (a,b) ClO_4^-, (c,d) ClO_3^-, (e,f) NO_3^-, (g,h) NO_2^-, and (i,j) dissolved oxidants measured over the course of two hours of oxidation at 10 mA/cm^2 on BDD and IrO_2 anodes in the undivided and divided setups. 120 mins of oxidation corresponds to 4.28 A·hrs/L. (a,c,e,g,i) Results from oxidation of simple urine matrix with 500 ppm CP. (b,d,f,h,j) Results from oxidation of simple urine matrix with 100 ppm SMX. Dissolved oxidants were quantified SO_4^{2-} by spiking samples taken for IC with $Na_2S_2O_3$.

6.4 The Reduction of TBPs in an Acidified Urine Matrix

In order to demonstrate the potential of a reduction treatment after an advanced oxidation process, we performed a series of reduction experiments on platinum (Pt), molybdenum (Mo), and titanium (Ti) cathodes. **Figure 6.6** compares the CVs of these cathodes for four matrices: NaCl at pH 7, NaCl at pH 2, $NaClO_3$ at pH 2, and $NaClO_4$ at pH 2. CVs of $NaClO_3$ and $NaClO_4$ solutions at pH 7 look identical to the Cl^- pH 7 solution. The peaks corresponding to chlorate and perchlorate reduction are only present at pH 2. A prominent cathodic peak for the NaCl at pH 2 matrix is seen at -0.7 V, -1.0 V, and -1.5 V for Pt, Mo, and Ti respectively. A similar peak has been previously attributed to adsorption of hydrogen at the cathode for Pt,[166] and this peak is all but absent for the CVs of the NaCl/pH 7 matrix. We therefore attribute this peak to the

adsorption of hydrogen for all of these cathodes. For the ClO_4 containing matrix, the hydrogen adsorption peak is decreased for the Mo and Ti electrodes. This may be indicative of surface bound ClO_4 reducing the surface area for hydrogen adsorption. For all electrodes, the desorption of hydrogen can be seen during the anodic sweep, with the highest magnitude for the NaCl/pH 7 matrix. This is due to the low concentration of H+ in solution, which provides a relatively strong driving force for the desorption of surface bound hydrogen. ClO_3^- is readily reduced by all electrodes, as indicated by the prominent cathodic peak at -0.4, -0.4, and -0.7 V for Pt, Mo, and Ti respectively. Note the absence of a hydrogen adsorption peak for the pH 2 chlorate solution. The hydrogen ion concentration is an order of magnitude less than that of chlorate, and since it is directly involved in the reduction of chlorate, the cathode the hydrogen adsorption peak is absent. From **Figure 6.6**, we can see Pt is most favorable towards the hydrogen evolution reaction (HER), Mo has a slightly later onset potential, and Ti has the largest inert window.

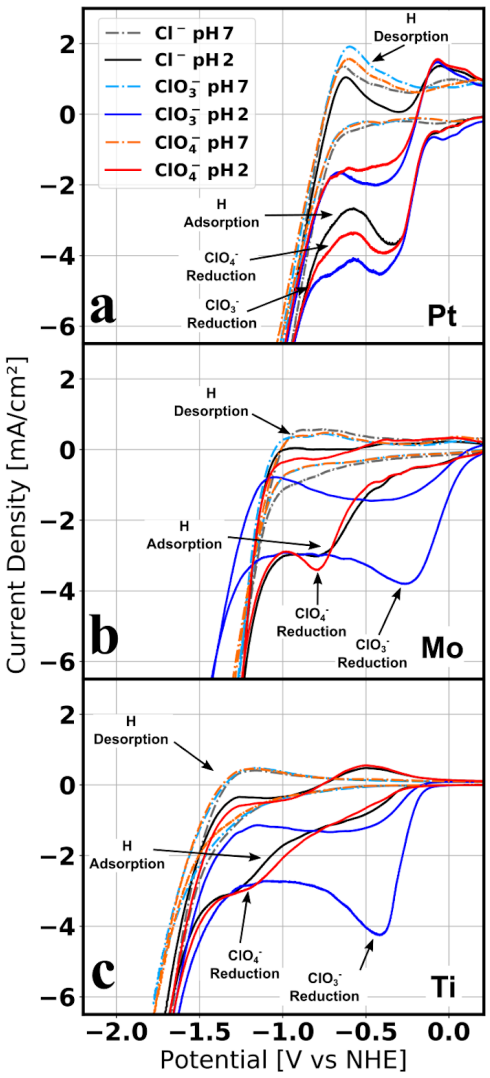

Figure 6.6 A comparison of cyclic voltammograms for 0.1 M Cl^- at pH 7, 0.1 M Cl^- at pH 2, 0.1 M ClO_3^- at pH 2, and 0.1 M ClO_4^- at pH 2 on Pt (a), Mo (b) , and Ti (c) cathodes. Sodium is the corresponding cation for all anions and pH was adjusted using HCl. Clear peaks can be identified for hydrogen adsorption/desorption and ClO_3^- reduction on all cathodes. CVs of 0.1 M ClO_3^- at pH 7, and 0.1 M ClO_4^- at pH 7 were also measured and appeared very similar to 0.1 M Cl^- at pH 7, suggesting that low pH is required for significant reduction events to occur.

In order to test the optimum reduction conditions for the oxidized urine matrix, a pH 2 solution with 5 ppm of ClO_4^- and 30 ppm of ClO_3^- was reduced on Pt, Mo, and Ti cathodes. In all of these experiments, a potentiostatic voltage was maintained (at -400, -550, -700, or -850 mV) for 3 hours in a divided cell (as depicted in **Figure 6.7a**), and the concentration of ClO_3^- and

ClO_4^- were measured over time. A key feature of this experiment is the competition between the HER and the reduction of the oxychlorides, both of which consume surfaced adsorbed hydrogen.[166,167] The final pH of the solutions was drastically increased for the Pt cathode, moderately increased for the Mo cathode, and slightly increased for the Ti cathode (**Figure 6.7b**). An increasing kinetic barrier for the HER in order of Ti>Mo>Pt explains this pH difference, which is further supported by the difference in the inert potential window in **Figure 6.6**. The change in the ClO_3^- and ClO_4^- concentration over time was used to extract first order rate constants, which can be found in **Figure 6.7c** and **Figure 6.7d**. Ti proved to have exceptionally fast kinetics toward the reduction of ClO_3^-, with almost complete removal from the matrix in 3 hours when held at potentiostatic voltage of -850 mV. The rate constant for ClO_3^- reduction increased monotonically on Ti for the potentials studied, which is likely related to the increasing driving force toward ClO_3^- reduction while not generating much hydrogen (as indicated by the constant pH). By contrast, the rate constant for ClO_3^- reduction decreased monotonically on Mo, while the pH of the final solution increased. This indicates a higher faradaic efficiency toward the HER and a lower faradaic efficiency toward ClO_3^- reduction as potential is increased. This is even more drastic in the case of Pt, where no measurable ClO_3^- reduction was measured. A moderate amount of ClO_4^- was reduced in the time-scale of this experiment on all electrodes.

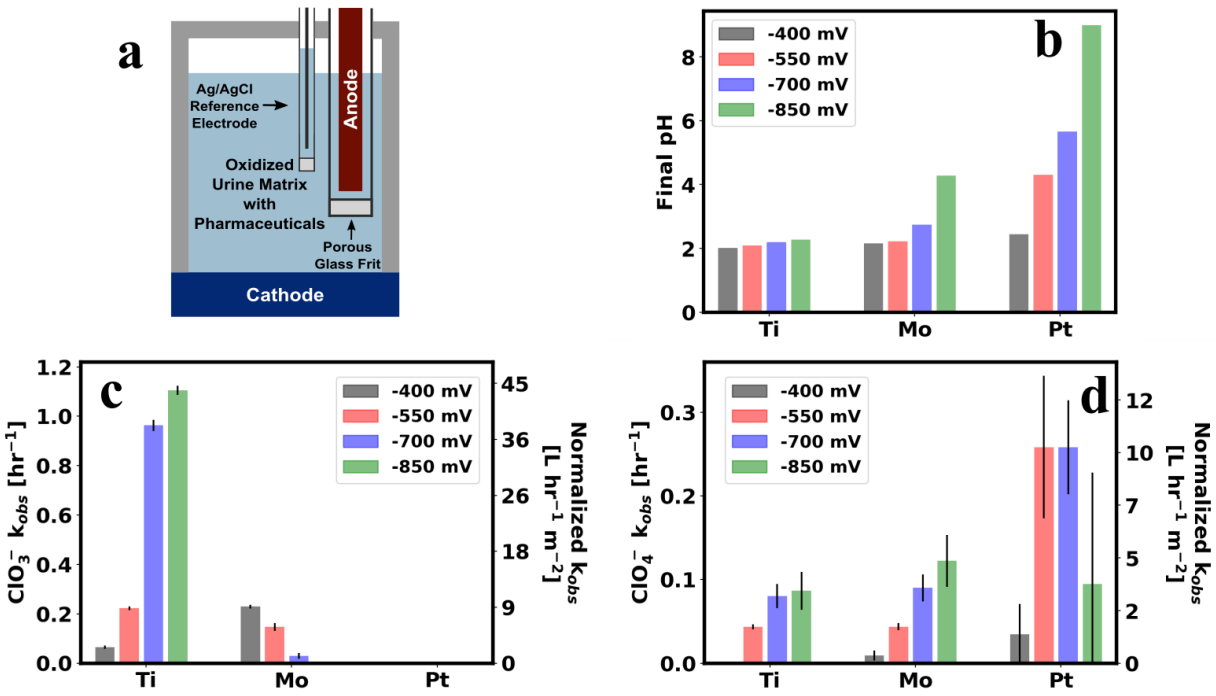

Figure 6.7 (a) A schematic of the reducicing divided cell setup. (b,c,d) Results of reduction experiments performed on Ti, Mo, and Pt cathodes in the reducing divided cell setup, where cathodes were held at the indicated voltages for 3 hours. The initial concentrations of ClO_3^- and ClO_4^- were 30 ppm and 5 ppm respectively, and initial pH was 2.00. This composition is similar to the composition after 120 mins of oxidation in the divided cell setup. (b) Final pH of the cathodic solutions. High final pH is indicative of the hydrogen evolution reaction. (c,d) First-order degradation rate constants for ClO_3^- (c) and ClO_4^- (d). These data indicate that ClO_3^- and ClO_4^- can be reduced

6.5 Alternation of Oxidation and Reduction

In order to demonstrate the potential of a subsequent reduction treatments in AOPs to remediate TBPs, we performed a reduction treatment on an acidified oxidized urine matrices as shown in **Figure 6.8**. The original matrix contained 100 mM NaCl, 250 mM urea, and 500 ppm and showed little evidence of other constituents (apart from $S_2O_3^{2-}$) as shown by the black trace shown in **Figure 6.8a**.

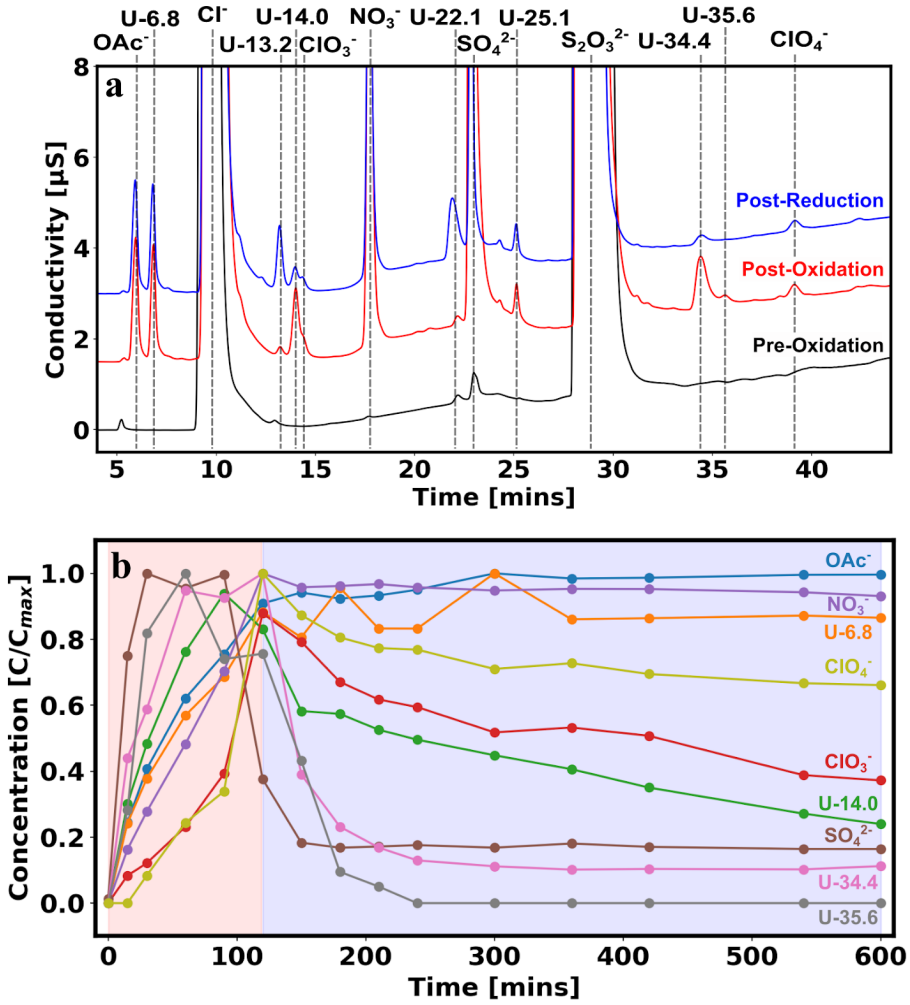

Figure 6.8 (a) Raw ion-chromatography data for (1) simple urine matrix with 500 ppm CP before oxidation, (2) after oxidation on BDD at 10 mA/cm^2 for 120 minutes (4.28 A.hrs/L) in divided cell set-up, and (3) after a subsequent reduction on Ti at -850 mV for 480 mins. (b) Normalized concentration of various anions during the oxidation (shaded in red) and the subsequent reduction (shaded in blue). These data illustrate the potential of a post-oxidation reduction treatment to remediate ClO_3^- and ClO_4^-

As shown by the blue trace, after oxidation on BDD at 10 mA/cm^2, a number of oxidation byproducts form, including ClO_3^- and ClO_4^-. A number of IC peaks corresponding to oxidation byproducts are highlighted with guidelines in **Figure 6.8a,** and their peak areas (normalized to the maximum peak area) are tracked over the course of the oxidation experiment in the red shaded region of **Figure 6.8b**. A subsequent reduction treatment was performed using a Ti

electrode maintained at -850 mV for 480 mins, and the same IC peaks are tracked in the blue region of **Figure 6.8b**. As expected, based on the reduction experiment highlighted in **Figure 6.7**, there was a decrease in the concentration in the ClO_3^- and ClO_4^-, however; the rate was slower that previously measured. This may in part be due to the competitive reduction of other unknown oxidation byproducts, which are labeled U-14.0. U-34.4, and U-35.5. The final pH of the solution before reduction was 2.3, and it rose to 9.0 after the 480 min reduction treatment. This may suggest that the reduction potential of -850 mV was high enough for the HER to slowly raise the pH over time. Nevertheless, these data are a promising illustration of the the potential of post-oxidation reduction treatments to reduce TBPs using these divided cell schemes.

6.6 Conclusion

This work has presented two important contributions to research on electrochemical advanced oxidation processes. We demonstrated that ammonia species play an important role in inhibiting the formation of ClO_3^- and ClO_4^- during advanced oxidation processes. This is an important result that provides additional motivation for decentralized use of AOPs to eliminate pharmaceuticals at the source of generation. This work also presented a novel electrochemical scheme which can be used to establish large pH gradients. These can be used to facilitate the reduction of toxic byproducts such as ClO_3^- and ClO_4^-.

Chapter 7: Concluding Remarks and Future Directions

7.1 Outcomes from Solution-Processed Chalcogenide Research

DMSO-TU and DMF-TU based molecular inks have led to some of the highest PCE solution-processed PV devices based on chalcogenide absorbers. The work presented in **Chapter 3** represents an important contribution toward understanding the chemical mechanisms involved in impurity transport out of absorbers from DMSO-TU and DMF-TU (and many other) solution processes. This work also clarified that Li-doping leads to sodium flux from the substrate, which facilitates the removal of impurities. Finally, the work highlights preliminary research on sulfurization as a method to remove impurities in these systems. The work presented in **Chapter 4** revealed previously unknown complexation mechanisms in the DMF-TU molecular ink and introduced a novel method to deposit $CISe_2$ without selenization. Finally, the DMF-TU complexation chemistry facilitated the stabilization of Ag and Ge in solution, which was used to fabricate the first germanium and silver coalloyed kesterite devices. These devices have some of the highest $V_{oc}/V_{oc,SQ}$ values ever reported for kesterite PV materials.

7.2 Future Work for Solution-Processed Chalcogenides

As described in **Chapter 1**, the future of solution-processed chalcogenide research is uncertain. The combination of falling prices for Si PV, the rise of solution-processed hybrid perovskites, and stagnet PCEs for solution-processed chalcogenide devices require a breakthrough if research in this technology is to continue. The biggest challenge for kesterite devices remains the low $V_{oc}/V_{oc,SQ}$; therefore, research must focus on solving this problem above all else. While there are a number of hypotheses about the origin of the low open circuit voltage

in these devices, I suspect that the origin is related to Sn-site defects that pin the electron quasi-fermi level under illumination. Given my knowledge of the large body of work on alloying different elements into CZTS, I believe that combination of Ag and Ge alloying has the best chance at improving the V_{oc} in kesterite devices. Results from the pilot study presented in **Figure 4.9** show one of the highest $V_{oc}/V_{oc,SQ}$ values ever reported for a kesterite device without any optimization of the parameter space. Follow-up work should perform a systematic exploration of vast metal ratio parameter space, including the ratios on the sites (Ag/(Ag+Cu)) and the ratios between the sites (I/(I+II+IV)). I also recommend that this work systematically examine the interaction between the selenization conditions (particularly the temperature) and the composition of the material. Given the extensive body of literature on order-disorder transitions in kesterite materials (i.e., post selenization annealing), I also recommend that future work examine the effects of controlled decreases to cation disorder in the alloyed materials.

7.3 Outcomes from Electrochemical Treatment of Urine Research

In the final nine months of my PhD, I made a substantial change in my research direction to contribute to an emerging research effort in the Hillhouse research group. In this time, I familiarized myself with the electrochemistry literature, designed and fabricated a custom electrochemical cell, and learned a suite of new analysis techniques, all of which led to the discoveries highlighted in **Chapter 6**. This work targeted one of the biggest challenges facing advanced oxidation processes (AOPs) (the generation of toxic byproducts) and provided two complementary solutions. This work showed that the dissolved nitrogen species in urine inhibit the formation of chlorate and perchlorate in AOPs by three orders of magnitude lower than when they are not present. It also presented a novel electrochemical scheme which can be used to

acidify the matrix during AOPs. This was leveraged in a post-oxidation reduction step that was shown to reduce the concentration of chlorate, perchlorate, and other oxidation byproducts.

7.4 Future Work for Electrochemical Treatment of Urine

The electrochemical scheme presented in **Chapter 6** is excellent groundwork for a variety of follow-up research projects. Fundamental research on how the other constituents of urine affect oxidant concentrations, pharmaceutical degradation pathways, and toxic-byproduct generation during oxidation is vital to developing a better scientific understanding of these systems. In particular, an effort should be made to perform these experiments in divided cells, given that these systems are less studied and different pathways will be active at low pH. A important next step toward the realization of an inexpensive device is the development of a cheap anode that can oxidize a wide range of compounds. Given that IrO_2 and BDD were both able to degrade cyclophosphamide (a relatively recalcitrant compound), I suggest remaining open to active and inactive electrodes. Two promising candidate anodes are graphite and F-doped SnO_2. Finally, I recommend a continued research effort to examine reduction treatments after AOPs to reduce toxic byproducts. This includes the development of novel cathodes which catalyze perchlorate reduction, the exploration novel device schemes (e.g., which use electrolytically generated H_2 for reduction), and the study of additional cathdoes to reduce other TBPs.

References

1. Clark, J. A., Uhl, A. R., Martin, T. R. & Hillhouse, H. W. Evolution of Morphology and Composition during Annealing and Selenization in Solution-Processed Cu2ZnSn(S,Se)4. Chem. Mater. 29, 9328–9339 (2017).
2. Clark, J. A. et al. Complexation Chemistry in N,N-Dimethylformamide-Based Molecular Inks for Chalcogenide Semiconductors and Photovoltaic Devices. J. Am. Chem. Soc. **141,** 298–308 (2018).
3. Uhl, A. R. et al. Solution-Processed Low-Bandgap CuIn(S,Se)2 Absorbers for High-Efficiency Single-Junction and Monolithic Chalcopyrite-Perovskite Tandem Solar Cells. Adv. Energy Mater. **8,** (2018).
4. A Novel Electrochemical Scheme to Eliminate Pharmaceuticals and Toxic Byproducts in Human Urine. *(In prep)*
5. Pecl, G. T. et al. Biodiversity redistribution under climate change: Impacts on ecosystems and human well-being. Sci. **355,** (2017).
6. Rizzo, L. et al. Urban wastewater treatment plants as hotspots for antibiotic resistant bacteria and genes spread into the environment: a review. Sci. Total. Environ. **447,** 345–360 (2013).
7. Heath, Y. & Gifford, R. Free-Market Ideology and Environmental Degradation: The Case of Belief in Global Climate Change. Environ. Behav. **38,** (2006).
8. Hornsey, M. J., Harris, E. A., Bain, P. G. & Fielding, K. S. Meta-analyses of the determinants and outcomes of belief in climate change. Nat. Clim. Chang. **6,** (2016).
9. Nozik, A. Exciton Multiplication and Relaxation Dynamics in Quantum Dots: Applications to Ultra-High Efficiency Solar Photon Conversion. in 2006 IEEE 4th World Conference on Photovoltaic Energy Conference 40–44 (IEEE). doi:10.1109/WCPEC.2006.279341
10. Fraunhofer Institute for Solar Energy Systems PHOTOVOLTAICS REPORT. https: //www.ise.fraunhofer.de/content/dam/ise/de/documents/publications/studies/Photovoltaics-Report.pdf. (2018).
11. Ener, R. A. Response from Dr. Ener. Pain Med. **5,** (2004).
12. Green, M. A. et al. Solar cell efficiency tables (version 51). Prog. Photovoltaics: Res. Appl. **26,** (2018).
13. Panthani, M. G. et al. High efficiency solution processed sintered CdTe nanocrystal solar cells: the role of interfaces. Nano Lett. **14,** 670–675 (2014).
14. Wang, W. et al. Device Characteristics of CZTSSe Thin-Film Solar Cells with 12.6% Efficiency. Adv. Energy Mater. **4,** 1301465 (2014).
15. Zhang, T. et al. High efficiency solution-processed thin-film Cu(In,Ga)(Se,S)2 solar cells. Energy & Environ. Sci. **9,** (2016).
16. Powell, D. M., Ran Fu, K., Horowitz, P. A., Basore, M. W. & Buonassisi, T. The Capital Intensity of Photovoltaics Manufacturing: Barrier to Scale and Opportunity for Innovation. Energy & Environmental Science **8,** 3395–3408 (2015).
17. Shay, J. L., Wagner, S. & Kasper, H. M. Efficient CuInSe2/CdS solar cells. Appl. Phys. Lett. **27,** (1975).
18. Katagiri, H. et al. Preparation and evaluation of Cu2ZnSnS4 thin films by sulfurization of E ▪ B evaporated precursors. Sol. Energy Mater. Sol. Cells **49,** (1997).

19. NREL Open PV Project Breakeven Analysis.
20. Chapin, D. M., Fuller, C. S. & Pearson, G. L. A New Silicon p-n Junction Photocell for Converting Solar Radiation into Electrical Power. J. Appl. Phys. **25,** (1954).
21. Klein, E. Y. et al. Global increase and geographic convergence in antibiotic consumption between 2000 and 2015. Proc. Natl. Acad. Sci. United States Am. **115,** E3463–E3470 (2018).
22. U.S. Food & Drug Administration: Novel Drug Approvals for 2017. https://www.fda.gov/Drugs/DevelopmentApprovalProcess/DrugInnovation/ucm537040.htm (accessed 2017-10-01).
23. Lassen, L. C. & Thomsen, M. K. Global health: the ethical responsibility of the pharmaceutical industry. Dan. Med. Bull. **54,** 35–36 (2007).
24. THE PHARMACEUTICAL INDUSTRY AND GLOBAL HEALTH. https://www.ifpma.org/wp-content/uploads/2017/02/IFPMA-Facts-And-Figures-2017.pdf (accessed 2019-5-30)
25. Majors-Foley, K. Use of and Barriers to Access to Opioid Analgesics: A Worldwide, Regional, and National Study. J. Emerg. Med. **51,** (2016).
26. Petrovic, M. et al. Fate and removal of pharmaceuticals and illicit drugs in conventional and membrane bioreactor wastewater treatment plants and by riverbank filtration. Philos. Trans. Ser. Math. Phys. Eng. Sci. **367,** 3979–4003 (2009).
27. Wang, J. & Wang, S. Removal of pharmaceuticals and personal care products (PPCPs) from wastewater: A review. J. Environ. Manag. **182,** 620–640 (2016).
28. Li, W. C. Occurrence, sources, and fate of pharmaceuticals in aquatic environment and soil. Environ. Pollut. **187,** 193–201 (2014).
29. Benotti, M. J. et al. Pharmaceuticals and endocrine disrupting compounds in U.S. drinking water. Environ. Sci. & Technol. **43,** 597–603 (2009).
30. Moreira, F. C., Boaventura, R. A. ., Brillas, E. & Vilar, V. J. . Electrochemical advanced oxidation processes: A review on their application to synthetic and real wastewaters. Appl. Catal. B: Environ. **202,** (2017).
31. Panizza, M. & Cerisola, G. Direct and mediated anodic oxidation of organic pollutants. Chem. Rev. **109,** 6541–6569 (2009).
32. Chong, M. N., Jin, B., Chow, C. W. K. & Saint, C. Recent developments in photocatalytic water treatment technology: a review. Water Res. **44,** 2997–3027 (2010).
33. Barazesh, J. M., Prasse, C. & Sedlak, D. L. Electrochemical Transformation of Trace Organic Contaminants in the Presence of Halide and Carbonate Ions. Environ. Sci. & Technol. **50,** 10143–10152 (2016).
34. Sopaj, F. et al. Influence of the anode materials on the electrochemical oxidation efficiency. Application to oxidative degradation of the pharmaceutical amoxicillin. Chem. Eng. J. **262,** (2015).
35. Domínguez, J. R. et al. Electrochemical Degradation of a Real Pharmaceutical Effluent. Water, Air, & Soil Pollut. **223,** (2012).
36. Ciríaco, L., Anjo, C., Correia, J., Pacheco, M. . & Lopes, A. Electrochemical degradation of Ibuprofen on Ti/Pt/PbO2 and Si/BDD electrodes. Electrochimica Acta **54,** (2009).
37. Radjenovic, J. & Sedlak, D. L. Challenges and Opportunities for Electrochemical Processes as Next-Generation Technologies for the Treatment of Contaminated Water. Environ. Sci. &

Technol. **49,** 11292–11302 (2015).
38. Scheer, R. & Schock, H.-W. Chalcogenide Photovoltaics: Physics, Technologies, and Thin Film Devices. (Wiley-VCH Verlag GmbH & Co. KGaA, 2011). doi:10.1002/9783527633708
39. Nelson, J. The Physics of Solar Cells (Properties of Semiconductor Materials). Imperial College Press 384 (Imperial College Press, 2001).
40. Shockley, W. & Queisser, H. J. Detailed Balance Limit of Efficiency of p-n Junction Solar Cells. J. Appl. Phys. **32,** 510 (1958).
41. Rau, U. & Schmidt, M. Electronic properties of ZnO/CdS/Cu(In,Ga)Se2 solar cells — aspects of heterojunction formation. Thin Solid Films **387,** (2001).
42. SCHMID, D., RUCKH, M. & SCHOCK, H. A comprehensive characterization of the interfaces in Mo/CIS/CdS/ZnO solar cell structures. Sol. Energy Mater. Sol. Cells **41–42,** (1996).
43. Neugebohrn, N., Hammer, M. S., Neerken, J., Parisi, J. & Riedel, I. Analysis of the back contact properties of Cu(In,Ga)Se2 solar cells employing the thermionic emission model. Thin Solid Films **582,** (2015).
44. Shockley, W. & Read, W. T. Statistics of the Recombinations of Holes and Electrons. Phys. Rev. **87,** (1952).
45. Hall, R. N. Electron-Hole Recombination in Germanium. Phys. Rev. **87,** (1952).
46. Braunger, D., Hariskos, D., Bilger, G., Rau, U. & Schock, H. . Influence of sodium on the growth of polycrystalline Cu(In,Ga)Se 2 thin films. Thin Solid Films **361–362,** (2000).
47. Gershon, T. et al. The Role of Sodium as a Surfactant and Suppressor of Non-Radiative Recombination at Internal Surfaces in Cu2ZnSnS4. Adv. Energy Mater. **5,** (2015).
48. Haight, R. et al. Band alignment at the Cu2ZnSn(SxSe1−x)4/CdS interface. Appl. Phys. Lett. **98,** (2011).
49. Terada, N. et al. Characterization of electronic structure of Cu 2 ZnSn(S x Se 1−x) 4 absorber layer and CdS/Cu 2 ZnSn(S x Se 1−x) 4 interfaces by in-situ photoemission and inverse photoemission spectroscopies. Thin Solid Films **582,** (2015).
50. Du, H. et al. Investigation of combinatorial coevaporated thin film Cu2ZnSnS4. I. Temperature effect, crystalline phases, morphology, and photoluminescence. J. Appl. Phys. **115,** (2014).
51. Scragg, J. J. S. et al. Cu-Zn disorder and band gap fluctuations in Cu2 ZnSn(S,Se)4 : Theoretical and experimental investigations: Cu-Zn disorder and band gap fluctuations in Cu2 ZnSn(S,Se)4. Phys. Status solidi **253,** (2016).
52. Scragg, J. J. et al. A detrimental reaction at the molybdenum back contact in Cu2ZnSn(S,Se)4 thin-film solar cells. J. Am. Chem. Soc. **134,** 19330–19333 (2012).
53. Chen, S., Walsh, A., Gong, X.-G. & Wei, S.-H. Classification of lattice defects in the kesterite Cu2ZnSnS4 and Cu2ZnSnSe4 earth-abundant solar cell absorbers. Adv. Mater. **25,** 1522–1539 (2013).
54. Shin, D., Saparov, B. & Mitzi, D. B. Defect Engineering in Multinary Earth-Abundant Chalcogenide Photovoltaic Materials. Adv. Energy Mater. **7,** (2017).
55. Guo, Q. et al. Fabrication of 7.2% Efficient CZTSSe Solar Cells Using CZTS Nanocrystals. J. Am. Chem. Soc. **132,** 17384–17386 (2010).
56. Ahmed, S. et al. A High Efficiency Electrodeposited Cu2ZnSnS4 Solar Cell. Adv. Energy Mater. **2,** 253–259 (2012).
57. Larramona, G. et al. Fine-Tuning the Sn Content in CZTSSe Thin Films to Achieve 10.8%

Solar Cell Efficiency from Spray-Deposited Water-Ethanol-Based Colloidal Inks. Adv. Energy Mater. **5,** 1501404 (2015).

58. Wang, W. et al. Device Characteristics of CZTSSe Thin-Film Solar Cells with 12.6% Efficiency. Adv. Energy Mater. **4,** 1301465 (2014).
59. Su, Z. et al. Fabrication of Cu2ZnSnS4 Solar Cells with 5.1% Efficiency via Thermal Decomposition and Reaction Using a Non-Toxic Sol–Gel Route. J. Mater. Chem. **2,** 500–509 (2014).
60. Uhl, A. R. et al. Non-Vacuum Deposition of Cu(In,Ga)Se2 Absorber Layers from Binder Free, Alcohol Solutions: Deposition of Cu(In,Ga)Se2 Absorber Layers. Prog. Photovoltaics: Res. Appl. **20,** 526–533 (2012).
61. Fu, J. et al. Tuning the Se Content in Cu2ZnSn(S, Se)4 Absorber to Achieve 9.7% Solar Cell Efficiency from a Thiol/Amine-Based Solution Process. ACS Appl. Energy Mater. **1,** 594–601 (2018).
62. Ki, W. & Hillhouse, H. W. Earth-Abundant Element Photovoltaics Directly from Soluble Precursors with High Yield Using a Non-Toxic Solvent. Adv. Energy Mater. **1,** 732–735 (2011).
63. Xin, H., Katahara, J. K., Braly, I. L. & Hillhouse, H. W. 8% Efficient Cu2ZnSn(S,Se)4 Solar Cells from Redox Equilibrated Simple Precursors in DMSO. Adv. Energy Mater. **4,** 1301823 (2014).
64. Xin, H. et al. Lithium-Doping Inverts the Nanoscale Electric Field at the Grain Boundaries in Cu2ZnSn(S,Se)4 and Increases Photovoltaic Efficiency. Phys. Chem. Chem. Phys. **17,** 23859–23866 (2015).
65. Uhl, A. R., Katahara, J. K. & Hillhouse, H. W. Molecular-Ink Route to 13.0% Efficient Low-Bandgap CuIn(S,Se)2 and 14.7% Efficient Cu(In,Ga)(S,Se)2 Solar Cells. Energy & Environ. Sci. **9,** 130–134 (2016).
66. Collord, A. D. & Hillhouse, H. W. Germanium Alloyed Kesterite Solar Cells with Low Voltage Deficits. Chem. Mater. **28,** 2067–2073 (2016).
67. Tiwari, D. et al. Single Molecular Precursor Solution for CuIn(S,Se) Thin Films Photovoltaic Cells: Structure and Device Characteristics. ACS Appl. Mater. & interfaces **9,** 2301–2308 (2017).
68. Guo, Q. et al. Development of CuInSe2 nanocrystal and nanoring inks for low-cost solar cells. Nano Lett. **8,** 2982–2987 (2008).
69. Hages, C. J., Koeper, M. J., Miskin, C. K., Brew, K. W. & Agrawal, R. Controlled Grain Growth for High Performance Nanoparticle-Based Kesterite Solar Cells. Chem. Mater. **28,** (2016).
70. Martin, T. R. et al. Nanoparticle Ligands and Pyrolized Graphitic Carbon in CZTSSe Photovoltaic Devices. Chem. Mater. **28,** (2016).
71. R. Uhl, A. et al. Solution-processed low-bandgap CuIn(S,Se)2 absorbers for high efficiency single junction and monolithic chalcopyrite-perovskite tandem solar cells. Submitted (2016). doi:10.1021/nl101284k
72. Collord, A. & Hillhouse, H. W. Screening of alkali elements in Cu2ZnSn(S,Se)4. in 2015 IEEE 42nd Photovoltaic Specialist Conference (PVSC) 1–4 (IEEE, 0). doi:10.1109/PVSC.2015.7356190

73. Haass, S. G. et al. Complex Interplay between Absorber Composition and Alkali Doping in High‐Efficiency Kesterite Solar Cells. Adv. Energy Mater. **8,** 1701760 (2018).
74. Haass, S. G. et al. 11.2% Efficient Solution Processed Kesterite Solar Cell with a Low Voltage Deficit. Adv. Energy Mater. **5,** (2015).
75. Werner, M. et al. Enhanced Carrier Collection from CdS Passivated Grains in Solution-Processed Cu2ZnSn(S,Se)4 Solar Cells. ACS Appl. Mater. & interfaces **7,** 12141–12146 (2015).
76. Sutter-Fella, C. M. et al. Sodium Assisted Sintering of Chalcogenides and Its Application to Solution Processed Cu2ZnSn(S,Se)4 Thin Film Solar Cells. Chem. Mater. **26,** (2014).
77. Werner, M., Sutter-Fella, C. ., Romanyuk, Y. . & Tiwari, A. . 8.3% efficient Cu2ZnSn(S,Se)4 solar cells processed from sodium-containing solution precursors in a closed reactor. Thin Solid Films **582,** (2015).
78. Schnabel, T., Abzieher, T., Friedlmeier, T. M. & Ahlswede, E. Solution-Based Preparation of Cu2ZnSn(S,Se)4 for Solar Cells—Comparison of SnSe2 and Elemental Se as Chalcogen Source. IEEE J. Photovoltaics **5,**
79. Neuwirth, M. et al. A multiple-selenization process for enhanced reproducibility of Cu2ZnSn(S,Se)4 solar cells. Appl. Phys. Lett. **109,** (2016).
80. Abzieher, T., Schnabel, T., Hetterich, M., Powalla, M. & Ahlswede, E. Source and effects of sodium in solution-processed kesterite solar cells: Source and effects of sodium in solution-processed kesterite solar cells. Phys. Status solidi **213,** (2016).
81. Xiao, Z.-Y. et al. Influencing Mechanism of the Selenization Temperature and Time on the Power Conversion Efficiency of Cu2ZnSn(S,Se)4-Based Solar Cells. ACS Appl. Mater. & interfaces **8,** 17334–17342 (2016).
82. Altamura, G., Wang, M. & Choy, K.-L. Improving efficiency of electrostatic spray-assisted vapor deposited Cu2ZnSn(S,Se)4 solar cells by modification of Mo/absorber interface. Thin Solid Films **597,** (2015).
83. Schnabel, T. & Ahlswede, E. On the interface between kesterite absorber and Mo back contact and its impact on solution-processed thin-film solar cells. Sol. Energy Mater. Sol. Cells **159,** (2017).
84. Madarász, J., Bombicz, P., Okuya, M. & Kaneko, S. Thermal Decomposition of Thiourea Complexes of Cu(I), Zn(II), and Sn(II) Chlorides as Precursors for the Spray Pyrolysis Deposition of Sulfide Thin Films. Solid State Ionics **141,** 439–446 (2001).
85. Scragg, J. J., Ericson, T., Kubart, T., Edoff, M. & Platzer-Bjorkman, C. Chemical Insights into the Instability of Cu2ZnSnS4 Films during Annealing. **23,** 4625–4633 (2011).
86. Fernandes, P. ., Salomé, P. M. . & da Cunha, A. . Study of polycrystalline Cu2ZnSnS4 films by Raman scattering. J. Alloy. Compd. **509,** (2011).
87. Fernandes, P. ., Salomé, P. M. . & da Cunha, A. . Growth and Raman scattering characterization of Cu2ZnSnS4 thin films. Thin Solid Films **517,** (2009).
88. Cheng, A.-J. et al. Imaging and phase identification of Cu2ZnSnS4 thin films using confocal Raman spectroscopy. J. Vac. Sci. & Technol. A: Vacuum, Surfaces, Films **29,** (2011).
89. Romero, M. J., Du, H., Teeter, G., Yan, Y. & Al-Jassim, M. M. Comparative study of the luminescence and intrinsic point defects in the kesterite Cu2ZnSnS4and chalcopyrite Cu(In,Ga)Se2thin films used in photovoltaic applications. Phys. Rev. B **84,** (2011).

90. Su, Z. et al. Cation Substitution of Solution-Processed Cu2ZnSnS4Thin Film Solar Cell with over 9% Efficiency. Adv. Energy Mater. **5,** (2015).
91. Zhang, L. H., Gong, H. & Wang, J. P. Thermal decomposition kinetics of amorphous carbon nitride and carbon films. J. Physics: Condens. Matter **14,** 1697 (1999).
92. Ferrari, A. C., Rodil, S. E. & Robertson, J. Interpretation of infrared and Raman spectra of amorphous carbon nitrides. Phys. Rev. B **67,** (2003).
93. Rodil, S. ., Muhl, S., Maca, S. & Ferrari, A. . Optical gap in carbon nitride films. Thin Solid Films **433,** (2003).
94. Han, H.-X. & Feldman, B. J. Structural and optical properties of amorphous carbon nitride. Solid State Commun. **65,** (1988).
95. Wang, S., Gao, Q. & Wang, J. Thermodynamic analysis of decomposition of thiourea and thiourea oxides. J. Phys. Chem. B **109,** 17281–17289 (2005).
96. Ang, T. P. & Chan, Y. M. Comparison of the melon nanocomposites in structural properties and photocatalytic activities. J. Phys. Chem. C **115,** 15965–15972 (2009).
97. Giovannozzi, A. M. et al. Rapid and sensitive detection of melamine in milk with gold nanoparticles by Surface Enhanced Raman Scattering. Food Chem. **159,** 250–256 (2014).
98. McMillan, P. F. et al. Graphitic carbon nitride C6N9H3·HCl: Characterisation by UV and near-IR FT Raman spectroscopy. J. Solid State Chem. **182,** (2009).
99. Colombara, D. et al. Deliberate and Accidental Gas-Phase Alkali Doping of Chalcogenide Semiconductors: Cu(In,Ga)Se. Sci. reports **7,** 43266 (2017).
100. Wu, S.-H. et al. High-efficiency Cu2ZnSn(S,Se)4solar cells fabricated through a low-cost solution process and a two-step heat treatment: High-efficiency Cu2ZnSn(S,Se)4solar cells. Prog. Photovoltaics: Res. Appl. **25,** (2017).
101. Wu, S.-H., Huang, K.-T., Chen, H.-J. & Shih, C.-F. Cu 2 ZnSn(S x Se 1 −x) 4 thin film solar cell with high sulfur content (x approximately 0.4) and low V oc deficit prepared using a postsulfurization process. Sol. Energy Mater. Sol. Cells **175,** (2018).
102. Kim, S., Kim, K. M., Tampo, H., Shibata, H. & Niki, S. Improvement of voltage deficit of Ge-incorporated kesterite solar cell with 12.3% conversion efficiency. Appl. Phys. Express **9,** (2016).
103. Giraldo, S. et al. Solar Cells: Large Efficiency Improvement in Cu2ZnSnSe4 Solar Cells by Introducing a Superficial Ge Nanolayer (Adv. Energy Mater. 21/2015). Adv. Energy Mater. **5,** (2015).
104. Ford, G. M., Guo, Q., Agrawal, R. & Hillhouse, H. W. Earth Abundant Element Cu2Zn(Sn1−xGex)S4 Nanocrystals for Tunable Band Gap Solar Cells: 6.8% Efficient Device Fabrication. Chem. Mater. **23,** (2011).
105. Qi, Y. et al. Elemental Precursor Solution Processed (CuAg)ZnSn(S,Se) Photovoltaic Devices with over 10% Efficiency. ACS Appl. Mater. & interfaces **9,** 21243–21250 (2017).
106. Gershon, T. et al. Photovoltaic Materials and Devices Based on the Alloyed Kesterite Absorber (AgxCu1-x)2ZnSnSe4. Adv. Energy Mater. **6,** (2016).
107. Qi, Y.-F. et al. Engineering of interface band bending and defects elimination via a Ag-graded active layer for efficient (Cu,Ag)2ZnSn(S,Se)4 solar cells. Energy & Environ. Sci. **10,** (2014).
108. Scrosati, B. & Vincent, C. A. Solubility Data Series: Alkali Metal, Alkaline-Earth Metal and Ammonium Halides. Amide Solvents. J. Electroanal. Chem. **11,** 100 (1980).

109. Rosen, B. M. et al. The Disproportionation of Cu(I)X Mediated by Ligand and Solvent into Cu(0) and Cu(II)X2 and its Implications for SET-LRP. J. Polym. Sci. Part A: Polym. Chem. **47,** 5606–5628 (2009).
110. Ahrland, S., Nilsson, K. & . Tagesson, B. Thermodynamics of the Copper (I) Halide and Thiocyanate Complex Formation in Acetonitrile. Acta Chemica Scandinavica **A,** 193–201 (1983).
111. Zhao, H., Chang, J., Boika, A. & Bard, A. J. Electrochemistry of High Concentration Copper Chloride Complexes. Anal. Chem. **85,** 7696–7703 (2013).
112. Lamoureux, M. & Milne, J. Selenium Chloride and Bromide Equilibria in Aprotic Solvents; a 77Se NMR Study. Polyhedron **9,** 589–595 (1990).
113. Baumann, M. E., Capraro, H.-G., Hilfinker, R. & Ochsner, M. Synthesis of Axially Disubstituted Octakis-Alkoxy-Germanium(IV) Phthalocyanines. in Photodynamic Therapy of Cancer (eds. Jori, G., Moan, J. & Star, W. M.) **2078,** 460–467 (1994).
114. Egorov, M. . et al. Electrochemistry of Complexes of Dichlorogermylene and Dihalostannylenes with Chromium, Molybdenum, and Tungsten Pentacarbonyls. J. Organomet. Chem. **574,** 279–285 (1999).
115. Bowmaker, G. A. et al. Crystal Structures and Vibrational Spectroscopy of Copper(I) Thiourea Complexes. Inorg. Chem. **48,** 350–368 (2008).
116. Spofford, W. A. & Amma, E. L. The Crystal Structure of Bis (Thiourea) Copper(I) Chloride. Acta Crystallogr. Sect. B: Struct. Crystallogr. Cryst. Chem. **26,** 1474–1483 (1970).
117. Vizzini, E. A., Taylor, I. F. & Amma, E. L. Electron-Deficient Bonding with Sulfur Atoms. III. Crystal and Molecular Structure of Bis (Thiourea) Silver(I) Chloride. Inorg. Chem. **7,** 1351–1357 (1968).
118. Otto, K. et al. Structure and Evolved Gas Analyses (TG/DTA-MS and TG-FTIR) of Mer-Trichlorotris (Thiourea)-Indium(III), a Precursor for Indium Sulfide Thin Films. J. Therm. Anal. Calorim. **105,** 83–91 (2011).
119. Ryabchikov, D. I. & Nazarenko, I. I. New Aspects of the Chemistry of Complexes of Selenium and Tellurium. Russ. Chem. Rev. **33,** 55–64 (1964).
120. Durgaprasad, G., Sathyanarayana, D. N. & Patel, C. C. Infrared Spectra and Normal Vibrations ofN,N-Dimethylformamide andN,N-Dimethylthioformamide. Bull. Chem. Soc. Jpn. **44,** (1971).
121. Kumari, R. G. et al. Raman spectral investigation of thiourea complexes. Spectrochim. acta. Part Mol. Biomol. Spectrosc. **73,** 263–267 (2009).
122. Mathur, M. S., Ho, J. H. K. & Tabisz, G. C. Raman Study of InCl3. Spectrosc. Lett. **14,** 395–404 (1981).
123. Frost, R. L. Raman spectroscopy of selected copper minerals of significance in corrosion. Spectrochim. acta. Part Mol. Biomol. Spectrosc. **59,** 1195–1204 (2003).
124. DODSON, R. M. & KING, L. C. The reaction of ketones with halogens and thiourea. J. Am. Chem. Soc. **67,** 2242 (1945).
125. Spinner, E. The vibration spectra and structures of the hydrochlorides of urea, thiourea and acetamide. The basic properties of amides and thioamides. Spectrochim. Acta **15,** (1959).
126. Takahashi, R., Suzuki, H. & Ishiguro, S. Solution Equilibria of Gallium(III) and Indium(III) Complexes with Halide and Thiocyanate Ions in N,N-Dimethylformamide. J. Chem. Soc. Faraday Trans. **92,** 2715–2724 (1996).

127. Brebrick, R. F. Vapor Pressure of Indium Chloride and Some Implications for the In-Se System. J. Phase Equilibria Diffus. **26,** 20–22 (2005).
128. Keneshea, F. . & Cubicciotti, D. Vapor Pressures of Zinc Chloride and Zinc Bromide and Their Gaseous Dimerization. J. Chem. Phys. **40,** 191–199 (1964).
129. Freiser, H. Gas-Liquid Partition Chromatography for Metals Separations. Anal. Chem. **31,** 1440–1440 (1959).
130. Katahara, J. K. & Hillhouse, H. W. Quasi-Fermi level splitting and sub-bandgap absorptivity from semiconductor photoluminescence. J. Appl. Phys. **116,** (2014).
131. Dorfs, D. et al. Reversible Tunability of the Near-Infrared Valence Band Plasmon Resonance in Cu2-x Se Nanocrystals. J. Am. Chem. Soc. **133,** 11175–11180 (2011).
132. Arnou, P. et al. Solution processing of CuIn(S,Se) 2 and Cu(In,Ga)(S,Se) 2 thin film solar cells using metal chalcogenide precursors. Thin Solid Films **633,** (2017).
133. Mendis, B. G. et al. Direct observation of Cu, Zn cation disorder in Cu2ZnSnS4solar cell absorber material using aberration corrected scanning transmission electron microscopy: Aberration corrected STEM in Cu, Zn cation disorder in CZTS. Prog. Photovoltaics: Res. Appl. **22,** (2014).
134. Bourdais, S. et al. Is the Cu/Zn Disorder the Main Culprit for the Voltage Deficit in Kesterite Solar Cells? Adv. Energy Mater. **6,** (2016).
135. Katahara, J. K. & Hillhouse, H. W. V overestimation from photoluminescence quantum yield in disordered absorber layers. in 2016 IEEE 43rd Photovoltaic Specialists Conference (PVSC) 3563–3566 (IEEE). doi:10.1109/PVSC.2016.7750335
136. Collord, A. D., Xin, H. & Hillhouse, H. W. Combinatorial Exploration of the Effects of Intrinsic and Extrinsic Defects in Cu2ZnSn(S,Se)4. IEEE J. Photovoltaics **5,**
137. Lafond, A. et al. Substitution of Li for Cu in CuZnSnS: Toward Wide Band Gap Absorbers with Low Cation Disorder for Thin Film Solar Cells. Inorg. Chem. **56,** 2712–2721 (2017).
138. Yuan, Z.-K. et al. Engineering Solar Cell Absorbers by Exploring the Band Alignment and Defect Disparity: The Case of Cu- and Ag-Based Kesterite Compounds. Adv. Funct. Mater. **25,** (2015).
139. Valakh, M. Y. et al. Optical properties of quaternary kesterite-type Cu2Zn(Sn1−xGex)S4 crystalline alloys: Raman scattering, photoluminescence and first-principle calculations. RSC Adv. **6,** (2014).
140. Maeda, T., Nakamura, S. & Wada, T. First-principles calculations of vacancy formation in In-free photovoltaic semiconductor Cu2ZnSnSe4. Thin Solid Films **519,** (2011).
141. Nakamura, S., Maeda, T. & Wada, T. Phase Stability and Electronic Structure of In-Free Photovoltaic Materials: Cu2ZnSiSe4, Cu2ZnGeSe4, and Cu2ZnSnSe4. Jpn. J. Appl. Phys. **49,** (2010).
142. Gong, W. et al. Crystallographic and optical properties of (Cu, Ag)2ZnSnS4and (Cu, Ag)2ZnSnSe4solid solutions: Crystallographic and optical properties of (Cu, Ag)2ZnSnS4and (Cu, Ag)2ZnSnSe4solid solutions. Phys. Status solidi **12,** (2015).
143. Luo, Y. et al. A review on the occurrence of micropollutants in the aquatic environment and their fate and removal during wastewater treatment. Sci. Total. Environ. **473–474,** 619–641 (2014).
144. Calero-Cáceres, W. et al. Sludge as a potential important source of antibiotic resistance genes in

both the bacterial and bacteriophage fractions. Environ. Sci. & Technol. **48,** 7602–7611 (2014).
145. Gerrity, D. W., Benotti, M. J., Reckhow, D. A. & Snyder, S. A. Pharmaceuticals and Endocrine-Disrupting Compounds in Drinking Water. in Biophysico-Chemical Processes of Anthropogenic Organic Compounds in Environmental Systems: Xing/Anthropogenic Organic Compounds 233–249 (John Wiley & Sons, Inc., 2011). doi:10.1002/9780470944479.ch9
146. Lienert, J., Bürki, T. & Escher, B. I. Reducing micropollutants with source control: substance flow analysis of 212 pharmaceuticals in faeces and urine. Water Sci. Technol. J. Int. Assoc. Water Pollut. Res. **56,** 87–96 (2005).
147. Lienert, J., Güdel, K. & Escher, B. I. Screening method for ecotoxicological hazard assessment of 42 pharmaceuticals considering human metabolism and excretory routes. Environ. Sci. & Technol. **41,** 4471–4478 (2007).
148. Jasper, J. T., Yang, Y. & Hoffmann, M. R. Toxic Byproduct Formation during Electrochemical Treatment of Latrine Wastewater. Environ. Sci. & Technol. **51,** 7111–7119 (2017).
149. Jojoa-Sierra, S. D., Silva-Agredo, J., Herrera-Calderon, E. & Torres-Palma, R. A. Elimination of the antibiotic norfloxacin in municipal wastewater, urine and seawater by electrochemical oxidation on IrO anodes. Sci. Total. Environ. **575,** 1228–1238 (2017).
150. Cotillas, S., Lacasa, E., Sáez, C., Cañizares, P. & Rodrigo, M. A. Electrolytic and electro-irradiated technologies for the removal of chloramphenicol in synthetic urine with diamond anodes. Water Res. **128,** 383–392 (2018).
151. Zöllig, H., Remmele, A., Morgenroth, E. & Udert, K. M. Removal rates and energy demand of the electrochemical oxidation of ammonia and organic substances in real stored urine. Environ. Sci. Water Res. & Technol. **3,** (2015).
152. Zöllig, H., Remmele, A., Fritzsche, C., Morgenroth, E. & Udert, K. M. Formation of Chlorination Byproducts and Their Emission Pathways in Chlorine Mediated Electro-Oxidation of Urine on Active and Nonactive Type Anodes. Environ. Sci. & Technol. **49,** 11062–11069 (2015).
153. Yang, Y., Shin, J., Jasper, J. T. & Hoffmann, M. R. Multilayer Heterojunction Anodes for Saline Wastewater Treatment: Design Strategies and Reactive Species Generation Mechanisms. Environ. Sci. & Technol. **50,** 8780–8787 (2016).
154. Cho, K. & Hoffmann, M. R. Urea degradation by electrochemically generated reactive chlorine species: products and reaction pathways. Environ. Sci. & Technol. **48,** 11504–11511 (2014).
155. Li, H., Yu, Q., Yang, B., Li, Z. & Lei, L. Electro-catalytic oxidation of artificial human urine by using BDD and IrO2 electrodes. J. Electroanal. Chem. **738,** (2015).
156. Rose, C., Parker, A., Jefferson, B. & Cartmell, E. The Characterization of Feces and Urine: A Review of the Literature to Inform Advanced Treatment Technology. Crit. Rev. Environ. Sci. Technol. **45,** 1827–1879 (2015).
157. Udert, K. M., Larsen, T. A., Biebow, M. & Gujer, W. Urea hydrolysis and precipitation dynamics in a urine-collecting system. Water Res. **37,** 2571–2582 (2003).
158. Larsen, T. A. Source Separation and Decentralization for Wastewater Management. Water Intell. Online **12,** (2013).
159. United States Environmental Protection Agency Proposed Rule for perchlorate. *https://www.epa.gov/dwstandardsregulations/perchlorate-drinking-water. (accessed 2019-5-30)*

160. California Office of Environmental Health Hazard Assessment Proposed Action Level for Chlorate. https://oehha.ca.gov/water/notification-level/proposed-action-level-chlorate.(accessed 2019-5-30)
161. Murata, M. et al. Electrochemical detection of free chlorine at highly boron-doped diamond electrodes. J. Electroanal. Chem. **612,** (2008).
162. Patil, P. ., Kawar, R. . & Sadale, S. . Electrochromism in spray deposited iridium oxide thin films. Electrochimica Acta **50,** (2005).
163. Dodd, M. C. & Huang, C.-H. Transformation of the antibacterial agent sulfamethoxazole in reactions with chlorine: kinetics, mechanisms, and pathways. Environ. Sci. & Technol. **38,** 5607–5615 (2004).
164. Hellström, D., Johansson, E. & Grennberg, K. Storage of human urine: acidification as a method to inhibit decomposition of urea. Ecol. Eng. **12,** (1999).
165. Hora, P. I., Novak, P. J. & Arnold, W. A. Photodegradation of pharmaceutical compounds in partially nitritated wastewater during UV irradiation. Environ. Sci. Water Res. & Technol. **5,** (2019).
166. Rodriguez, J. M. D., Melian, J. A. H. & Pena, J. P. Determination of the Real Surface Area of Pt Electrodes by Hydrogen Adsorption Using Cyclic Voltammetry. J. Chem. Educ. (1998). doi:10.1021/ED077P1195
167. Yang, Q. et al. Catalytic and electrocatalytic reduction of perchlorate in water – A review. Chem. Eng. J. **306,** (2016).